Defining the osteoclast response to *Staphylococcus aureus* osteomyelitis

By

Jenna R. Petronglo

Dissertation

Submitted to the Faculty of the

Graduate School of Vanderbilt University

in partial fulfillment of the requirements

for the degree of

DOCTOR OF PHILOSOPHY

In

Molecular Pathology and Immunology

May 12, 2023

Nashville, Tennessee

Approved:

James E. Cassat, M.D., Ph.D
Ken S. Lau, Ph.D.
Jeffrey C. Rathmell, Ph.D.
Julie A. Rhoades, Ph.D.
Edward R. Sherwood, M.D., Ph.D.

DEDICATION

I dedicate this work to my mom,
who believed in me so much,
I began to believe in myself.

ACKNOWLEDGEMENTS

I would like to thank all the teachers and mentors (scientific and otherwise) who helped me and encouraged me through my many stages of education. I would like to thank those who invested time and energy in teaching me laboratory and research skills when I was an inexperienced, and largely clueless, undergraduate. These early opportunities and experiences were fundamental to my decision to become a scientist.

I thank my committee members Dr. Jeff Rathmell, Dr. Ken Lau, Dr. Julie Rhoades, and Dr. Ed Sherwood. I am grateful for all your advice and constructive critiques. Thank you for taking time out of your busy schedules to help me. I am thankful to all the core resources I utilized for my projects. I thank Margaret Allaman for helping me run my Luminex experiments. I thank Dr. Sasi Uppuganti for always being so helpful whenever I had questions about micro-CT. I thank Josh Johnson for sectioning femurs—this was essential for the data I needed for my first author paper. I am also grateful to the Wilson lab for allowing me to use the Odyssey imager to take pictures of my immunoblots. I would also like to acknowledge our collaborators at Wash U, Dr. Gabriel Mbalaviele and Dr. Deb Veis. It has been great to work together studying the role of the inflammasome in osteomyelitis.

I must whole-heartedly thank all the Cassat lab members I have had the good fortune to work with. You all have taught me so much, and I am proud to count you as both colleagues and friends. To season 1 grad students Niki Putman, Aimee Potter, Caleb Ford, Tom Spoonmore, and Chris Peek—your intimidating intelligence motivated me to do my best and your support and encouragement meant so much than you can ever know. I must also thank Casey Butrico, who is a friend as true as they come, as well as a disciplined and excellent scientist who has lent me a helping hand too many times to count. I am grateful to current and former Research Assistants Laura Fulbright, Jacob Curry, and Virginia Cruz-Victorio--you all were always ready to help without complaint and kept the lab running seamlessly. A huge thanks to the postdocs: Kara who lifts everyone up with her positive spirit, Brittney who is refreshingly willing to tell it like it is, and Juan who is full of big ideas. I thank newer lab members including Clara Si, for her enthusiasm for the inflammasome, and Sana Fatah, for working with me on project that ended up being full of technical challenges and for being a great mentee. I am grateful to my dissertation mentor, Dr. Jim Cassat, who reminds me that imagination, curiosity, and humility and are all essential qualities of a great scientist. Jim finds a way to see the best in every student, and I am grateful for his advice, encouragement, and trust, which saw me through some very difficult times.

Finally, I must thank my friends and family. I thank: my mommom, Tulia, whose many sacrifices gave her family opportunity and security; my father, whose dogged commitment to his farm and crops perhaps rubbed off on me (except I harvest data instead of eggplants); and my Aunt Mary who has been endlessly encouraging. I thank my twin sister Kaitlyn, a fiercely hilarious person who keeps me laughing and who held me accountable to my longstanding goal of pursuing a PhD. I thank my older sister Aimee, who uses her big heart and extreme strength to hold our family together. I could not have succeeded without my mom, who invested so much of herself in raising me and who dreamed for me a life where I could fully pursue my goals and aspirations. I thank my partner, Keifer, who generously supports me through times of stress and who makes the best coffee. Thank you to my grad school friends Casey and Andrea, who made this experience so much more fun. Thank you to my lifelong friend Kyle, whose sharp wit always makes me laugh—I will never forget you did better than me in AP Biology. I also thank my friend Casey Howe whose support guided me through so many tough times.

To pursue scientific questions of one's own choosing, with the answer promising nothing more than the potential to someday, possibly, fit into the greater puzzle of life, is an immense privilege. My time in graduate school has been fun, darkly comical, very challenging, and sometimes amazing. My education in science and research has been the greatest privilege. I am grateful to all those who invested in my training and helped me learn how to be a scientist.

TABLE OF CONTENTS

LIST OF TABLES

LIST OF FIGURES

LIST OF ABBREVIATIONS

Name	Abbreviation
Accessory gene regulator	Agr
Absent in melanoma 2	AIM2
Component of activator protein-1	AP-1
Apoptosis-associated speck-like protein containing CARD	ASC
Bone marrow-derived monocytes	BMDM
BRCA2 containing complex subunit 3	BRCC3
bone volume / total volume	BV/TV
Cryopyrin-associated autoinflammatory syndromes	CAPS
Caspase activation and recruitment domain	CARD
Colony forming units	CFU
Chronic recurrent multifocal osteomyelitis	CRMO
Colony-stimulating factor 1 receptor	CSF-1R
Damage-associated molecular pattern	DAMP
DNAX-activating protein of 12 kDa	DAP12
4′,6-diamidino-2-phenylindole	DAPI
Dimethyl sulfoxide	DMSO
De-ubiquitinating enzyme	DUB
Enzyme-linked Immunoassay	ELISA
Endoplasmic reticulum	ER
Extracellular signal-regulated kinase	ERK
Fc receptor common γ	FcRγ
Insulin-like growth factor-1	IGF-1
Interleukin-10	IL-10
Interleukin-1 receptor type 1	IL-1R1
Interleukin-1 alpha	IL-1α
Interleukin-1 beta	IL-1β
Interleukin-4	IL-4
Interleukin-6	IL-6
Inositol 1, 4, 5-triphosphate	IP3
Interleukin-1 receptor-associated kinase 1	IRAK1
Transmembrane immunoreceptor tyrosine-based activation motif	ITAM
Jumonji domain-containing 3	JMJD3
c-Jun N-terminal kinase	JNK
lactate dehydrogenase	LDH
Lipopolysaccharide	LPS
Leucine-rich repeat	LRR
Mitogen-activated protein kinases	MAPK
Macrophage colony-stimulating factor	M-CSF
Myeloid DAP12 associated lectin or CLEC5A (MDL-1)	MDL-1
Mixed lineage kinase domain-like (MLKL)	MLKL
Multiplicity of infection	MOI

Microbial surface components recognizing adhesive matrix molecules	MSCRAMMs
Myeloid differentiation marker 88	Myd88
NAIP, CIITA, HET-E, and TP1	NACHT
NIMA-related kinase 7	NEK7
Nuclear factor of activated T cells c1	NFATc1
Nuclear factor-kappa B	NFκB
Nucleotide binding and oligomerization, leucine-rich repeat, pyrin domain-containing 3	NLRP3
Osteocyte lacuno-canalicular network	OCLN
Osteoprotegerin	OPG
Osteoclast-associated receptor	OSCAR
Pathogen-associated molecular pattern	PAMP
Phosphate-buffered saline	PBS
Phosphatidylinositol 3-kinase	PI3K
Paired immunoglobulin-like receptor A	PIR-A
Phospholipase C γ	PLCγ
Pattern recognition receptor	PRR
Alpha-type phenol-soluble modulins	PSMα
N-terminal pyrin domain	PYD
Quantitative real time- polymerase chain reaction	qRT-PCR
Receptor activator of nuclear factor (NF)-κB	RANK
Receptor activator of nuclear factor (NF)-κB ligand	RANKL
receptor interacting serine/threonine kinase 1	RIPK1
Receptor interacting serine/threonine kinase 1	RIPK1
Receptor interacting serine/threonine kinase 3	RIPK3
relative luminescence	RLU
RUNX family transcription factor 2	Runx2
Sialic acid-binding immunoglobulin-like lectin 15 (Siglec-15)	Siglec-15
Trichloroacetic acid	TCA
Transforming growth factor beta	TGF-β
Toll/interleukin-1 receptor/resistance	TIR
Toll-interleukin-1 receptor (TIR) domain-containing adaptor protein	TIRAP
Toll-like receptor	TLR
Tumor necrosis factor	TNF
Tumor necrosis factor receptor	TNFR
TNF receptor-activating factor	TRAF
Tartrate-resistant acid phosphatase	TRAP
Triggering receptor expressed on myeloid cells-2	TREM-2
Whole bone marrow	WBM
Micro-computed tomography	μCT
Staphylococcal abscess communities	SACs
Autoinducing peptide	AIP
Tryptic soy broth	TSB
Fetal bovine serum	FBS
Whole bone marrow	WBM
Dithiothreitol	DTT

Room temperature	RT
Standard deviation	SD
Microphthalmia-associated transcription factor	MITF
Micro-computed tomography	µCT
Nucleotide-binding oligomerization domain containing protein 2	NOD2
Revolutions per minute	rpm
Minute	min
Hour	h

INTRODUCTION

Inflammation of bone, known as osteomyelitis, is most commonly caused by infection with the Gram-positive bacterium *Staphylococcus aureus*. During osteomyelitis, the homeostasis-maintaining activities of bone-building osteoblasts and bone-resorbing osteoclasts are altered, resulting in aberrant bone formation and net bone loss. This perturbation of bone homeostasis manifests as bone damage. Successful treatment of osteomyelitis requires antibiotics and, in many cases, surgical debridement to remove necrotic and infected bone. Even with these measures, *S. aureus* osteomyelitis can progress to a chronic infection. Innate immune responses to *S. aureus* are facilitated by immune cell detection of pathogens through pattern-recognition receptor (PRRs) and subsequent elaboration of cytokines to recruit phagocytic cells like macrophages and neutrophils. While these responses are essential to host survival and bacterial containment, the inflammation generated by these responses also promotes dysregulation of bone homeostasis to induce bone damage. This dissertation will focus on mechanisms by which immune responses to *S. aureus* in infected bone drive dysregulation of bone homeostasis by influencing bone-resorbing osteoclasts.

Osteoclasts are large, multinucleated, bone-resorbing cells. These cells differentiate from the myeloid lineage in response to the canonical differentiation factor receptor activator of nuclear factor (NF)-κB ligand (RANKL). While molecular reprogramming during differentiation effectively turns the immune progenitor into a specialized bone cell, osteoclasts remain interconnected with the immune system. Cytokine responses occurring both systemically and within bone influence the differentiation and resorption of osteoclasts in both physiologic and disease states. The full extent to which osteoclasts themselves engage in immune processes, like cytokine production and Toll-like receptor (TLR) signaling, has been the subject of much inquiry. It is appreciated that TLR signaling in osteoclast precursors significantly influences whether the precursor commits to an osteoclast or macrophage cell fate. Whether sensing of *S. aureus* through TLRs has tangible effects on dysregulation of bone homeostasis during osteomyelitis is not clear. In Chapter II, I evaluate the role of *S. aureus* sensing TLRs 2 and 9 on host bacterial containment and on dysregulation of bone homeostasis during osteomyelitis, with a specific interest in how TLR signaling affects osteoclast differentiation. Chapter II will address the following Aim:

Aim 1: *Elucidate the role of Toll-like receptors (TLRs) 2 and 9 in the pathogenesis of dysregulation of bone homeostasis during* Staphylococcus aureus *osteomyelitis.*

Chapter III focuses on another facet of innate immunity, the interleukin-1 type 1 receptor (IL-1R1) signaling pathway, which is a major driver of the immune response to *S. aureus*. IL-1R1 cytokines promote osteoclast differentiation and resorption and contribute to osteoclast-mediated bone loss during osteomyelitis. The IL-1R1 cytokine IL-1β requires proteolytic processing to gain biologic activity. How IL-1β is produced and activated during *S. aureus* osteomyelitis is not known, although published findings show *S. aureus*-infected macrophages can activate IL-1β through the nucleotide binding and oligomerization, leucine-rich repeat, pyrin domain-containing 3 (NLRP3) inflammasome. The extent to which osteoclasts, which share a progenitor lineage with macrophages, engage in inflammasome activation to promote the dysregulation of bone homeostasis is not well understood. These outstanding questions will be addressed in Chapter III through the following Aim:

> ***Aim 2:*** *Determine how bacterial-induced inflammasome activation in osteoclasts and progenitors contributes to dysregulated bone homeostasis.*

In summary, this dissertation will interrogate how the *S. aureus*-sensing innate immune pathways, TLR signaling and the inflammasome, act through osteoclasts to alter bone homeostasis during osteomyelitis. Chapter I will present background information to support the scientific questions addressed in Chapters II and III. Chapter IV will deliver a summary of the findings from Chapters II and III and will offer plans for future experiments to expand upon these results.

CHAPTER I: BACKGROUND

Overview of *Staphylococcus aureus* osteomyelitis

S. aureus osteomyelitis etiology, treatment, and complications

Osteomyelitis is defined as inflammation of the bone. Although osteomyelitis can be incited by sterile inflammatory processes, bacterial infection most frequently acts as the triggering agent (1,2). The Gram-positive bacterium *Staphylococcus aureus* is the most common bacterial pathogen isolated from the infected bone (2,3). Osteomyelitis caused by *S. aureus* is a significant health condition that affects a broad patient population (4). Infection may be of hematogenous or contiguous origin (1,2,5). Hematogenous osteomyelitis strikes healthy children without known risk factors for infection (6). In adults, osteomyelitis can arise from hematogenous spread, but more commonly occurs following accidental inoculation during surgery or from trauma where the bone is directly exposed to bacteria (1,2,7). People with diabetes are at a high risk for developing osteomyelitis following skin infection, which can spread to the bone (4,8). These cases are often polymicrobial (4). This dissertation will focus on post-traumatic osteomyelitis caused by *S. aureus* with a particular interest in how the bone microenvironment is perturbed by the inflammatory response to infection.

S. aureus osteomyelitis can be difficult to diagnose due to variations in disease presentation (9). Clinical presentations of post-traumatic bone infection include poorly healing skin wounds and fracture nonunion. Diagnosis involves bloodwork, MRI imaging, and positive culture from a potentially infected bone sample (1,2,5). In the case of trauma, debridement surgery to remove necrotic bone and the infectious focus is used to facilitate antibacterial treatment (2,10). The efficacy of antibiotic treatment is hindered by bone necrosis and devascularization. Sequestrum, pieces of de-vascularized necrotic bone, can form as part of the disease process. Additionally, involucrum, a type of reactive bone formation initiated by periosteal cells, can develop to encase the sequestrum (11). These bone lesions can act as a nidus for infection (11,12). Because osteomyelitis develops and presents in many different ways, clinical scoring procedures including the Lew-Waldvogel and Cierny-Mader systems have been developed to help evaluate disease and standardize treatments (11,13). Even still, developing a universal, standard paradigm for treatment remains difficult due to the heterogeneity of the disease (9). Treating osteomyelitis is mired by complications that make infection resolution difficult to accomplish. *S. aureus* has a growing profile of resistance to many antibiotics (14). In addition to resistance, bacteria

can achieve tolerance to antibiotics through biofilm formation and other incompletely defined mechanisms (15). Finally, bacterial osteomyelitis results in severe bone damage. Infection perturbs the normal homeostasis-maintaining activities of bone cells. Pathologic bone loss and aberrant bone formation are hallmarks of disease (11,16). The pathologic changes to bone brought on by infection contribute to antibiotic recalcitrance and increase risk of complications such as pathologic fracture and altered mobility (5,11,17). Thus, better approaches to treat *S. aureus* osteomyelitis are needed. This dissertation focuses on identifying mechanisms by which *S. aureus* infection promotes dysregulation of bone homeostasis to drive bone damage during osteomyelitis. The experiments presented in Chapters II and III test how the immune response to *S. aureus* contributes to bone damage. *S. aureus* can also induce bone damage directly, and this will be discussed in the next section.

Overview of *S. aureus* pathogenicity and virulence

S. aureus can cause severe, invasive infection in many different tissue sites such as the skin, heart, lung, eye, and bone, as well systemically in the bloodstream (18). *S. aureus* was responsible for 119,427 bloodstream infections in the United States in 2017 alone, and 19,842 of those were fatal (19). Its versatility as a pathogen arises from its adaptive metabolism, manipulation and evasion of immune responses, and induction of toxin-mediated host cytotoxicity (20,21). The ability of *S. aureus* to persist in the host, induce tissue damage, and, in some cases, cause death, is best understood by examining specific ways *S. aureus* interacts with its host. For instance, while many bacterial organisms produce toxins that damage host tissues for bacterial gain, the *S. aureus* arsenal of specialized secreted virulence factors and toxins is distinctive due to its diversity and specialization. This section will focus on toxins and virulence factors that have significance to the pathogenesis of *S. aureus* osteomyelitis.

Exoproteins in the staphylococcal repertoire contribute to the development of bone damage during osteomyelitis (22). Some *S. aureus* toxins kill host cells by targeting specific cell surface receptors (20). This targeting mechanism is important to understanding how *S. aureus* causes deadly infection in humans. For example, the pore-forming toxin hemolysin-α (Hla) targets the cell surface receptors a disintegrin and metalloprotease 10 (ADAM10) and plekstrin-homology domain-containing protein A7 (PLEKA7) to lyse erythrocytes, endothelial cells, macrophages, T-cells, and B-cells (23–26). Hla has affinity for both mouse and human ADAM10 (20). It is also an activator of the inflammasome (27,28). It has also been shown to promote joint damage in a model of *S. aureus* septic arthritis and tissue damage in a model of *S. aureus* lung infection (29–31). Other toxins like leukocidin AB (LukAB) target cell surface receptors but have a high affinity for human, but not mouse, receptor isoforms (32,33). Toxins like LukAB that preferentially kill human immune cells are referred to as leukocidins.

These toxins may help *S. aureus* overcome the human host's attempt to generate neutralizing antibody responses to clear infection (33).

In addition to Hla and LukAB, which induce targeted cytotoxicity, *S. aureus* also utilizes toxins that lyse cells indiscriminately through membrane disruption. The small, amphipathic peptides of the phenol-soluble modulin (PSM) family kill in this manner (34). The alpha-type PSM (PSMα) toxins 1-4, four separate toxins encoded in the same operon, have been shown to induce bone damage during osteomyelitis (22,34). Transcription of the PSMα toxins is controlled by a two-component system called accessory gene regulator (Agr) (35). Agr is activated by environmental cues, including the buildup of autoinducing peptide (AIP), which signals that *S. aureus* population growth has reached a high threshold (36). The Agr system turns on a program of genes encoding toxins and virulence factors including the PSMα toxins (34). In part, PSMα toxins induce bone destruction by directly killing bone cells (22,37). In osteomyelitis, the *S. aureus* protease aureolysin controls toxicity of the PSMα toxins through proteasomal degradation. *S. aureus* mutant strains that do not express PSMα or have over-active aureolysin induce significantly less bone destruction in a mouse model of post-traumatic osteomyelitis (22). Thus, PSMα toxin-mediated bone damage represents one mechanism by which *S. aureus* directly causes bone damage. Bone damage still occurs in osteomyelitis induced by toxin-deficient strains and when Agr is inhibited, thus supporting the hypothesis that inflammation from the host response to *S. aureus* also drives bone damage (22,38). In this dissertation, I test how specific innate immune pathways influence bone damage during osteomyelitis. Experiments in Chapters II and III also test how osteoclasts respond to supernatant prepared from *S. aureus* growth cultures. I mainly employ supernatants from a PSMα-deficient (Δ*psmα1-4*) strain because the PSMα toxins are so lytic to bone cells, it is difficult to study the effects of other components when they are present (22,37).

In addition to inducing bone damage, *S. aureus* can persist in the bone, making it difficult to successfully eradicate using antibiotics. *S. aureus* makes adhesion molecules called microbial surface components recognizing adhesive matrix molecules (MSCRAMMs), which help it seed onto the bone (39,40). Once attached to the bone, *S. aureus* can form biofilms, which help it to survive antibiotic treatment through tolerance (15,41). In addition to biofilm formation, *S. aureus* can also form staphylococcal abscess communities (SACs), which often manifest in the bone marrow (15). The SAC is made of a fibrin pseudocapsule and is surrounded by neutrophils, which are unable to access the bacterial community sheltering within (42). SACs can compromise blood flow, leading to greater bone necrosis and sequestrum formation, thus creating a vicious cycle of bacterial persistence (11,15). Additionally, *S. aureus* can invade the cortical bone, reaching into the deeper region where mechano-sensing osteocytes live. This is known as the osteocyte lacuno-canalicular network (OLN) (43,44).

Within the OLN, *S. aureus* is shielded from antibiotics (15). *S. aureus* factors, including penicillin binding protein 4, allow for its invasion of the OLN (45). Thus, defining how specific *S. aureus* factors facilitate abscess formation and infiltration into the OLN is important to the overall understanding of how *S. aureus* causes acute and chronic bone infection. While this dissertation focuses on how host responses to *S. aureus* promote bone damage, building a complete mechanistic understanding of *S. aureus* osteomyelitis also requires further study of how *S. aureus* survives in bone, evades antibiotic killing, and induces bone damage through toxins.

Understanding bone homeostasis and the skeletal niche

Bone is a unique and dynamic tissue

Bone is repaired continuously to maintain structural integrity. In addition to providing structural support, bone also acts as a reservoir for hematopoiesis, which occurs within the marrow of bones including the femur. Thus, bone is a highly dynamic tissue. It is made up of organic material, mainly type I collagen, and the inorganic mineral hydroxyapatite (46). Maintenance of bone homeostasis is performed by a specialized community of skeletal cells including bone-building osteoblasts, bone-resorbing osteoclasts, and mechano-sensing osteocytes. These cells maintain bone homeostasis by ensuring bone loss is balanced by new bone formation (47). The femur is a long bone comprised of cortical and trabecular bone architecture. Cortical bone is a hard shell that encases the bone marrow. It is made up of an outer layer of periosteum and inner layer of endosteum, which interfaces with the bone marrow. Trabecular bone exists at the proximal and distal ends of the femur within the anatomic regions called the metaphyses and epiphyses. It is located under the cortical bone, and it has a lattice-like architecture (48,49). The rate of bone remodeling, or turnover, is higher in trabecular bone than in the cortical bone (50). The femur is the focus of animal model experiments shown in Chapters II and III of this dissertation. In osteomyelitis, the normal processes of bone maintenance are altered to perturb bone homeostasis (11,22,51). **Fig. 1** shows an anatomical diagram of the femur which is useful as a guide for understanding basic bone anatomy and the parameters of bone loss and bone formation that are measured in the upcoming data sections. Assessments of bone parameters including callus formation, cortical bone destruction, and trabecular bone loss are used as means of approximating how infection alters bone homeostasis. The following background sections will detail how osteoblasts and

osteoclasts regulate bone homeostasis and will present osteoclast differentiation in detail, as osteoclasts are the major focus of this dissertation.

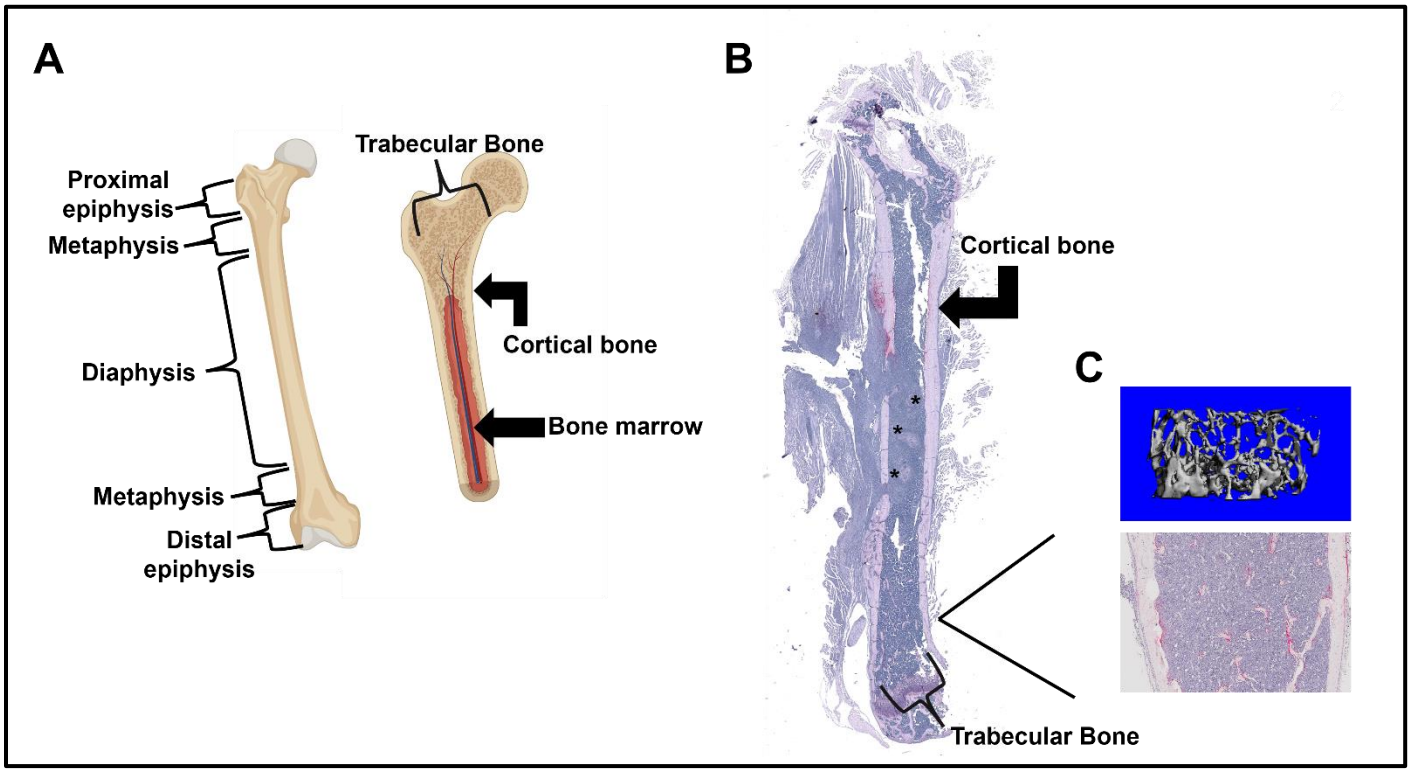

Figure 1. Bone architecture in the femur. A) The femur is made up of two types of bone architecture. Cortical bone comprises the diaphysis of the femur. This bone is a hard shell that encapsulates the bone marrow. Trabecular bone comprises the metaphases and epiphyses. This bone has a spongy architecture. **B)** Image shows a formalin-fixed femur isolated from a mouse that underwent induction of *S. aureus* osteomyelitis. The femur was stained for tartrate-resistant acid phosphatase (TRAP) and imaged at 10X. The arrows show the cortical and trabecular bone regions. The asterisks denote the formation of staphylococcal abscesses in the bone marrow**. C)** These images offer greater detail on the trabecular bone in the distal metaphysis. The upper image shows trabecular bone reconstructed using micro-computed tomography (μCT). The lower image shows a zoomed-in image of trabecular bone from a TRAP-stained femur section.

<u>Osteoclasts and osteoblasts collaborate to maintain bone homeostasis</u>

Bone undergoes regular repair, as microdamage to bone occurs from mechanical loading (52). Osteoblasts and osteoclasts are the major cell types involved in maintaining bone. Osteoblasts arise from the mesenchymal stem cell lineage and differentiate through activation of the master transcription factor RUNX family transcription factor 2 (Runx2) (53). Osteoclasts arise from myeloid precursors in response to the canonical differentiation factor receptor activator of nuclear factor (NF)-κB ligand

(RANKL), discussed in detail in the following section (54). The process of bone repair depends on specific spatial organization of the skeletal cells and is coordinated by numerous secreted and membrane-bound factors, called coupling factors (47). The necessity of spatial proximity and communication between bone repair cells has led to the definition of the bone multicellular unit (BMU), which describes how osteoclasts and osteoblasts convene to conduct the highly coordinated bone remodeling process (55). Bone remodeling begins when osteoclasts start resorbing. Bone resorption can be initiated by secreted factors like sphinogosine-1 phosphate and RANKL (56–58). The large, multinucleated osteoclast utilizes an actin ring to form a sealed zone on the bone called a ruffled border. The adherence between the osteoclast and the bone is facilitated by αvβ3 integrins which localize to form podosomes along the actin ring, creating the sealing zone (59). Osteoclasts pump protons into the sealed zone using the vacuolar-ATPase transporter and this acid breaks down the mineral component of the bone matrix (60,61). Subsequent release of the enzyme cathepsin K serves to break down collagen (62). Secreted coupling factors help osteoclasts sense how much bone resorption has occurred and signal to osteoblasts to begin formation. Additionally, factors like transforming growth factor beta (TGF-β) and insulin-like growth factor-1 (IGF-1) are embedded within the bone matrix and, upon excavation, provide signals to resorbing osteoclasts and awaiting osteoblasts (63,64). For instance, TGF-β negatively regulates osteoclastogenesis and promotes osteoclast apoptosis while activating osteogenic signaling in osteoblasts (65,66). Combinatorial signaling ushers in the next phase of remodeling, known as the reversal stage. Reversal cells remove incompletely degraded collagen and mineral from the bone, essentially cleaning the surface to ready it for new matrix deposition (47). The precise identity of reversal cells has remained elusive, as they do not express clear identity makers. It is suspected that they are mesenchymal cells in the early stage of differentiation into osteoblasts (47,67). Following reversal, mature osteoblasts enter the space and deposit osteoid, or unmineralized bone matrix, onto the resorbed surface. Osteoblasts iteratively mineralize the matrix through hydroxyapatite deposition (47). When bone formation is complete, most of the involved osteoblasts undergo apoptosis. The remaining cells either become quiescent bone lining cells or begin terminal differentiation into osteocytes, which live in the lacunae of the bone (47,67).

Osteoclastogenesis in detail

Differentiation of osteoclast precursors into mature, multinucleated, bone-resorbing osteoclasts occurs through a process known as osteoclastogenesis. Osteoclastogenesis occurs in myeloid/monocyte progenitors, referred to here as osteoclast precursors, in response to RANKL. *In vivo*, osteoblasts and osteocytes are the major cellular sources of RANKL (68–70). Osteoblasts also produce an inhibitory decoy receptor for RANKL called osteoprotegerin (OPG) (71). This is an important mechanism by which osteoblasts influence osteoclast differentiation and function. Cell culture can be used to study factors affecting osteoclastogenesis. In culture, mature osteoclasts form as early as 3 days into culture with RANKL, with many osteoclasts present by day 5 of culture. Osteoclasts are quantified by identifying cells that have 3 or more nuclei and stain positively for tartrate-acid phosphatase (TRAP), an enzymatic protein involved in resorption (72). In addition to counting osteoclasts, the cell fusion and fission events involved in osteoclastogenesis can be visualized in the cell culture plate by microscopy. Imaging studies employing cell-permeable dyes have demonstrated that fusion occurs in a coordinated manner, with specific cells acting as the seed osteoclasts (73,74). For a long time, direct *in vivo* observations of the timing and frequency of osteoclast fusion were not possible due to technical challenges. And, although many field researchers suspected that mature osteoclasts undergo fission as well as fusion *in vivo*, solid evidence of this phenomenon remained enigmatic. Thus, the scientific understanding of osteoclastogenesis was limited to what could be observed in culture plates and bone sections (73,74). The advent of intravital imaging has led to a new understanding of how osteoclastogenesis proceeds in the skeletal system. Using a mouse parabiosis model comprised of transgenic mice expressing fluorescent lineage markers, Jacome-Galarza et al. determined that the initial population of osteoclasts that develops during murine embryogenesis is seeded by cells of the erythro-myeloid lineage. These founding osteoclasts, dubbed syncytia, are replenished over time through fusion of single monocytes into the syncytia. This results in total nuclear replacement every 2 months (75). A subsequent publication by McDonald et al. revealed that osteoclasts cycle between large, more multinucleated, resorbing cells and smaller cells, aptly named osteomorphs. The cycling between these cell states can be controlled by pulsing with soluble RANKL to promote osteomorph fusion to functional osteoclasts (58).

The process of osteoclastogenesis, by which osteoclast precursors undergo differentiation reprogramming through epigenetic and transcriptional changes, requires signaling through three different receptors: the colony-stimulating factor 1 receptor (CSF-1R), the receptor activator of nuclear factor (NF)-κB receptor (RANK), and a co-stimulatory receptor paired with an immunoreceptor tyrosine-based activation motif (ITAM)-containing adapter (59). A summary of the signaling events that drive

osteoclastogenesis is depicted in **Fig. 2**. The CSF-R1 receptor acts first in the differentiation cascade. CSF-R1 is expressed in cells of the myeloid lineage (76). It is activated in osteoclast precursors by the ligand macrophage colony-stimulating factor (M-CSF), which initiates the expression of RANK (77). M-CSF further acts as a differentiation and survival signal in mature osteoclasts (76,78,79). RANK is type I transmembrane protein and tumor necrosis factor (TNF) family member (80). Following its expression on the cell surface, it is bound by RANK ligand (RANKL), a TNF family cytokine (54,81). RANK lacks intrinsic enzymatic activity in its intracellular region and therefore relies on an adapter protein to transduce its signal. The cytoplasmic tail region of RANK has interaction domains compatible with TNF receptor-activating factor (TRAF)-2, TRAF3 and TRAF5 (80,82,83). Despite this, RANK mainly transduces through TRAF6 to induce osteoclastogenic molecular reprogramming (82,84). TRAF6 activates the mitogen-activated protein kinases (MAPK) signaling cascade comprised of extracellular signal-regulated kinase (ERK), c-Jun N-terminal kinase (JNK), and p38 to activate the activator protein-1 (AP-1) transcription factor family (85,86). TRAF6 also activates NF-κB signaling, which is essential for osteoclast formation (84,87). The AP-1 family member c-Fos, in conjunction with NF-κB, initially serves to upregulate transcription of the master regulator of osteoclastogenesis, the transcription factor nuclear factor of activated T cells cytoplasmic 1 (NFATc1) (88–92). Epigenetic changes to the *Nfatc1* gene locus, namely the Jumonji domain-containing 3 (JMJD3)-mediated removal of the repressive methylation marker H3K27me3, are also essential for *Nfatc1* transcription (93). However, transcription of *Nfatc1* alone is not sufficient for the procession of osteoclastogenesis. NFATc1 must be activated via dephosphorylation so it can access the nucleus and bind DNA in an active state (88). Once activated, NFATc1 auto-amplifies signaling by homing to its own promoter (92). It also upregulates transcription of osteoclast-identity genes.

Understanding how NFATc1 becomes activated requires discussion of the final of the three aforementioned receptors required for osteoclastogenesis. Co-stimulation occurs through ITAM-containing adapters including DNAX-activating protein of 12 kDa (DAP12) and/or Fc receptor common γ (Fc-Rγ) (94–98). In mice lacking DAP12 and Fc-Rγ, osteoclasts cannot form, resulting in severe osteopetrosis (96). Neither DAP12 nor Fc-Rγ have ligand-binding domains, and so these adapters work in concert with a selection of co-receptors. DAP12 can associate with co-receptors including triggering receptor expressed on myeloid cells-2 (TREM-2), myeloid DAP12 associated lectin or CLEC5A (MDL-1), or sialic acid-binding immunoglobulin-like lectin 15 (Siglec-15) (94,98). Fc-Rγ can associate with osteoclast activating factor (OSCAR) or paired immunoglobulin-like receptor A (PIR-A) to promote osteoclastogenesis (94,95,97). Fc-Rγ can also associate with Fc receptors FcγRI, FcγRIII and FcγRIV, although the consequences of signaling through these is not fully understood and may in some cases

be inhibitory rather than osteoclastogenic (94). Calcium efflux occurs downstream of co-stimulation to ultimately induce dephosphorylation and activation of NFATc1. Calcium signaling occurs through spleen tyrosine kinase (Syk), which interacts with the phosphorylated tyrosine residues on the ITAM adapter of DAP12 or Fc-Rγ and subsequently activates phospholipase C γ (PLCγ) (99). Inositol 1, 4, 5-triphosphate (IP_3) then potentiates Ca^{2+} release from the ER. Calmodulin becomes activated in response to the surge in Ca^{2+} and in turn activates the phosphatase calcineurin to induce NFATc1 dephosphorylation and translocation to the nucleus (99,100). NFATc1 upregulates the transcription of many osteoclast-identity genes including genes coding for TRAP, OSCAR, and cathepsin K. (89). Ultimately, differentiating osteoclasts fuse to form large, multinucleated cells (74). In Chapter III, I will test how progression from monocyte to osteoclast alters cellular capacity to activate the inflammasome. Understanding the molecular events that underlie osteoclastogenesis is important when considering how inflammasome regulation may be governed in this specific population of cells.

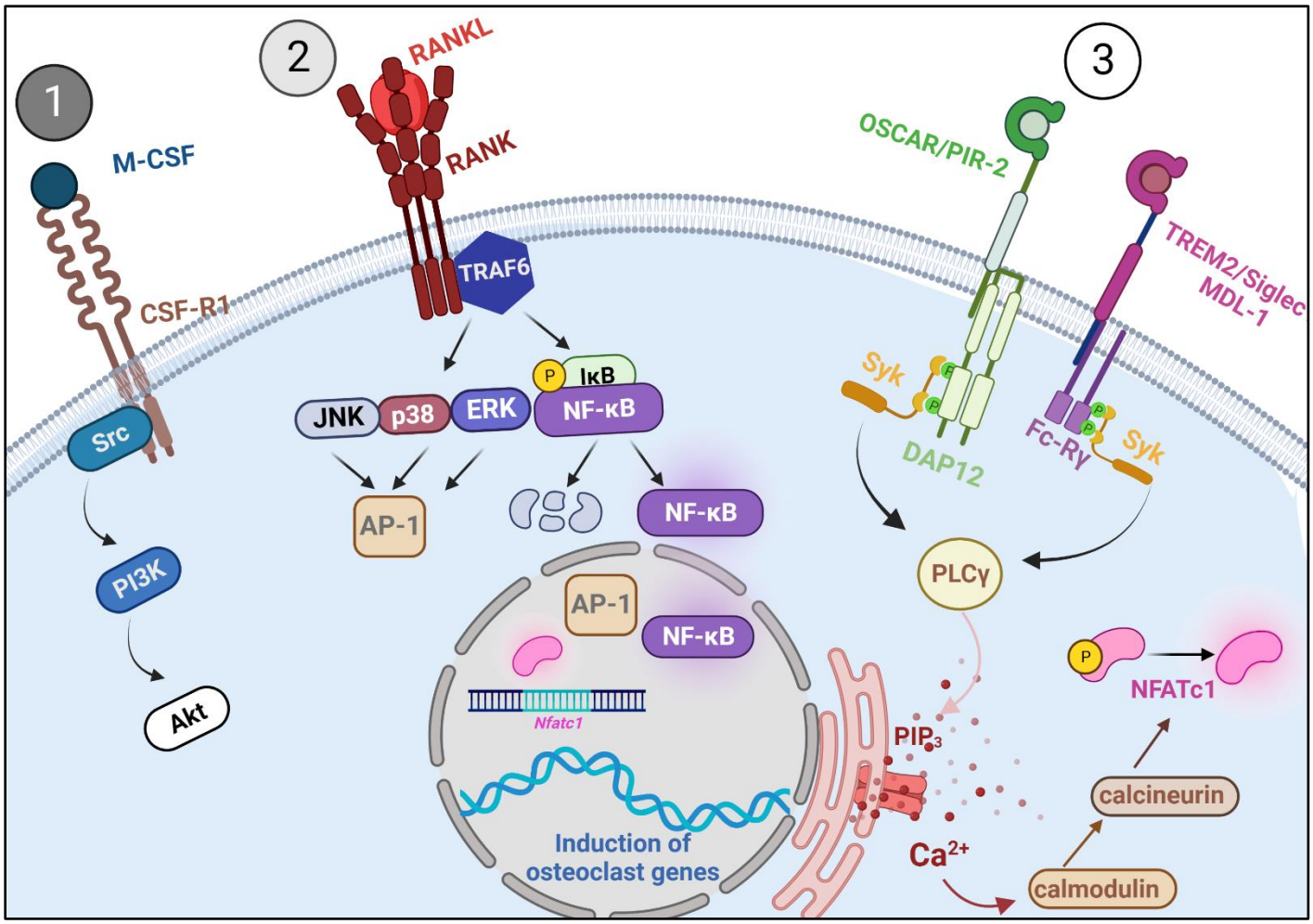

Figure 2. Overview of signaling pathways controlling osteoclastogenesis. 1) Signaling through the colony-stimulating factor 1 receptor (CSF-R1) by macrophage colony-stimulating factor (M-CSF) results in the recruitment and phosphorylation of Src by the intrinsic tyrosine kinase activity in the cytoplasmic tail of CSF-R1. Src activates phosphatidylinositol 3-kinase (PI3K), which in turn activates the kinase Akt to drive survival, differentiation, and actin reorganization. CSF-R1 signaling is responsible for inducing expression of receptor activator of nuclear factor (NF)-κB (RANK). **2)** When RANK is bound by its ligand, RANK ligand (RANKL), it transduces its signal through the adapter TNF receptor-activating factor 6 (TRAF6). This results in activation of the mitogen-activated protein kinases (MAPK) c-Jun N-terminal kinase (JNK), p38, and extracellular signal-regulated kinase (ERK), leading to activation of the component of activator protein-1 (AP-1) family of transcription factors. TRAF6 also drives activation of the NFκB transcription factor family. Together, these transcription factors activate expression of osteoclastogenic genes. **3)** Activation of nuclear factor of activated T cells c1 (NFATc1) gene transcription is a critical outcome of RANK signaling. Subsequently, co-stimulation occurs through paired transmembrane immunoreceptor tyrosine-based activation motif (ITAM)-containing adapter [Fc receptor common γ (Fc-Rγ) or DNAX-activating protein of 12 kDa (DAP12)] and a co-receptor. Phosphorylation of the ITAM results in recruitment and activation of spleen tyrosine kinase (Syk) to activate phospholipase C γ (PLCγ). PLCγ causes inositol 1, 4, 5-triphosphate (IP_3) to open a channel in the endoplasmic reticulum (ER) to allow Ca^{2+} efflux. This activates calmodulin and calcineurin to dephosphorylate NFATc1. Upon activation, NFATc1 drives expression at its own promoter and induces expression of osteoclastogenic gene programming. Figure made with BioRender.com.

Osteo-immune crosstalk during *S. aureus* osteomyelitis

Osteoimmunology informs the study of bone infection

The importance of bone is two-fold; it acts as an adaptable scaffold for movement while also serving as a repository for hematopoiesis. Bone's functional duality results in a dynamic and diverse microenvironment where skeletal cells and immune cells live in proximity. This has led to the development of the scientific field of osteoimmunology, which is dedicated to studying how immune cells and bone cells interact and influence one another. Efforts in this field have identified fundamental osteo-immune interactions that govern the physiologic maintenance of bone homeostasis and the hematopoietic niche. In this section, I detail osteo-immune interactions that may influence bone homeostasis during osteomyelitis.

Multifactorial causes of bone damage in osteomyelitis

Bone damage manifests in osteomyelitis through alterations to bone homeostasis. This can result from staphylococcal toxins that directly kill bone cells, as discussed in the earlier part of this chapter. Inflammation generated by the immune response to pathogen can also, paradoxically, drive the dysregulation of bone homeostasis (22). Despite bacterial persistence, the immune response within the infected femur leads to significant inflammation (101). In part, inflammation causes altered differentiation and function of resident skeletal cells like osteoclasts and osteoblasts, manifesting as bone loss and aberrant bone formation (102). Callus formation, indicative of fracture healing and of a sub-periosteal reaction, correlates with higher bacterial burdens (16). However, stimulation of the bone using only bacterial wall components is sufficient to induce osteogenesis, suggesting that inflammation resulting from cell sensing of bacteria induces callus formation directly (103). Our group has identified the interleukin-1 type 1 receptor (IL-1R1) signaling pathway as a driver of osteoclastogenesis and of parallel bone loss in the trabecular bone during *S. aureus* osteomyelitis. Our results suggest this signaling pathway also influences callus formation, which is increased in osteomyelitis in IL-1R1-deficient mice (51). The next section will discuss potential mechanisms by which host-sensing of bacteria and cytokine responses perturb bone homeostasis through altered osteoclast differentiation and function. This is relevant to Chapters II and III, which present data on how specific innate immune pathways influence changes to bone homeostasis during osteomyelitis.

Inflammatory stimuli influence osteoclast differentiation and function

Mature osteoclasts and their progenitors are exquisitely responsive to changes in cytokine milieu, and specific cytokines are known to promote bone loss in numerous inflammatory bone diseases (102). Inflammatory cytokines like TNFα, interleukin-6 (IL-6), and interleukin-1 beta (IL-1β) promote bone loss through osteoclast-mediated joint erosion in arthritis (102,104–107). The TNFα blocking antibody infliximab is commonly used to treat severe rheumatoid arthritis (106). Cytokines like TNFα and the IL-1R1 cytokines IL-1β and IL-1α are also important in promoting immune cell responses to *S. aureus* (108–111). Importantly, these cytokines are thought to drive inflammatory bone loss in part by acting upon osteoclasts to increase differentiation and resorption (102,107). IL-1α/β promote osteoclast differentiation by amplifying NFATc1-driven differentiation programming in cells that have been exposed to permissive levels of RANKL (112,113). TNFα increases osteoclastogenesis by initiating IL-1R1 cytokine and RANKL production in stromal cells, which positively regulates osteoclastogenesis (114,115). Additionally, these same cytokines can inhibit osteoclastogenesis in certain contexts. If a monocyte precursor is exposed to an osteoclastogenic cytokine like TNFα before sufficient RANKL exposure, the cell will differentiate into a macrophage, adopting an inflammatory M1 phenotype (116). There are also cytokines that inhibit osteoclastogenesis even when a precursor cell has already been primed by RANKL, including interleukin-4 (IL-4) and interleukin-10 (IL-10) (117,118). In addition to altering differentiation, cytokines can also modulate osteoclast function by promoting resorption. Exposure to IL-1β during osteoclastogenesis results in a pathologic resorptive phenotype wherein mature osteoclasts resorb more bone. This proceeds without a parallel increase in expression of kindlin-3 and talin-1, adhesion molecules normally used in resorption (119). This study exposes the possibility that osteoclasts differentiating during inflammation may be reprogrammed to resorb more bone in a non-canonical manner. Cytokine elaboration from macrophages also drives increased resorption in *S. aureus*-infected osteoclast cultures (120). Thus, cytokine responses potentiated by infection are highly influential to the differentiation and function of osteoclasts. In Chapter III, I will explore this topic further by interrogating elaboration of IL-1R1 cytokines by osteoclast lineage cells as a potential mechanism of bone loss during osteomyelitis.

In addition to cytokine responses, pattern-recognition receptor (PRR) ligation can directly influence osteoclast progenitor cell fate decisions and promote resorption by mature cells. Toll-like receptors (TLRs) are a type of PRR known to influence osteoclasts. TLRs are involved in host detection of *S. aureus*, and this will be discussed as length in the next section. At the RNA level, osteoclast precursors express TLRs 1-9 and mature osteoclasts express TLR2 and TLR4 (121). There is not clear consensus as to which TLRs are fully functional in mature, resorptive osteoclasts, but TLR potentiation

does impact differentiation in precursors. If an osteoclast is stimulated with a TLR agonist prior to sufficient RANKL exposure, this directs differentiation toward the macrophage rather than osteoclast fate (122–128). However, stimulation with a TLR2, 4, or 9 agonist during or following sufficient RANKL exposure will propel the precursor toward the osteoclast fate and increase overall osteoclast formation (126,127,129,130). This effect is strongest when two different TLR signals are combined (126). C-Fos and NFκB activation are increased by strong TLR agonism following RANKL-priming, suggesting that TLR ligation activates osteoclastogenic signaling, potentially due to convergence on TRAF6 (126,129). Moreover, TLR2 agonism significantly increases resorption by osteoclasts cultured on dentin chips (130). In Chapter II, I will explore whether TLR signaling influences the osteoclast differentiation response to staphylococcal culture supernatants or infection with live *S. aureus*.

The role of Toll-like receptor signaling in *S. aureus* infection

Overview of Toll-like receptors 2 and 9

Toll-like receptors (TLRs) are type I transmembrane proteins that require receptor homo- or hetero- dimerization to initiate downstream signaling events. Mice and humans have 11 and 13 types of TLRs, respectively (131). TLRs act as pattern recognition receptors (PRRs) to detect a broad array of damage- and pathogen-associated molecules (131,132). TLR2 and TLR9 both detect molecules relevant to Gram-positive bacterial infection (131). TLR2 dimerizes with TLR1 and/or TLR6 to detect tri- and di-acylated bacterial lipoproteins, respectively (133,134). TLR9 is localized to the endosome and detects unmethylated CpG-DNA (135). For all TLRs except TLR3, the adapter protein myeloid differentiation marker 88 (MyD88) facilitates signal transduction from the dimerized TLR. MyD88 is also required for signal transduction by the IL-1R1 (136). TNF receptor-activating factor-6 (TRAF6) is activated downstream of MyD88 and drives the activation of NFκB transcription factor family (137). In addition to NFκB, TLR9 can also activate the type I interferon response (138). When TLR2 signals from the endosome following receptor endocytosis it can also activate the type I interferon response (139). Thus, TLR activation by pathogen- or damage-associated molecules results in the initiation of immune responses. Many immune cells including macrophages, dendritic cells, and neutrophils express TLR2 and TLR9 (140). There is also evidence to support that osteoclast lineage cells express TLR2 and TLR9 (121,126). A major focus of Chapter II is to define the role of TLR2 and TLR9 signaling in promoting bacterial burden control and driving bone damage during *S. aureus* osteomyelitis.

Toll-like receptors 2 and 9 in the host response to *S. aureus*

TLR2 and TLR9 enable host detection of *S. aureus* to initiate downstream innate immune responses. Thus, loss of these detectors is expected to be deleterious to host antibacterial defenses. Despite this, the results of studies aimed at defining the roles of TLR2 and TLR9 in *S. aureus* infection have yielded mixed results. In the case of TLR9, polymorphisms that reduce TLR9 expression in humans are associated with increased rates of nasal carriage of *S. aureus* (141). Complimentary studies in cell culture and animal models are limited in number and have not sufficiently expanded upon this observation. A 2012 study by Parker and Prince showed that detection of *S. aureus* by TLR9 induced the type I interferon response in dendritic cells. In a mouse model of *S. aureus* lung infection, this TLR9-mediated response reduced host ability to clear infection (138). Far greater attention has been paid to elucidating the role of TLR2 in the host response to *S. aureus*. Cell culture studies revealed that WT and *Tlr2*$^{-/-}$ macrophages have similar rates of internalization, suggesting phagocytosis is not entirely dependent on TLR2 (142,143). Following treatment with heat-killed *S. aureus*, release of pro-inflammatory cytokines like IL-6 and TNFα is reduced in *Tlr2*$^{-/-}$ macrophages compared to WT macrophages (142). However, the cytokine measurements reported are well over baseline in *Tlr2*$^{-/-}$ cells, suggesting that the decrease may not be substantial enough to impair the immune response. Like the findings of Parker and Prince on TLR9, *Tlr2*$^{-/-}$ macrophages have been reported to better control intracellular replication of live *S. aureus*, as *S. aureus* can prevent oxidative burst in the phagolysosome in a TLR2-dependent manner (139,143). The most definitive argument for the beneficial role of TLR2 in host response to *S. aureus* can be found in work comparing survival of WT and *Tlr2*$^{-/-}$ mice undergoing septic infection. At a range of 1-3 x 10^7 CFU administered intravenously, TLR2 deficient mice incur increased mortality and increased bacterial burdens compared to WT controls over a 14-day infection (144). Subsequent studies in lung and skin are contradictory, finding that TLR2 is not essential to bacterial containment (108,139,143,145). Whether TLR2 is critical to host survival or bacterial containment in *S. aureus* osteomyelitis is not known.

In addition to examining how loss of TLR2 affects infection outcome, complimentary approaches have aimed to test how bacterial pathogen production of TLR2-activaitng lipoproteins influences disease pathogenesis. A Δ*lgt* mutant lacking the lipoprotein diacylglycerol transferase gene, which codes for the enzyme that catalyzes the first step in the formation of mature lipoproteins, has been used to study how altered production of TLR2 ligands by *S. aureus* influences infection outcome. Studies with this strain yielded contradictory results. While Wardenburg et al. found that the Δ*lgt* strain caused more severe infection due to immune evasion, Schmaler et al. demonstrated that the mutant strain causes less severe infection due to a growth defect attributed to inadequate iron acquisition

(146,147). It is likely that different strain backgrounds contributed to the disparate findings. In humans, reduced TLR2 expression correlates with increased mortality risk during septic infection (148). However, mutations affecting TLR2 expression and heterozygous inactivating mutations are not associated with increased risk of *S. aureus* infection overall (149,150). Thus, more research is needed to ascertain whether TLR2 and TLR9 are drivers of a productive host response or whether *S. aureus* manipulation of TLR signaling turns these detection mechanisms against the host.

The relevance of the NLRP3 inflammasome to *S. aureus* osteomyelitis

Inflammasome overview

Inflammasomes are multiprotein complexes that assemble and activate in response to broad pathogen- and damage-associated stimuli. There are many types of inflammasomes, including NLRP1, NLRP3, NLRC4, Pyrin, and AIM2, named for the unique sensor protein employed. The sensor acts as a PRR which induces assembly and activation of the multiprotein inflammasome complex (151,152). The complexity of the signals controlling inflammasome activation and downstream effects make it difficult to generalize about the commonalities of these different sensor-based systems. I chose to narrow the focus of the following sections to the nucleotide binding and oligomerization, leucine-rich repeat, pyrin domain-containing 3 (NLRP3) inflammasome. NLRP3 can respond to broad, damage-related stimuli and has demonstrated relevance to *S. aureus* infection (27,28,31,153–159). The NLRP3 inflammasome requires two signals for activation: a priming signal through a TLR or tumor necrosis factor receptor (TNFR) and an activating 2nd signal detected by the inflammasome sensor (160,161). The result of inflammasome induction is activation of caspase-1 which then activates IL-1β and interleukin 18 (IL-18) and, in some cell types, induces death by pyroptosis (162–164). The absent in melanoma 2 (AIM2) inflammasome, also caspase-1-dependent, is activated by *S. aureus* through sensing of bacterial DNA, and thus is also of potential importance to *S. aureus* osteomyelitis but is not the chosen focus of this dissertation (165). This background section is relevant to Chapter III, which interrogates how inflammasome-mediated maturation of IL-1β influences the dysregulation of bone homeostasis during *S. aureus* osteomyelitis.

NLRP3 overview

The NLRP3 inflammasome is a multi-protein complex comprised of a N-terminal pyrin domain (PYD), a central NAIP, CIITA, HET-E, and TP1 (NACHT) domain, and a C-terminal leucine-rich repeat (LRR) domain (152,162). The assembled NLRP3 complex is comprised of the adapter protein apoptosis-associated speck-like protein containing CARD (ASC), the cysteine protease caspase-1, and the regulatory protein NIMA-related kinase 7 (NEK7) (**Fig. 3**). The NLRP3 inflammasome is expressed by immune cells like macrophages, neutrophils, and dendritic cells and in some resident tissue cells like epithelial cells (164,166–169). When active, the NLRP3 inflammasome liberates the cysteine protease activity of caspase-1 by positioning it in an energetically favorable state, allowing it to auto-activate through self-cleavage (170,171). Active caspase-1 remains within the complex where it cleaves target proteins including the pro forms of inflammatory cytokines IL-1β and IL-18, which are activated by cleavage (162,164). In some cell types including macrophages, caspase-1 also cleaves gasdermin D into the N-terminal p31 fragment to induce pyroptotic cell death (163). The highly pro-inflammatory consequences of NLRP3 activation can be disastrous if unrestrained, as is the case in cryopyrin-associated autoinflammatory syndrome (CAPS), an inflammatory disorder caused by a gain of function mutation in the *Nlrp3* gene (172). Due to the risk of generating excessive inflammation, there are numerous regulatory mechanisms that prevent unnecessary deployment of the inflammasome's explosive potential. To understand the positive and negative regulatory signals that control NLRP3 activation, it is useful to consider NLRP3 activation as a two-step process. Although this two-step model admittedly simplifies the complexity of NLRP3 activation, I employ it in the following section as a tool for understanding common elements that control NLRP3 in many cellular contexts.

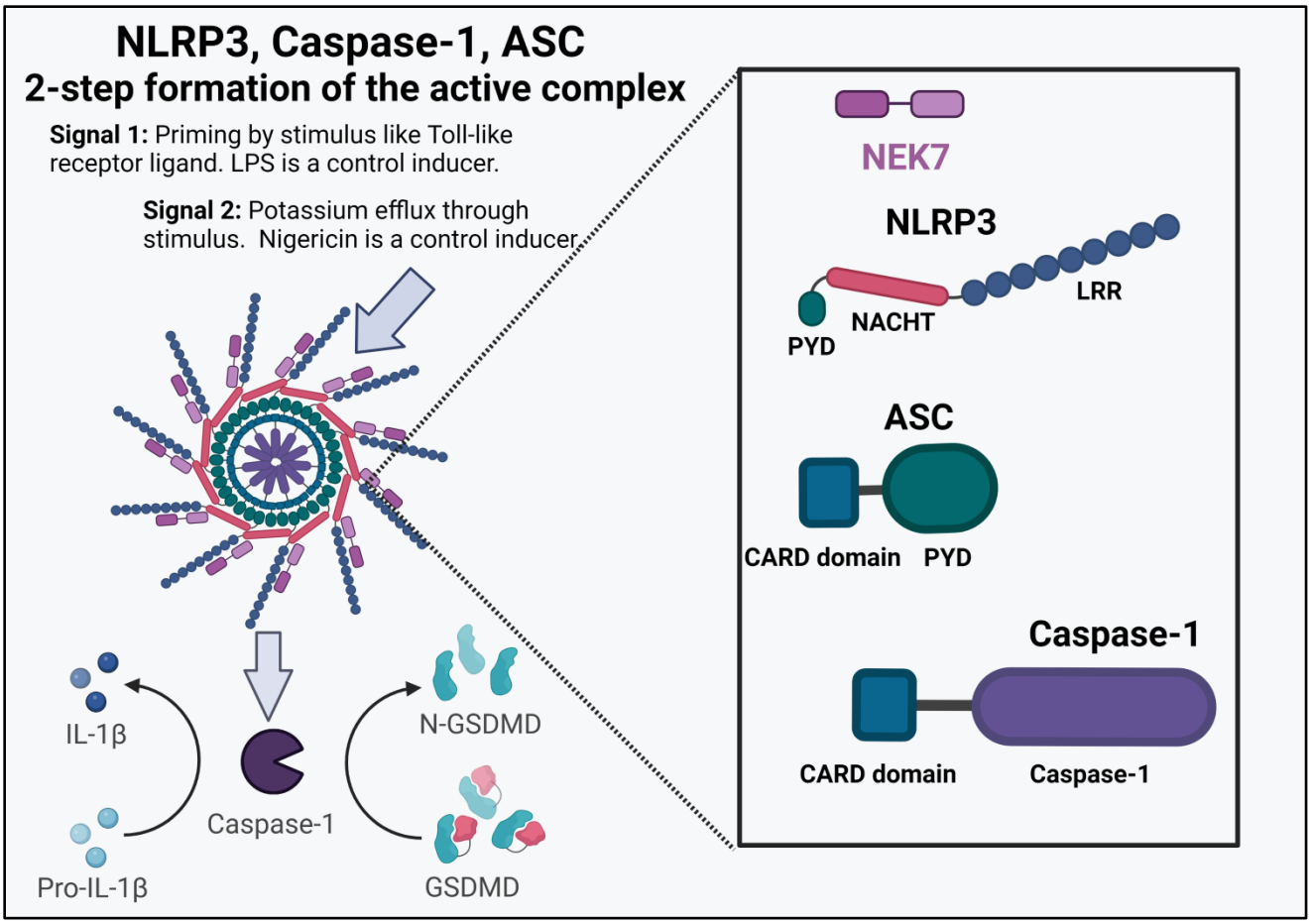

Figure 3. Overview of the NLRP3 inflammasome. The nucleotide binding and oligomerization, leucine-rich repeat, pyrin domain-containing 3 (NLRP3) inflammasome is made up of the NLRP3 sensor, apoptosis-associated speck-like protein containing CARD (ASC) adapter, NIMA-related kinase 7 (NEK7), and caspase-1. Assembly occurs in response to a priming signal followed by a 2nd, activating signal. Upon 2nd signal, the protein components oligomerize. ASC and caspase-1 interact through CARD domains. ASC and NLRP3 bind together through interactions in the pyrin (PYD) domains. Figure made with BioRender.com.

NLRP3 activation and assembly

The two-step NLRP3 activation model is comprised of a priming signal and an activation signal. Priming readies the inflammasome for activation by inducing transcription and translation of the protein components and by altering post-translational modifications that inhibit complex assembly (151). The priming signal can come through a stimulus that activates a PRR such as a TLR or through a cytokine receptor like the TNFR. Receptor signaling potentiates NFκB signaling to upregulate gene transcription and translation of inflammasome components like NLRP3 and IL-1β (160,161). In cell culture models, TLR agonists including lipopolysaccharide (LPS) are standard priming agents. Sufficient priming time is required for protein synthesis to take place, and so in cell culture assays, a 3-4 h window is utilized for priming (173). After priming, a 2nd signal stimulus activates the NLRP3 sensor. Although stimuli like reactive oxygen species and pH changes can act as the 2nd signal, in bacterial infection, K^+ efflux out of the cell is thought to be the commonality between all effective 2nd signal stimuli (174). In cell culture studies, commonly used K^+ efflux-inducing stimuli include the ionophore nigericin and ATP (173,175). Studies presented in Chapter III utilize LPS followed by nigericin. Mechanistically, the exact sequences of molecular events enabling NLRP3 assembly following 2nd signal are still being elucidated. It is known that the trans-Golgi network must be dispersed prior to NLRP3 complex assembly. The dispersed trans-Golgi network acts as a scaffold onto which NLRP3 docks and assembles with ASC, caspase 1, and, in some cases, NEK7 (176). The signals that control trans-Golgi dispersal are still being explored.

The temporal framework laid out for priming and the mechanism by which the 2nd signal activates assembly of NLRP3 are subject to change based on the cellular context. For example, NLRP3 activation can occur without new gene transcription or protein synthesis in a manner known as fast priming. This is an interleukin-1 receptor-associated kinase 1- (IRAK-1) dependent mechanism allows for a short priming of 10 min with LPS followed by NLRP3 activation upon stimulation with a 2nd signal (177–179). Fast priming is known to occur in human and murine macrophages (178–180). Moreover, in human cells the molecular mechanism underlying 2nd signal initiation of fast priming relies on NEK7-mediated recruitment of NLRP3 to the trans-Golgi network. However, prolonged exposure to LPS renders NEK7 obsolete and instead utilizes IκκB (181). Despite the evolving mechanistic understanding of inflammasome activation, it remains generally universal that NLRP3 activation requires a TLR or TNFR signal followed by damage-associated stimulus. It is important to utilize the working model for NLRP3 activation as a framework rather than an absolute; inflammasome activation varies based on the specific stimuli of interest and the distinct cell type being studied. This is important when considering the data presented in Chapter III, wherein I begin to define the mechanism of inflammasome induction in osteoclasts, for which the inflammasome has not been previously characterized.

Negative regulation of NLRP3

Negative regulation through post-translational modifications to NLRP3, caspase-1, ASC, and the regulatory protein NEK7 can control inflammasome induction by restricting substrate cleavage or assembly (151). There are many types of post-translational modifications that regulate NLRP3 assembly and here I will discuss some of the major known modifications. For instance, NLRP3 is heavily ubiquitinated in its inactive state and thus activity of a de-ubiquitinating enzyme (DUB) is required for activation. LPS stimulation through TLR4 leads to the activation of the DUB BRCA2 containing complex subunit 3 (BRCC3). This induces the removal of the K63-linked ubiquitin from NLRP3 and is essential for the oligomerization of NLRP3 (182). Additional modifications to NLRP3 include phosphorylation and sumoylation. For instance, the phosphorylation of NLRP3 at human serine 198 and mouse serine 194 by c-Jun N-terminal kinase 1 (JNK1) is vital for NLRP3 self-binding and subsequent inflammasome induction (183). Additionally, both caspase-1 and IL-1β can be negatively or positively regulated by phosphorylation and ubiquitination (151). Caspase-1 self-cleaves its p46 inactive form to activate its catalytic C-terminal domain. The cleavage event results in a p10 protein which is not catalytically active and the C-terminal p33 fragment. These dimerize with another set of caspase-1 p10/p33 proteins. All of this occurs while caspase-1 is still assembled in the NLRP3 complex. In this form, caspase-1 activates its targets. A final cleavage event removes the CARD domain from the p33 to release the p20/p10 fragments from the complex. These de-dimerize and, because they are unstable when not associated, they rapidly degrade. Thus, the sites that caspase-1 self-cleaves ultimately function to both activate and shut off catalytic activity of the complex (170). Recently, a regulatory role for gasdermin D was identified by Hu et al. The cleaved N-terminal fragment can bind caspase-1 via the RFWK residues of the β1-β2 loop, thus acting to negatively regulate caspase-1 (184). In addition to modifications of the proteins of the inflammasome, negative binding proteins exist human cells (184). The PYD-only proteins (POPs) family of proteins regulate inflammasome components through direct binding (185–187). Whether a similar mechanism exists in murine cells is not yet known.

The role of the inflammasome in bone homeostasis

The link between IL-1R1 cytokines IL-1α and IL-1β and the skeletal system has been appreciated for decades. Before the IL-1β gene was cloned, it was sometimes referred to as osteoclast activating factor because stimulating differentiating osteoclast precursors with IL-1α/β significantly increases osteoclast formation (188,189). Mechanistically, IL-1R1 transduces its signal through the adapter TRAF6 to promote the activity of the transcription factors cFos and microphthalmia-associated transcription factor (MITF), thus driving osteoclast differentiation programming (112,190). Interestingly,

chronic recurrent multifocal osteomyelitis (CRMO), an inflammatory bone disease, can be caused by underlying mutations in genes that regulate IL-1R1 signaling and by gain-of-function mutations in *Nlrp3* (191). Mice engineered to have constitutively active NLRP3 incur bone lesions and increased osteoclastogenesis (192,193). While studies examining the role of IL-1R1 cytokines in inflammatory bone loss have been numerous, attention has only recently shifted toward the study of how IL-1β-activating inflammasomes contribute to damage in bone infection. For instance, Zhu et al. demonstrated that protein levels of NLRP3 and gasdermin D are increased in samples from patients undergoing debridement surgery to treat *S. aureus* osteomyelitis compared to samples from femoral neck repair (194). *In vitro* work in the same publication suggested NLRP3 inhibition may have efficacy in reducing osteoclast formation during infection (194).

In the data presented in Chapter III, I examine how osteoclast differentiation influences cellular capacity to activate the NLRP3 inflammasome. The potential importance of this work is highlighted by several recent publications that establish a role for inflammasome activation in bone healing and identify a link between protein components of the inflammasome and regulation of osteoclast function. Firstly, Sun et al. demonstrated that mice deficient in gasdermin D have reduced healing in femur fractures as measured by increases to osteoclast abundance, delays in callus deposition, and reduced biomechanical measurements of bone stability at 28 days post-injury. The phenotype of gasdermin D-deficient mice mirrored that of IL-1R1-deficient mice, suggesting a cooperative relationship between gasdermin D and cytokine function (195). Interestingly, a regulatory role for gasdermin D in osteoclasts was recently identified in a publication by Li et al. This work revealed that osteoclasts express many caspases as well as gasdermin D. Differential cleavage of gasdermin D by RIPK1/caspase-8/caspase-3 results in a p20 fragment unique to mature osteoclasts. The p20 form serves an essential regulatory function by controlling acidification of the endo-lysosome to limit resorption. Mice deficient in gasdermin D experience exacerbated bone loss in a model of ovariectomy-induced osteoporosis (196). Interestingly, unlike Sun et al., Li et al. reported that gasdermin D-deficient mice have lower bone mass at baseline (195,196). These findings are intriguing because they demonstrate roles for inflammasome-related pathways in bone homeostasis. Specifically, because I am interested in understanding inflammasome activation in osteoclasts, the findings of Li et al. serve as important rationale for my studies. Not only is gasdermin D present in osteoclasts as a regulatory protein, but osteoclasts also express high levels of other caspases (196). Moreover, excessive bone particles activate inflammasome responses in myeloid lineage cells to promote osteoclast differentiation (197). Thus, there is ample opportunity and importance in elucidating how these proteins function in differentiating and mature osteoclasts.

The NLRP3 inflammasome in *S. aureus* infection

To understand the potential role of the NLRP3 inflammasome in the host response to *S. aureus* osteomyelitis, a focus of Chapter III, I will review some of the major findings on the role of NLRP3 in other infection models. Efforts to understand how inflammasome activation occurs in *S. aureus*-infected macrophages were rooted in the observation that the staphylococcal toxin hemolysin-α (Hla) induces both cytokine release and death in macrophages (198). Follow up work demonstrated that Hla acts as a second signal for NLRP3 activation in both human and mouse cells (27,28). The NLRP3-inducing effect of Hla is greatest when cells are treated with *S. aureus* culture supernatant rather than infected with live bacteria (27). Additional studies aimed to determine the molecular mechanism underlying NLRP3 activation in *S. aureus*-infected macrophages, and this led to a more nuanced understanding of how *S. aureus* interacts with and manipulates its host. Caspase-1 activation upon intracellular infection can facilitate acidification of the phagolysosome and oxidative burst (154). Paradoxically, it has also been reported that NLRP3 activation prevents macrophage killing of bacteria due to Hla-mediated inhibition of phagosome acidification (153). Thus, expression levels of Hla in specific strains may ultimately determine whether NLRP3 activation helps or harms the host cell.

Mouse studies to determine the cytokines that drive the immune response to *S. aureus* have pointed to IL-1β as a major driver of neutrophil and macrophage mediated responses (51,108–111). In implant associated infection, TNFα and IL-1β are essential for control of implant-associated infection (111). Whether the NLRP3 inflammasome is the major driver of the IL-1β response to *S. aureus* is not yet clear. In a biofilm-associated craniotomy infection, TLR2 drives caspase-1-dependent responses which are critical to bacterial containment (199). A study by the same group demonstrated an important role for the AIM2 rather than the NLRP3 inflammasome in a brain abscess model of *S. aureus* infection, stressing the need to also consider NLRP3-independent mechanisms (200). Work in models of lung infection suggest dichotomous roles for the cytokine-activating versus cell death-inducing consequences of inflammasome induction. For instance, in a model of *S. aureus* pneumonia, NLRP3-deficiency significantly reduces tissue injury in an IL-1R1-independent manner (31). Thus, while cytokine elaboration promotes immune cell recruitment and activation, other inflammasome-induced events like pyroptosis may be deleterious, offering a potential druggable pathway. Studies addressing the specific inflammasome responsible for mediating host responses in the bone will be pivotal to understanding how IL-1R1 signaling drives bacterial containment and how this influences bone homeostasis. Towards this open question, in Chapter III, I interrogate the role of the NLRP3 inflammasome and its downstream effectors in bone homeostasis in a mouse model of post-traumatic osteomyelitis.

A version of the following section (Chapter II: Context-dependent roles for Toll-like receptors 2 and 9 in the pathogenesis of *Staphylococcus aureus* osteomyelitis) was originally published in *Infection & Immunity* (October 2022).

Petronglo JR, Putnam NE, Ford CA, Cruz VC, Curry JM, Butrico CE, Fulbright LE, Johnson JR, Peck SH, Fatah SR, and Cassat, JE. Context dependent roles for Toll-like receptors 2 and 9 in the pathogenesis of *Staphylococcus aureus* osteomyelitis. *Infect. Immun.* 2022; 90(11).

DOI: 10.1128/iai.00417-22

CHAPTER II: CONTEXT-DEPENDENT ROLES FOR TOLL-LIKE RECEPTORS 2 AND 9 IN THE PATHOGENESIS OF *STAPHYLOCOCCUS AUREUS* OSTEOMYELITIS

Introduction

Staphylococcus aureus is the most common causative agent of infectious osteomyelitis, or infection of bone (3,7). A major pathologic feature of osteomyelitis is dysregulated bone homeostasis and consequent bone damage (5,11,201). In healthy skeletal tissue, bone-building osteoblasts and bone-resorbing osteoclasts balance the deposition of new bone matrix with the resorption of old bone, thus maintaining bone homeostasis (202,203). Perturbation of bone homeostasis during osteomyelitis leads to bone loss and aberrant bone healing and contributes to morbid complications, including pathologic fractures (1,5,201). Moreover, vascular damage occurring in response to infection can interfere with antibiotic delivery, thereby promoting chronic infection (1,5,11). Thus, in addition to prolonged antibiotic therapy, patients suffering from osteomyelitis often require invasive surgical debridement to remove infected and necrotic bone (1,5,7,201). To develop new therapeutic strategies that reduce morbidity and improve antibiotic treatment of osteomyelitis, it is crucial to define the mechanisms by which bacterial infection incites bone damage. Thus, this chapter focuses on defining how innate immune signaling, specifically through Toll-like receptor (TLR) sensing of *S. aureus*, influences pathologic bone remodeling during osteomyelitis.

In inflamed bone, osteoclasts are key mediators of bone loss or osteolysis (102). Increases in osteoclast differentiation (osteoclastogenesis) and bone resorption are recognized mechanisms of pathologic osteoclast activation in inflammatory disease (102,119,204). In physiologic conditions, osteoclastogenesis occurs when precursors of the monocytic lineage encounter the canonical differentiation factor, receptor activator of nuclear factor (NF)-κB ligand (RANKL) (54). RANKL-primed osteoclast progenitors then fuse to form large, multinucleated cells capable of resorbing bone. However, osteoclastogenesis is shaped by stimuli in the bone microenvironment, including engagement of pattern recognition receptors (PRRs) and the cytokine milieu (102,127). Specifically, signaling through TLRs 2, 4, and 9 promotes osteoclastogenesis in RANKL-primed osteoclast precursors (125–127,205). Conversely, TLR signaling prior to RANKL can inhibit subsequent osteoclastogenesis (122,123,125,126). Downstream of TLR signaling, pro-inflammatory cytokines such as IL-6, IL-1β, and TNFα enhance osteoclast differentiation, while other cytokines such as IL-10 are inhibitory (112,115,116,118,206,207). Thus, responses to bacterial infection have the potential to

influence osteoclast formation directly through ligation on progenitor cells, and indirectly by potentiating cytokine release from neighboring cells. Moreover, additional resident skeletal cells, including osteoblasts, also engage TLRs in response to *S. aureus*, which can perturb environmental RANKL and cytokine levels (208–210). In addition to bone loss, bone formation is also altered during osteomyelitis. Impaired healing, abnormal callus deposition, and bone loss are also characteristic of human disease and similarly manifest in animal models of disease (16,103). Therefore, it is important to define how specific innate immune responses to bacterial pathogens disrupt bone homeostasis.

TLR2 and TLR9 have been reported to contribute to the innate immune response during *S. aureus* infection (144,210–213). TLR2 dimerizes with TLR1 and/or TLR6 to detect tri- and di-acylated bacterial lipoproteins, respectively, consequently activating NF-κB signaling (133,134). TLR2 has been shown to promote host survival in septic infection, but its role is less clear in tissue-specific models of infection (108,144,145). TLR9 is localized to endosomal compartments and recognizes unmethylated CpG-DNA (135). Studies on how TLR9 contributes to host defenses during *S. aureus* infection *in vivo* have been limited (138,212,213). Moreover, many *in vitro* studies document the ability of TLR agonists to promote osteoclast differentiation and mature cell resorption, but the understanding of how these receptors impact osteoclastogenesis and bone homeostasis during bacterial infection *in vivo* is more limited. In this study, we investigate the role of TLR2 and TLR9 signaling in the specific context of post-traumatic *S. aureus* osteomyelitis, with a focus on understanding how these immune receptors influence host antibacterial defenses and modulate infection-induced changes to bone homeostasis.

Materials and Methods

Animal use

C57BL/6J mice (Jackson stock #000664) were used for all *in vivo* and *in vitro* experiments that employed wild type (WT) animals as controls. WT control mice used in the osteomyelitis model were ordered from The Jackson Laboratory (Bar Harbor, ME) and delivered to our housing facility 1-2 weeks prior to undergoing surgery. *Tlr9*$^{-/-}$ mice were provided by Dr. Richard Peek (Vanderbilt University Medical Center) and bred in-house via homozygous crosses to generate experimental animals (135). *Tlr2*$^{-/-}$ mice were ordered from Jackson (stock #004650) and either used for experiments following a 1 to 2-week equilibration period or bred to maintain the knockout colony. To generate mice deficient in TLR2 and TLR9 (*Tlr2/9*$^{-/-}$ mice), *Tlr2*$^{-/-}$ and *Tlr9*$^{-/-}$ mice were crossed to yield homozygous offspring.

Offspring were genotyped using Transnetyx, Inc. (Cordova, TN). The *Tlr2/9*$^{-/-}$ colony was subsequently maintained by homozygous breeding. Because these strains were expected to be immunocompromised, *Tlr2*$^{-/-}$, *Tlr9*$^{-/-}$, and *Tlr2/9*$^{-/-}$ mice were housed with sterile bedding and provided sterile food.

Bacterial strains and growth conditions

Experiments were performed the following: *S. aureus* USA300-lineage strain AH1263 (WT) (214), a derivative strain lacking the alpha-type phenol-soluble modulins (Δ*psmα1-4*) (22), a derivative strain lacking alpha-type phenol-soluble modulins and staphylococcal protein A (Δ*psmα1-4* Δ*spa*) (215), or an Δ*lgt* strain lacking the ability to generate mature lipoproteins due to the disruption of the lipoprotein diacylglycerol transferase gene (216). The Δ*lgt* strain, from here on referred to as *lgt*::Tn, was generated in the LAC background by bacteriophage phi-85-mediated transduction of the transposon-disrupted, erythromycin resistance-marked allele from the USA300-lineage JE2 strain (NE1905), which was procured from the NARSA transposon library (216). Bacterial cultures used in both *in vitro* and *in vivo* infection experiments were grown overnight at 37°C in tryptic soy broth (TSB) with shaking at 180 rpm. 10 μg/ml erythromycin was added to the culture media for the Δ*psmα1-4,* Δ*psmα1-4* Δ*spa*, and *lgt*::Tn strains. Bacterial inocula were prepared by back-diluting overnight cultures 1:100 into TSB and then incubating an additional 3 h at 37°C with shaking at 180 rpm. The subcultures were then centrifuged for 5 min at 4,000 x g to pellet cells. The bacterial inoculum was adjusted to the desired concentration by diluting in 1X phosphate-buffered saline (PBS) and measuring optical density. All post-infection CFU were enumerated after growth on trypticase soy agar (TSA) plates.

Preparation of bacterial supernatants

Concentrated bacterial supernatants were prepared as previously reported (43,44). In brief, 1-2 bacterial colonies were inoculated into 250 ml Erlenmeyer flasks containing 50 ml of sterile RPMI medium with 1% casamino acids (Fisher Scientific). Flasks were sealed with rubber stoppers and cultured for 15 h at 37°C with shaking at 180 rpm. To pellet bacteria, cultures were then centrifuged at 4000 x g for 10 min. Supernatants were sterilized using a 0.22 μm polyethersulfone filter and then concentrated to a final volume of ~1.5 ml using an Amicon Ultra 3-kDa nominal molecular weight column (MilliporeSigma, Burlington, MA). Supernatants were again filter sterilized and single-use aliquots were prepared on ice and frozen at −80°C.

Whole bone marrow isolation and bone marrow-derived monocyte enrichment

Whole bone marrow (WBM) was isolated from male WT, *Tlr2*$^{-/-}$, *Tlr9*$^{-/-}$, or *Tlr2/9*$^{-/-}$ mice aged between 8 and 12 weeks. WBM was flushed from femurs using unsupplemented MEM-α medium (Gibco, Waltham, MA), passed through a 100 μM filter, and centrifuged at 1500 rpm x 5 min. Red blood cells were lysed in ammonium-chloride-potassium buffer for 10 min, and then 1X PBS was added to deactivate lysis. Cells were centrifuged again and resuspended in 100% fetal bovine serum (FBS) for counting. WBM cell preparations were then frozen in 10% dimethyl sulfoxide (DMSO) in FBS and stored in liquid nitrogen until ready to use. Cryopreserved vials of WBM cells were rapidly thawed in a 37°C water bath and then washed in MEM-α medium supplemented with 10% FBS and 1X penicillin-streptomycin to remove DMSO. To enrich for bone marrow-derived monocytes (BMDMs), WBM cells were seeded at 8-10 million cells per 10 cm tissue culture-treated dish in MEM-α medium + 10% FBS + 1X penicillin-streptomycin supplemented with macrophage colony-stimulating factor (M-CSF). Supernatant from the CMG14-12 cell line served as the M-CSF source and was added at a vol/vol ratio of 1:5, providing a high dose of M-CSF for positive selection of monocytes (69). After four days of differentiation, BMDMs were scraped off 10 cm dishes and seeded into 96-well tissue culture plates at 50,000 cells / well or into 24-well plates at 250,000 cells / well. All cell cultures were incubated at 37°C with 5.0% CO_2.

Osteoclastogenesis assays

Two osteoclastogenesis assays were used: a pre-commitment assay in which BMDMs are primed with receptor activator of nuclear factor (NF)-κB ligand (RANKL) for 48 h and then stimulated with bacterial supernatant in the absence of RANKL, and a continuous assay in which RANKL stimulation is present during the duration of bacterial stimulation. For each assay, culture medium was as follows: MEM-α + 1X penicillin-ptreptomycin + 10% FBS with CMG14-12 supernatant at 1:20 vol/vol (BMDM maintenance media) or MEM-α + 1X penicillin-streptomycin + 10% FBS with CMG14-12 supernatant at 1:20 vol/vol and 35 ng/ml RANKL (osteoclastogenic media). In the pre-commitment osteoclastogenesis assay, BMDMs were cultured in osteoclastogenic media for 48 h. Then cells were washed once in warm 1X PBS and media were replaced with BMDM maintenance media. 2.5 - 7% vol/vol Δ*psmα1-4* supernatant or 7% vehicle control (1% casamino acids in RPMI) were added to the cells. 4 days later, cells were fixed and stained for tartrate-resistant acid phosphatase (TRAP) and 4′,6-diamidino-2-phenylindole (DAPI), as described below. In the continuous RANKL assay, BMDMs were plated in osteoclastogenic media. On the second day of culture, 2.5 - 9% vol/vol of concentrated supernatants prepared from the Δ*psmα1-4* strain, or a 7% vehicle control (1% casamino acids in RPMI),

were added to the cell monolayers. Medium was changed and supernatants/vehicle were replenished on the 4th day of culture. On day 6 of culture, cells were fixed and stained for TRAP and DAPI.

TRAP and DAPI staining

Adherent cells from the pre-commitment and continuous RANKL assays were fixed in a solution containing 4% formaldehyde and 0.05% Triton X-100 solution in 1X PBS for 10 min and then in a 1:1 acetone:ethanol solution for 1 min. Fixed cells were then TRAP-stained with reagents from the Acid Phosphatase, Leukocyte (TRAP) Kit (Sigma #378A). TRAP-stained wells were also stained with DAPI to visualize nuclei. Entire wells were imaged at 4X magnification using a Biotek Cytation 5 Imaging Reader (Agilent, Winooski, VT) and then the images were stitched together. Fiji Image J was used to merge color brightfield and DAPI images together and to view merged images for counting (217). Osteoclasts, defined as $TRAP^+$ cells with 3 or more nuclei, were enumerated.

Reverse transcriptase quantitative PCR (RT-qPCR)

BMDMs were cultured for 2 days in osteoclastogenic media. Cells were washed once with 1X PBS and then BMDM maintenance medium was added to the wells. Cells were then stimulated with 5% vol/vol Δ*psmα1-4* supernatant or vehicle. After 24 h of stimulation, cells were washed with 1X PBS and lysed using RT Lysis Buffer (Qiagen, Hilden, Germany) supplemented with β-mercaptoethanol. Cell lysates were obtained by centrifugation in a Qiashredder column (Qiagen) at 13000 rpm for 2 min. RNA was extracted from cell lysates using the RNeasy Mini Kit (Qiagen) in accordance with the manufacturer's instructions. RNA concentrations were measured using a Biotek Synergy HT Microplate Reader (Agilent Winooski, VT). 500 ng of RNA per sample used to synthesize cDNA using the qScript XLT cDNA Supermix (QuantaBio, Beverly, MA). cDNA was diluted 1:10 in nuclease-free water and frozen at -20°C until ready to use. RT-qPCR was performed using iQ Sybr Green Supermix (Bio-Rad, Hercules, CA) using primer sequences shown in **Table 1**. Cq values were analyzed using the ΔΔCq method (218).

Table 1. Primers for qRT-PCR experiments shown in Chapter II.

Gene	Protein Target	Fwd	Rv	Source
Actb	β-Actin	5'-GCAAGTGCTTCTAGGCGGAC-3'	5'-AAGAAAGGGTGTAAAACGCAGC-3'	(219)
Ctsk	Cathepsin-K	5'-GAAGAAGACTCACCAGAAGCAG-3'	5'-TCCAGGTTATGGGCAGAGATT-3'	(220–222) Primer Bank 31982433a1
Nfatc1	NFATc1	5'-CCCGTCACATTCTGGTCCAT-3'	5'-CAAGTAACCGTGTAGCTGCACAA-3'	(223)
Oscar	OSCAR	5'-TGGCGGTTTGCACTCTTCA-3'	5'-GATCCGTTACCAGCAGTTCCAGA-3'	(224)
Tnfrsf11a	RANK Receptor	5'-GGACGGTGTTGCAGCAGAT-3'	5'-GCAGTCTGAGTTCCAGTGGTA-3'	(221,222) Primer Bank 31981958a1

Multiplexed cytokine quantification

BMDMs from WT, *Tlr2*$^{-/-}$, *Tlr9*$^{-/-}$, and *Tlr2/9*$^{-/-}$ male mice were plated at 50,000 cells/well in 96-well plates in either BMDM maintenance media or osteoclastogenic media. After two days of culture, cells were washed in 1X PBS. Media were changed to either BMDM maintenance media or osteoclastogenic media and then cells were stimulated with 7% (vol/vol) Δ*psmα1-4* Δ*spa* supernatant so that the following culture conditions were achieved: RANKL exposure before supernatant treatment, RANKL exposure before and during supernatant treatment, RANKL exposure during supernatant treatment only, and no RANKL exposure before or during supernatant exposure. As a control, one group of WT cells in each RANKL exposure condition received vehicle treatment. After 12 h of stimulation, cell culture supernatants were collected and stored at -80°C until ready for analysis. For cytokine measurement, samples were transitioned to -20°C overnight, thawed on ice the following day, and centrifuged at 2000 x g for 10 min at 4°C to remove debris. Cytokine concentrations were measured from cell culture supernatants using the 25-plex Mouse Cytokine/Chemokine Magnetic Bead Panel (MilliporeSigma, Burlington, MA, catalog #MCYTOMAG-70K-PMX) on the FLEXMAP 3D instrument following the manufacturer's instructions. Cytokine measurements below the limit of detection for a given analyte were reported as the lowest value on the standard curve. Values above the limit of detection were reported but not used in calculations or statistical comparisons.

In vitro infection by gentamicin protection assay

BMDMs were plated at a density of 50,000 cells/well in 96-well plates in osteoclastogenic media. After two days in culture, cells were washed once with warm 1X PBS and media were replaced with antibiotic-free MEM-α + 10% FBS with CMG 14-12 supernatant at 1:20 vol/vol. Bacterial inocula were prepared from WT AH1263 and adjusted to a concentration of approximately 5 x 10^8 CFU/ml in sterile 1X PBS. Cell monolayers were infected with *S. aureus* by adding 1.25 x 10^6 CFU in 2.5 µl for a multiplicity of infection (MOI) of 25. PBS alone was added to control wells as a mock-infection. Plates were centrifuged at 1000 rpm for 1 min to bring bacteria in contact with the cell monolayers. Plates were then incubated for 2 h at 37°C to allow for bacterial internalization. Media were then removed, and cells were washed in warm 1X PBS. Cells were incubated for an additional hour with fresh MEM-α supplemented with 100 µg/ml gentamicin to kill extracellular bacteria. Following gentamicin protection, one set of samples was immediately lysed in 0.1% Triton X in 1X PBS to enumerate internalized CFU. Cell supernatants were plated from the infected wells to ensure that gentamicin effectively killed the extracellular bacteria. A separate set of infected cells was transitioned to BMDM maintenance media and incubated at 37°C and 5% CO_2 for 2 more days, after which time the infected cells were either lysed for enumeration of intracellular bacterial load or fixed and TRAP-stained. TRAP-stained wells were also stained with DAPI to visualize nuclei and were quantified in the same manner as the osteoclastogenesis assays.

Murine model of osteomyelitis

All animal experiments were approved by the Vanderbilt University Institutional Animal Care and Use Committee. Mice underwent induction of post-traumatic osteomyelitis as previously described (22,51,225). Briefly, 7- to 8-week-old mice were anesthetized using 3-3.5% isoflurane for induction and 1-1.5% for maintenance. Mice received subcutaneous injections of sustained-release buprenorphine (0.5-1 mg/kg) prior to the procedure and to maintain analgesia for 48 h post-infection. After induction of anesthesia, the left hindlimb and flank were prepared for surgery and the diaphysis of the femur was exposed using sterile technique. An approximately 1 mm defect was made in one side of the cortical bone using trephination with a 21-gauge needle. An inoculum containing either 1 x 10^5 CFU or 1 x 10^6 CFU of AH1263 in 2 µl 1X PBS was injected into the cortical defect using a micropipette. Muscle fascia and skin were then closed with sutures and the mice were allowed to recover from anesthesia. Mice were monitored and weighed daily until the experimental end point. Mice were monitored for humane endpoint criteria, which included inability to eat or drink, immobility or lethargy, hunched posture, and weight loss greater than 20% body weight occurring after 4 days post-infection. No mice in this study

met criteria for humane endpoint euthanasia. At the experimental endpoint, mice were euthanized. In the event that a femur was fractured during extraction, the sample was excluded from imaging analyses.

Murine model of septic infection

All animal experiments were approved by the Vanderbilt University Institutional Animal Care and Use Committee. Mice were anesthetized using 4% isoflurane for induction. Following anesthesia, mice were inoculated with either 5 x 10^6 or 1 x 10^7 CFU of AH1263 in a 100 µl volume via retro-orbital injection with an insulin syringe. Following injection, lubricant was immediately applied to the eye to prevent drying. Mice were placed in a pre-warmed cage to recover from anesthesia. Mice were monitored twice daily and weighed daily. Mice that displayed humane endpoint criteria including hypoactivity, hyperactivity, impaired gait, self-trauma, vocalization, restlessness, hunched posture, lack of inquisitiveness, or lesions on the eye, either immediately following the procedure or at any point post-procedure, were euthanized immediately. Mice that did not start regaining weight after 4 dpi were euthanized.

CFU enumeration

At the desired endpoint, femurs, kidneys, and livers were sterilely dissected from euthanized mice that were previously subjected to osteomyelitis or retro-orbital infection. Femurs or kidneys were singly placed in NAVY bead lysis tubes (Next Advance, Troy, NY) containing 500 µl of sterile 1X PBS. Because of the larger size, livers were split into two bead lysis tubes prior to homogenizing. Tissues were then homogenized at 4°C using a Bullet Blender at the highest setting for 3 intervals of 5 min each. Homogenates were serially diluted in sterile 1X PBS and plated on TSA plates. Plates were incubated overnight at 30°C and CFU were counted the next day. The limit of detection for this workflow is 1.69 and 1.99 Log_{10} transformed CFU for femurs/kidneys and liver, respectively.

Micro-computed tomography (µCT) of cortical and trabecular bone in femurs

Femurs were dissected from mice at day 14 post-infection, fixed in 10% neutral buffered formalin for 48 h, and then moved to 70% EtOH before storage at 4°C. Fixed femurs were scanned using a µCT50 (Scanco Medical, Switzerland) instrument and analyzed with µCT Tomography V6.3–4 software (Scanco USA, Inc.). Scans were acquired at 10.0 µm voxel size at 70 kV, 200 µA, and an integration time of 350 ms in a 10.24 mm view to result in 1088 image slices. To accommodate analysis of trabecular and cortical bone, a region of interest was selected on each femur to encompass the trabecular bone of the distal metaphysis, as well as entire the diaphysis so that the cortical defect into

which bacteria were inoculated could be visualized. The proximal epiphysis was excluded. Cortical bone destruction, callus formation, and trabecular bone volume were determined by contouring the indicated regions of interest as previously described (22,51,226). Briefly, to analyze cortical bone loss and callus formation, 818 slices were contoured, centered around the midpoint of the defect. For trabecular bone analysis, measurements to the distal trabecular bone were standardized to begin 30 slices above the growth plate. 101 slices total were analyzed.

Bone histology and histomorphometric analysis of osteoclasts in trabecular bone

After imaging by μCT, fixed femurs were decalcified for four days in 20% EDTA pH 7.4 at 4˚C, with a solution change on day 2. Decalcified femurs were processed into paraffin and embedded, then sectioned at 4μm thickness through the infectious nidus and bone marrow cavity using a Leica RM2255 microtome. Sectioned femurs were stained for TRAP with hematoxylin counterstain. Slides containing TRAP-stained histologic sections were then imaged at 10X on a Biotek Cytation 5 Image Reader (Agilent, Winooski, VT). Histomorphometry was performed on the imaged slides using BIOQUANT OSTEO software (BIOQUANT, Nashville TN). The analysis was performed on a region of interest of trabeculae proximal to the growth plate in the distal femur. Using ASBMR standards, osteoclast surface and bone perimeter were calculated and quantify percent osteoclast surface/bone surface (52).

Enzyme-linked Immunoassay (ELISA) of bone homogenates

IL-1β was measured from infected and contralateral femur samples using the IL-1β Mouse ELISA Kit (Abcam, #ab100704). Extracted femurs were placed NAVY bead lysis tubes (Next Advance, Troy, NY) containing 500 μl of sterile cell-lytic buffer supplemented with protease inhibitor. Femurs were then homogenized at 4°C using a Bullet Blender at the highest setting for 3 intervals of 5 min each. Samples were centrifuged at 4°C and 4,000 x g for 5 min to pellet bone fragments. The supernatants were moved to new Eppendorf tubes and frozen at -80°C until ready to use. To assay 100 μl of sample per well in duplicate, homogenate samples were diluted in Assay Diluent B at a 2:1 ratio. Standard curves were generated using recombinant IL-1β supplied by the kit and performing serial dilutions according to the manufacturer's instructions. Serum-free cell culture medium diluted 2:1 in Assay Diluent B was used as the diluent for the curve. The assay was carried out at described in the product manual. Absorbance was read at 450 nm using the Biotek Synergy HT Microplate Reader (Agilent Winooski, VT). IL-1β concentrations were interpolated from the sigmoidal standard curve using GraphPad Prism. To determine concentrations in the experimental samples, the interpolated values were scaled up by the dilution factor.

Statistical analysis

The plotting of data and subsequent statistical testing was done using GraphPad Prism software (Version 9). For all experiments, data were checked for normality prior to statistical analysis using either the D'Agostino-Pearson test or the Shapiro-Wilk test. In comparisons of two groups, including the comparisons of μCT data and CFU burdens in femurs and organs, a parametric t-test or a non-parametric Mann-Whiney U test was used to compare between groups, depending on normality of the data distribution. To assess the relative contributions of genotype and limb type on trabecular bone volume, a repeated measures two-way ANOVA with Sidak's test of multiple comparisons was used. To assess the effect of treatment and genotype on osteoclast counts, a two-way ANOVA was used with a post hoc Dunnett's test of multiple comparisons or Sidak's test, depending on the comparison made. To assess the effect of genotype on osteoclast count normalized to vehicle, a one-way ANOVA was used with Dunnett's test of multiple comparisons to make post hoc comparisons between genotypes. To assess the effect of genotype and RANKL-stimulation on cytokine release, a two-way ANOVA was used with Dunnett's test of multiple comparisons to compare each genotype to WT for each RANKL stimulation.

Results

S. aureus supernatants promote osteoclast differentiation in RANKL-primed precursors in a TLR2-dependent manner

To explore potential TLR-dependent effects of bacterial infection on bone homeostasis, we began by testing the effect of *S. aureus* supernatant stimulation on differentiation of RANKL-primed bone marrow-derived monocytes (BMDMs), or osteoclast precursors, *in vitro*. We used supernatants prepared from the *S. aureus* LAC (AH1263) Δ*psmα1-4* strain in these experiments (22). We chose this strain for our model because we have observed that concentrated supernatants containing the alpha-type phenol soluble modulins (PSMα) are potently cytotoxic to skeletal cells (22,51). We tested the extent to which Δ*psmα1-4* supernatant increased osteoclastogenesis in RANKL-primed precursors isolated from WT, *Tlr2*$^{-/-}$, *Tlr9*$^{-/-}$, and *Tlr2/9*$^{-/-}$ mice. We found that WT and *Tlr9*$^{-/-}$ RANKL-primed osteoclast precursors underwent significant osteoclastogenesis in response to *S. aureus* supernatant, as compared to vehicle control (**Fig. 4A-B**). Conversely, no significant differences were detected between supernatant- and vehicle-treated cells from *Tlr2*$^{-/-}$ and *Tlr2/9*$^{-/-}$ mice (**Fig. 4B**), implicating TLR2

as a major driver of osteoclastogenesis in RANKL-primed osteoclast precursors responding to Δ*psmα1-4* supernatant.

To corroborate results from osteoclast enumeration, we next measured transcripts of nuclear factor-of activated T cells cytoplasmic 1 (*Nfatc1*), a transcription factor essential for inducing osteoclast differentiation, and three genes associated with osteoclastogenesis: osteoclast-associated receptor (*Oscar*), cathepsin K (*Ctsk*), and the RANKL receptor (*Tnfrsf11a*) (89,227,228). Transcriptional changes were measured in WT and *Tlr2/9*$^{-/-}$ RANKL-primed osteoclast precursors exposed to Δ*psmα1-4* supernatant by normalizing to expression in the vehicle controls. WT cells had a greater induction of *Oscar* and *Nfatc1* upon supernatant exposure compared to *Tlr2/9*$^{-/-}$ cells. Induction of *Ctsk* and *Tnfrsf11a* did not differ between genotypes (**Fig. 4C**). Because osteoclast differentiation can be augmented by osteoclastogenic cytokines, we next measured cytokine production in RANKL-primed cells responding to Δ*psmα1-4* supernatant. Bacterial supernatants were prepared from a double knockout Δ*psmα1-4* and staphylococcal protein A (Δ*spa*) strain because protein A can bind to the Fc region of antibodies to interfere with antibody-based cytokine detection (229). Release of osteoclastogenic cytokines, including IL-6, TNF-α, MIP-1α, and IL-1α, occurred in WT and *Tlr9*$^{-/-}$ cells upon stimulation with bacterial supernatant. These responses were significantly reduced in cells lacking TLR2 (**Fig. 4D, Table 2**). Taken together, these results indicate that molecular changes consistent with osteoclastogenesis occur in RANKL-primed osteoclast precursors exposed to *S. aureus* supernatant, and these changes are blunted when TLR2 is absent.

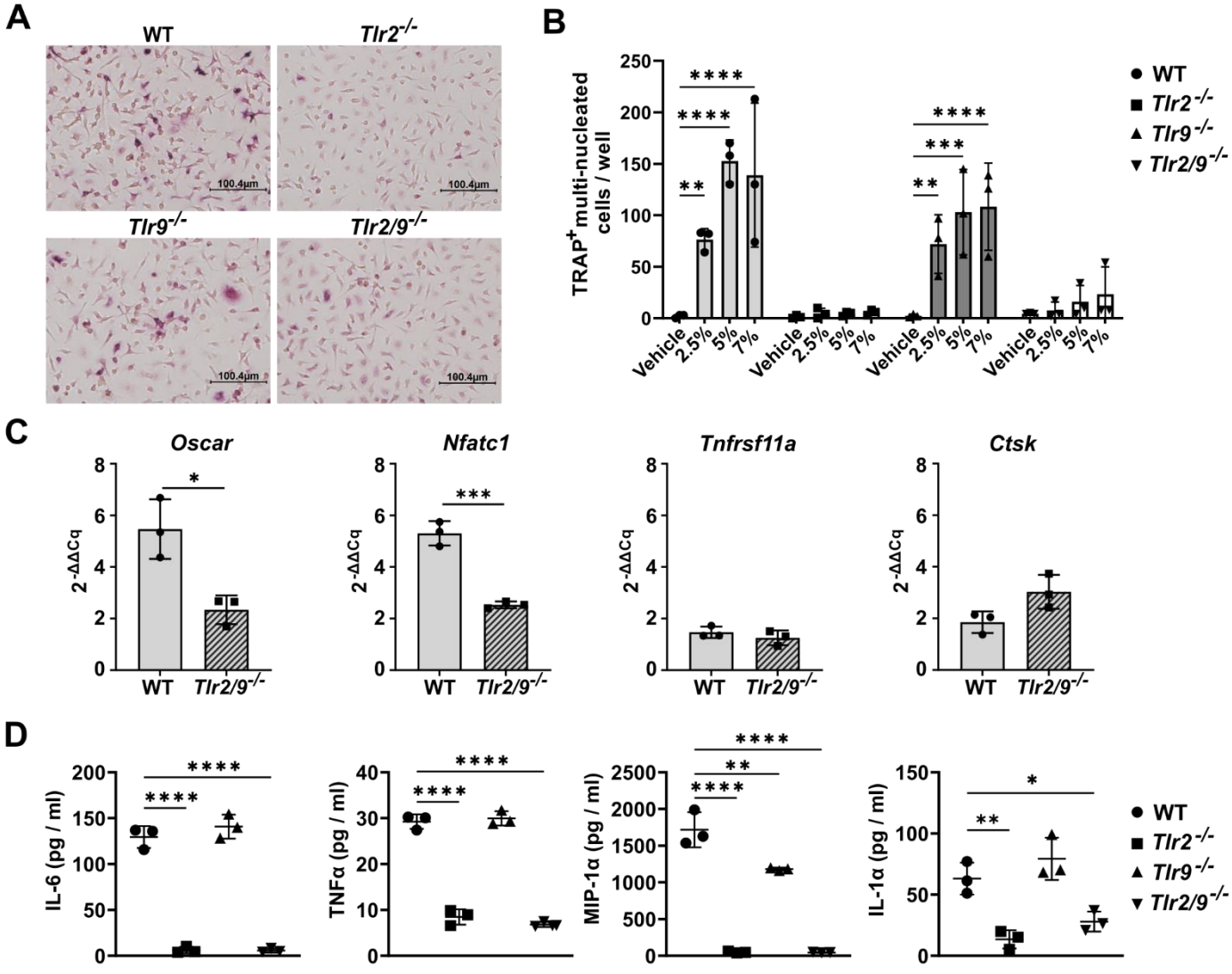
A
WT
Tlr2-/-
Tlr9-/-
Tlr2/9-/-
100.4μm
B
TRAP+multi-nucleated cells / well
Vehicle
2.5%
5%
7%
WT
Tlr2-/-
Tlr9-/-
Tlr2/9-/-
C
Oscar
Nfatc1
Tnfrsf11a
Ctsk
2-ΔΔCq
WT
Tlr2/9-/-
D
IL-6 (pg / ml)
TNFα (pg / ml)
MIP-1α (pg / ml)
IL-1α (pg / ml)

Figure 4. *S. aureus* supernatants promote osteoclastogenesis in RANKL-primed precursors through TLR2. A-B) Bone marrow-derived monocytes (BMDMs) were isolated from wildtype (WT), *Tlr2*$^{-/-}$, *Tlr9*$^{-/-}$, and *Tlr2/9*$^{-/-}$ mice and cultured with 35 ng/ml RANKL + CMG 14-12 supernatant for 2 days. RANKL-primed osteoclast precursors were stimulated with the indicated vol/vol percentage of supernatant from the Δ*psmα1-4* strain of *S. aureus* or vehicle control in media containing CMG 14-12 supernatant but lacking RANKL. After 4 more days of culture, cells were stained for tartrate-resistant acid phosphatase (TRAP) and TRAP^{+}, multinucleated (≥3 nuclei) osteoclasts were quantified. **A)** Representative images of the 5% treatment condition were obtained at 20X magnification. **B)** Enumeration of TRAP^{+} multinucleated osteoclasts. Osteoclast counts were evaluated by two-way ANOVA and counts from each genotype were compared to vehicle by Dunnett's multiple comparisons test. **p < 0.01, ***p < 0.001, ****p < 0.0001. If not denoted with asterisks, statistical difference between treatments was not significant. Error bars denote standard deviation (SD). Results are representative of three biological replicate experiments and n = 3 technical replicates from one biological replicate are plotted. **C)** BMDMs were primed with 35 ng/ml RANKL and CMG 14-12 supernatant for 2 days, then stimulated with 7.5% supernatant from Δ*psmα1-4* or vehicle for 24 h in media without RANKL. Cell lysates were collected, and transcript levels were measured by RT-qPCR. ΔΔCq values were compared between genotypes by t-test. *p < 0.05, ***p < 0.001. If not denoted with asterisks, statistical difference between genotypes was not significant. Error bars denote SD. Results are representative of two biological replicates with n = 3 technical replicates per group plotted. **D)** BMDMs were cultured in 35 ng/ml RANKL + CMG 14-12 supernatant for 2 days. RANKL-primed osteoclast precursors were stimulated with 7% Δ*psmα1-4* Δ*spa* supernatant in the absence of RANKL. Cell culture supernatants were collected after 12 h of stimulation. Cytokine abundance was measured using Luminex technology. Cytokines were compared across genotypes by one-way ANOVA and Dunnett's multiple comparison's test was used to compare between WT and knockout. *p < 0.05, **p < 0.01, ****p < 0.0001. If not denoted with asterisks, statistical difference between genotypes was not significant. Error bars denote SD. Results represent one biological replicate with n = 3 technical replicates per group.

Table 2. Cytokine responses upon RANKL withdrawal. BMDMs were cultured in media containing 35 ng/ml RANKL + CMG 14-12 supernatant for 2 days. Cells were then changed to RANKL-free media and stimulated with 7% vol/vol of supernatant from the Δ*psmα1-4* Δ*spa* strain. Cytokines were measured after 12 h of stimulation. Average cytokine abundance in pg/ml is shown ± SD.

*Under LOD measurement used in mean and SD calculation or only measured value reported

#One or more measurements omitted from mean and SD calculation because the coefficient of variation for duplicate samples was greater than 30% or because the measured value exceeded the detection maximum

Table 2: RANKL → No RANKL					
Cytokine	**WT vehicle**	**WT Δ*psmα1-4* Δ*spa***	***Tlr2*$^{-/-}$ Δ*psmα1-4* Δ*spa***	***Tlr9*$^{-/-}$ Δ*psmα1-4* Δ*spa***	***Tlr2/9*$^{-/-}$ Δ*psmα1-4* Δ*spa***
G-CSF	3.24 ± 0.29	2235.67 ± 258.11	8.85 ± 6.74	3059.67 ± 150.07	3.06 ± 0.47
GM-CSF	30.21 ± 1.76	29.58 ± 5.60	24.17 ± 7.50	31.93 ± 3.19	26.05 ± 1.84
INFγ	2.27 ± 0.27	3.29 ± 0.32	1.86 ± 0.75	4.36 ± 0.75	1.65 ± 0.10
IL-1α	28.57 ± 2.78	63.17 ± 13.08	13.46 ± 7.48	79.29 ± 17.29	27.97 ± 8.19
IL-1β	2.60 ± 0.84	2.46 ± 0.58	1.81 ± 0.66	3.57 ± 0.52	*1.75 ± 0.75
IL-2	11.86 ± 0.47	9.37 ± 0.35	9.22 ± 1.43	12.12 ± 5.38	9.74 ± 2.37
IL-4	#0.75 ± 0.19	*0.70 ± 0.16	0.63 ± 0.12	0.79 ± 0.23	*0.55 ± .01
IL-5	7.03 ± 1.99	11.66 ± 2.13	5.94 ± 1.50	#13.50 ± 0.27	6.15 ± 1.86
IL-6	5.10 ± 1.31	129.47 ± 11.96	6.31 ± 3.50	140.89 ± 13.06	5.68 ± 2.15
IL-7	2.27 ± 0.65	2.16 ± 0.54	1.85 ± 0.46	2.76 ± 1.11	1.88 ± 0.55
IL-9	67.59 ± 5.83	69.10 ± 7.39	41.74 ± 11.86	72.54 ± 18.84	48.36 ± 10.83
IL-10	3.90 ± 0.91	221.52 ± 30.61	4.27 ± 1.35	213.15 ± 3.82	4.38 ± 0.36
IL-12 (p40)	2.11 ± 0.80	2.64 ± 0.45	1.83 ± 0.95	4.49 ± 1.23	2.09 ± 0.54
IL-12 (p70)	13.73 ± 2.92	11.52 ± 3.36	8.74 ± 1.27	14.70 ± 4.21	8.37 ± 3.97
IL-13	2.56 ± 0.16	3.70 ± 0.54	1.16 ± 0.14	3.65 ± 0.75	1.62 ± 0.72
IL-15	14.71 ± 3.41	19.96 ± 5.68	13.02 ± 5.11	21.72 ± 7.95	14.70 ± 1.86
IL-17	0.77 ± 0.11	15.63 ± 0.89	*0.60 ± 0.14	13.30 ± 0.50	*0.64 ± 0.21
IP-10	251.70 ± 49.17	428.80 ± 86.71	115.70 ± 10.57	345.77 ± 78.95	188.17 ± 32.92
KC	29.39 ± 1.50	1345.33 ± 208.46	50.10 ± 14.27	1397.33 ± 240.35	31.39 ± 2.11
MCP-1	194.88 ± 23.34	1257.00 ± 143.95	217.59 ± 18.15	1063.87 ± 122.33	319.46 ± 9.10
MIP-1α	32.39 ± 1.73	1718.00 ± 239.06	50.79 ± 11.99	1181.67 ± 19.22	44.94 ± 4.76
MIP-1β	51.12 ± 4.46	8136.67 ± 1852.34	88.19 ± 10.37	5285.00 ± 52.46	78.43 ± 5.50
MIP-2	92.75 ± 8.76	13168.00 ± 1174.41	636.84 ± 44.73	#13164.00	324.89 ± 47.91
RANTES	3.96 ± 0.54	13.32 ± 1.42	2.76 ± 0.60	13.12 ± 0.55	3.39 ± 0.41
TNFα	5.06 ± 0.81	27.59 ± 1.80	6.38 ± 1.38	28.40 ± 1.81	5.04 ± 0.43

TLR2 promotes osteoclastogenesis during dual stimulation with *S. aureus* supernatant and RANKL

The fate of an osteoclast precursor is influenced by agonism of TLR2 and 9, especially before or shortly after RANKL exposure (127). However, in the bone microenvironment, exposure to RANKL and bacterial ligands may occur either sequentially or simultaneously. Thus, we questioned whether the ability of TLR2 to promote osteoclastogenesis would be altered when RANKL stimulation continued during *S. aureus* supernatant exposure. We measured osteoclast formation in WT, *Tlr2*$^{-/-}$, *Tlr9*$^{-/-}$, and *Tlr2/9*$^{-/-}$ BMDMs primed with RANKL for one day followed by dual RANKL and Δ*psmα1-4* supernatant stimulation. We found that osteoclast abundance increased in response to a range of supernatant doses in WT, *Tlr2*$^{-/-}$, and *Tlr9*$^{-/-}$ cells. However, *Tlr2/9*$^{-/-}$ cells incurred increased osteoclast formation only with select supernatant concentrations (**Fig. 5A-B**). To better visualize the increase in osteoclast formation incited by supernatant treatment and to control for stochastic differences in baseline osteoclast number, the data were also analyzed after normalization of osteoclast counts to the vehicle control for each genotype. This analysis revealed that loss of TLR2, but not TLR9, limits the increase in osteoclast differentiation, as *Tlr2*$^{-/-}$ and *Tlr2/9*$^{-/-}$ cells had significantly less induction of osteoclast formation than WT cells following treatment with 5%, 7%, or 9% supernatant (**Fig. 5C**). These results suggest that TLR2 promotes increased osteoclastogenesis when RANKL and bacterial stimulation are applied concurrently. Because some increases in osteoclastogenesis occurred in *Tlr2*$^{-/-}$ cells, there are likely TLR2-independent mechanisms responsible for a proportion of the osteoclast formation occurring in response to concurrent RANKL and bacterial stimulation.

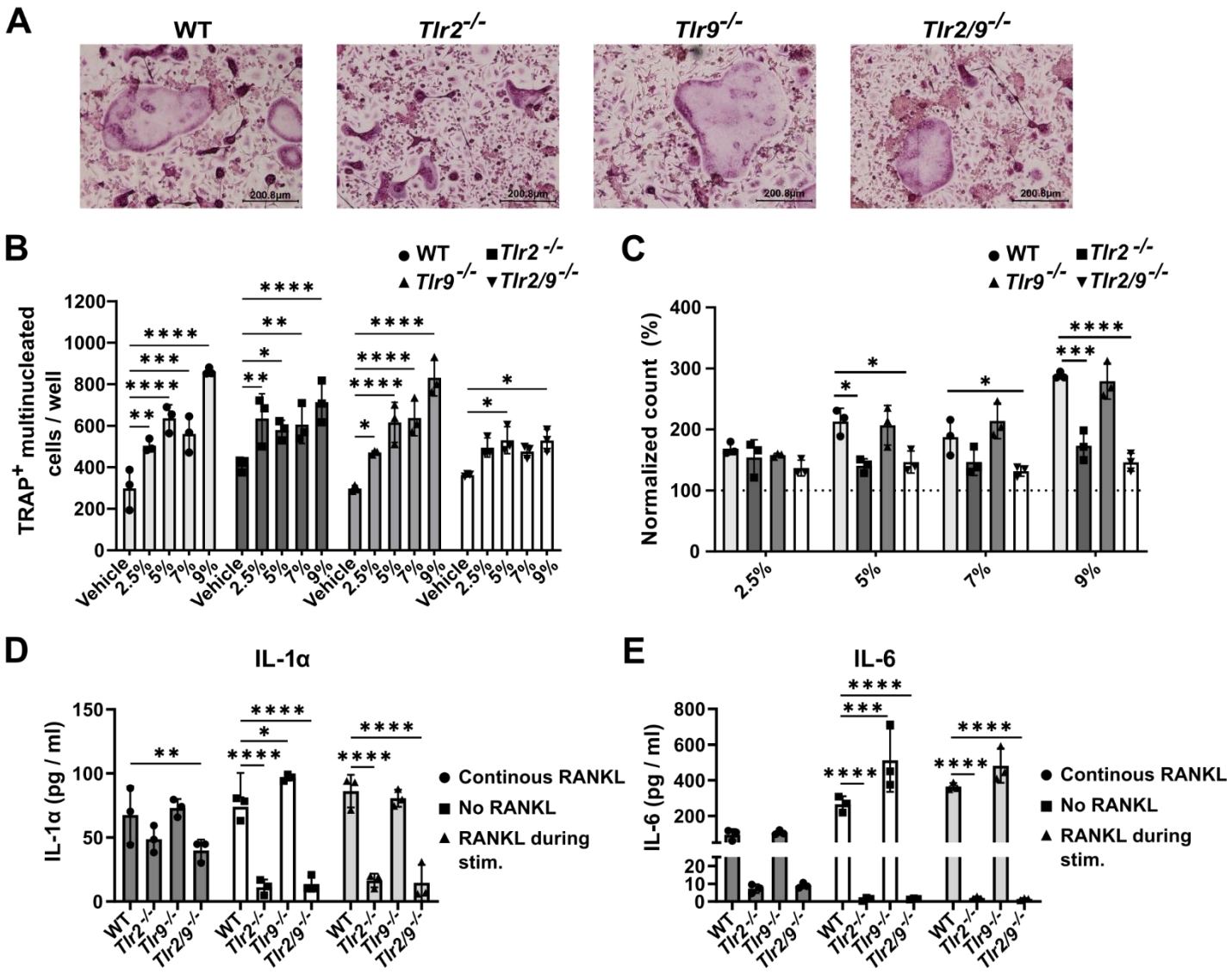
A
WT
Tlr2-/-
Tlr9-/-
Tlr2/9-/-
200.8µm
B
WT
Tlr2 -/-
Tlr9 -/-
Tlr2/9 -/-
TRAP+ multinucleated cells / well
Vehicle
2.5%
5%
7%
9%
C
Normalized count (%)
D
IL-1α
IL-1α (pg / ml)
Continous RANKL
No RANKL
RANKL during stim.
E
IL-6
IL-6 (pg / ml)

Figure 5. The timing of RANKL exposure alters the relative impact of TLR2 on bacterial-induced osteoclastogenesis and cytokine responses. A-C) BMDMs from WT, *Tlr2*$^{-/-}$, *Tlr9*$^{-/-}$, and *Tlr2/9*$^{-/-}$ mice were plated in CMG 14-12 supernatant + 35 ng/ml RANKL. After one day of culture, RANKL and CMG 14-12 supernatant stimulation were maintained, and cells were exposed to the indicated vol/vol percentage of *S. aureus* supernatant from the Δ*psmα1-4* strain or vehicle control. After 4 more days of culture, cells were fixed, stained for TRAP, and TRAP^{+}, multinucleated osteoclasts were quantified. **A)** Representative images of the 5% treatment condition were taken at 10X magnification. **B)** Counts of TRAP^{+}, multinucleated cells were analyzed by two-way ANOVA and Dunnett's multiple comparisons test was used to compare between treatment and vehicle for each genotype. *p < 0.05, **p < 0.01, ***p < 0.0001, ****p < 0.0001. If not denoted with asterisks, statistical difference between treatments was not significant. Error bars denote SD. Results are representative of three biological replicates and n = 3 technical replicates from one biological replicate are plotted per group. **C)** Changes in osteoclast number were calculated relative to the average vehicle count for the respective genotype. For each treatment, a one-way ANOVA was used to assess the effect of genotype and Dunnett's test of multiple comparisons was used to compare each genotype to WT within each supernatant concentration. *p < 0.05, **p < 0.01, ***p < 0.001, ****p < 0.0001. If not denoted with asterisks, statistical difference between genotypes was not significant. Error bars denote SD. Results are representative of three biological replicates and n = 3 technical replicates from one biological replicate are plotted per group. **D-E)** BMDMs were seeded in media with or without RANKL. After 2 days of culture, cells incubated in media without RANKL were treated with 7% vol/vol Δ*psmα1-4* Δ*spa* supernatant ("No RANKL") or RANKL + 7% vol/vol Δ*psmα1-4* supernatant ("RANKL during stim. only"). Cells incubated in media with RANKL were treated with 7% Δ*psmα1-4* Δ*spa* supernatant with RANKL maintained ("continuous RANKL"). After an additional 12 h incubation, cytokines were measured from cell culture media using Luminex technology. Cytokine concentrations were evaluated by two-way ANOVA and Dunnett's test of multiple comparisons was used to compare each genotype to WT. *p < 0.05, **p < 0.01, ***p < 0.001, ****p < 0.0001. If not denoted with asterisks, statistical difference between genotypes was not significant. Error bars denote SD. Results represent one biological replicate with n = 3 technical replicates per group.

TLR2-dependent cytokine responses to bacterial supernatants are affected by timing of RANKL exposure

To better understand the TLR2-dependent signaling events that lead to enhancement of osteoclastogenesis in the presence of RANKL, we measured cytokine responses in WT, *Tlr2*$^{-/-}$, *Tlr9*$^{-/-}$, and *Tlr2/9*$^{-/-}$ BMDMs exposed to three different sequences of RANKL and Δ*psmα1-4* Δ*spa* supernatant: 1) RANKL followed by Δ*psmα1-4* Δ*spa* supernatant with continued RANKL, 2) No RANKL followed by Δ*psmα1-4* Δ*spa* supernatant, or 3) No RANKL followed by RANKL and Δ*psmα1-4* Δ*spa* supernatant. We found that the presence of TLR2 was a strong determinant of cytokine response, irrespective of RANKL exposure (**Tables 3-5**). However, magnitude of cytokine release was reduced by continuous RANKL exposure for most cytokines measured (**Table 4**). Release of the osteoclastogenic cytokines IL-6 and IL-1α was significantly affected by both cell genotype and RANKL exposure when evaluated by two-way ANOVA. Moreover, both IL-6 and IL-1α were reduced in *Tlr2*$^{-/-}$ and *Tlr2/9*$^{-/-}$ cells compared to WT when cells were either not exposed to RANKL or simultaneously exposed to RANKL and supernatant, but not when RANKL exposure was continuous (**Fig. 5D-E**). These data indicate that cytokine elaboration in response to *S. aureus* supernatants is influenced by prior RANKL exposure and occurs in a TLR2-dependent manner.

Table 3. Cytokine response in macrophages. BMDMs were cultured in media containing CMG 14-12 supernatant for 2 days. Cells were then stimulated with 7% vol/vol of supernatant from the Δ*psmα1-4* Δ*spa* strain. Cytokines were measured after 12 h of stimulation. Average cytokine abundance in pg/ml is shown ± SD.

*Under LOD measurement used in mean and SD calculation or only measured value reported

#One or more measurements omitted from mean and SD calculation because the coefficient of variation for duplicate samples was greater than 30% or because the measured value exceeded the detection maximum

<X All measurements were under detection minimum

>X All measurements were over detection maximum

Table 3: No RANKL → No RANKL					
Cytokine	**WT vehicle**	**WT Δ*psmα1-4* Δ*spa***	***Tlr2*$^{-/-}$ Δ*psmα1-4* Δ*spa***	***Tlr9*$^{-/-}$ Δ*psmα1-4* Δ*spa***	***Tlr2/9*$^{-/-}$ Δ*psmα1-4* Δ*spa***
G-CSF	*0.89 ± 0.30	2951.67 ± 284.82	*1.05 ± 0.41	3657.67 ± 515.04	0.93 ± 0.15
GM-CSF	12.70 ± 3.80	*13.38 ± 8.20	*7.56 ± 3.33	25.38 ± 5.67	11.45 ± 1.01
INFγ	*0.83 ± 0.34	2.18 ± 0.52	*0.76 ± 0.23	3.39 ± 0.61	*0.63 ± 0.16
IL-1α	11.31 ± 4.94	74.09 ± 9.49	*11.14± 6.01	96.79 ± 2.53	13.74 ± 6.08
IL-1β	*1.197 ± 0.51	2.16 ± 0.93	<0.90	3.58 ± 2.24	<0.90
IL-2	3.83 ± 0.80	4.85 ± 1.34	#7.93 ± 1.05	9.03 ± 2.55	5.81 ± 1.71
IL-4	<0.55	<0.55	<0.55	<0.55	<0.55
IL-5	2.02 ± 0.83	3.49 ± 1.13	1.37 ± 0.32	4.54 ± 0.68	2.01 ± 0.13
IL-6	0.85 ±	265.87 ± 44.93	1.32± 0.92	512.12 ± 177.25	1.46 ± 0.37
IL-7	<0.77	<0.77	<0.77	1.28 ± 0.12	*0.78 ± 0.02
IL-9	15.15 ± 6.29	59.97 ± 9.00	19.78 ± 12.84	72.12 ± 7.96	15.17 ± 3.20
IL-10	1.61 ± 0.12	304.30 ± 30.61	*1.73 ± 0.88	313.69 ± 19.98	1.41 ± 0.42
IL-12 (p40)	*1.73 ± 1.26	*2.22 ± 1.56	*1.14	3.07 ± 0.26	2.44 ± 0.65
IL-12 (p70)	*1.86 ± 0.88	*3.50 ± 2.39	4.02 ± 0.55	6.30 ± 2.46	3.64 ± 0.77
IL-13	2.93 ± 0.89	4.36 ± 0.95	#1.48 ± 0.10	7.16 ± 1.46	2.10 ± 0.96
IL-15	*4.02 ± 3.66	*3.41 ± 1.59	3.26 ± 1.97	8.28 ± 3.32	3.36 ± 2.33
IL-17	2.74 ± 0.67	26.00 ± 1.80	#1.83 ± 0.64	28.04 ± 1.92	1.41 ± 0.13
IP-10	632.80 ± 170.51	483.16 ± 122.59	#273.16 ± 21.58	757.18 ± 162.12	477.56 ± 253.45
KC	67.46 ± 16.55	3020.67 ± 578.69	87.73 ± 17.13	4079.00 ± 465.54	66.83 ± 13.38
MCP-1	721.07 ± 30.04	2511.00 ± 398.65	#620.58 ± 17.79	4016.00 ± 1535.26	878.09 ± 71.08
MIP-1α	226.94 ± 18.88	#9878.00	#200.56 ± 1.41	>15053	168.96 ± 13.96
MIP-1β	728.12 ± 85.37	>9967	#611.94 ± 26.57	>9967	463.52 ± 36.68
MIP-2	462.50 ± 72.45	>14319	1993.67 ± 295.11	>14319	1142.00 ±108.57
RANTES	4.47 ± 1.24	56.32 ± 7.26	2.81 ± 1.44	66.56 ± 10.24	4.12 ± 1.09
TNFα	5.68 ± 0.92	101.80 ± 12.72	7.34 ± 1.61	32.12 ± 21.75	5.34 ± 0.46

Table 4. Cytokine response in continuous RANKL. BMDMs were cultured in media containing 35 ng/ml RANKL + CMG 14-12 supernatant for 2 days. RANKL was continued and cells were stimulated with 7% vol/vol of supernatant from the Δ*psmα1-4* Δ*spa* strain Cytokines were measured after 12 h of stimulation. Average cytokine abundance in pg/ml is shown ± SD.

*Under LOD measurement used in mean and SD calculation or only measured value reported

#One measurement omitted from mean and SD calculation because the coefficient of variation for duplicate samples was greater than 30%

Table 4: RANKL → RANKL					
Cytokine	**WT vehicle**	**WT Δ*psmα1-4* Δ*spa***	***Tlr2*$^{-/-}$ Δ*psmα1-4* Δ*spa***	***Tlr9*$^{-/-}$ Δ*psmα1-4* Δ*spa***	***Tlr2/9*$^{-/-}$ Δ*psmα1-4* Δ*spa***
G-CSF	#2.62 ± 0.00	1556.00 ± 448.64	3.73 ± 0.82	1771.00 ± 251.81	4.92 ± 1.20
GM-CSF	29.17 ± 8.09	*22.27 ± 16.62	32.70 ± 1.47	28.34 ± 4.49	29.45 ± 1.93
INFγ	1.67 ± 0.25	2.23 ± 0.88	2.61 ± 0.39	2.74 ± 0.18	2.31 ± 0.39
IL-1α	29.51 ± 15.56	67.61 ± 22.26	48.67 ± 10.47	73.12 ± 6.90	39.94 ± 8.50
IL-1β	1.83 ± 1.13	*2.30 ± 1.28	2.59 ± 0.28	3.43 ± 0.66	1.97 ± 0.59
IL-2	9.70 ± 0.68	14.22 ± 1.11	18.49 ± 2.98	14.09 ± 2.63	15.77 ± 3.80
IL-4	*0.60 ± 0.09	*0.71 ± 0.09	0.86 ± 0.13	0.66 ± 0.00	0.63 ± 0.04
IL-5	6.44 ± 2.08	8.25 ± 1.60	7.32 ± 1.73	7.11 ± 1.09	6.97 ± 1.35
IL-6	#4.86 ± 0.47	94.94 ± 30.76	7.23 ± 2.43	106.23 ± 12.77	8.94 ± 1.47
IL-7	2.34 ± 1.55	*1.58 ± 0.74	2.76 ± 0.54	2.37 ± 0.13	2.44 ± 0.35
IL-9	55.79 ± 8.09	66.22 ± 10.71	79.82 ± 7.57	77.21 ± 6.63	73.25 ± 10.50
IL-10	4.69 ± 1.65	253.46 ± 44.59	11.26 ± 0.76	249.53 ± 11.41	9.29 ± 2.01
IL-12 (p40)	*2.12 ± 1.25	*1.90 ± 1.04	3.61 ± 0.70	3.57 ± 0.29	2.19 ± 0.45
IL-12 (p70)	#12.21 ± 0.59	10.83 ± 3.99	14.84 ± 0.96	15.94 ± 2.48	16.22 ± 3.13
IL-13	3.08 ± 0.46	3.10 ± 1.48	2.17 ± 0.67	3.36 ± 0.71	2.09 ± 0.31
IL-15	14.62 ± 11.88	*13.39 ± 10.18	19.18 ± 4.09	21.32 ± 1.22	23.27 ± 6.51
IL-17	*0.65 ± 0.13	12.23 ± 2.68	0.77 ± 0.13	9.39 ± 1.06	0.81 ± 0.07
IP-10	455.73 ± 110.01	425.95 ± 250.95	188.92 ± 67.60	329.83 ± 89.40	205.14 ± 54.59
KC	#38.86 ± 1.08	984.60 ± 239.27	52.59 ± 2.14	1051.55 ± 119.45	45.36 ± 4.29
MCP-1	174.03 ± 27.57	932.05 ± 255.42	161.24 ± 5.99	776.28 ± 42.69	247.82 ± 6.68
MIP-1α	30.15 ± 3.95	925.49 ± 188.22	38.05 ± 3.92	650.46 ± 35.97	37.42 ± 0.23
MIP-1β	45.99 ± 8.48	3931.33 ± 1472.54	65.75 ± 4.46	2186.00 ± 259.28	65.24 ± 1.70
MIP-2	91.93 ± 25.85	10484.67 ± 2100.01	746.96 ± 30.80	13295.33 ± 1008.15	503.89 ± 46.82
RANTES	4.17 ± 0.48	11.17 ± 2.96	4.03 ± 0.28	11.34 ± 1.35	4.36 ± 0.08
TNFα	6.95 ± 0.91	25.08 ± 4.52	9.67 ± 1.16	27.46 ± 1.00	9.34 ± 0.35

Table 5. Cytokine response during dual RANKL and supernatant exposure. Cytokine response in BMDMs were cultured in media with CMG 14-12 supernatant for 2 days. Cells were then moved to media containing 35 ng/ml RANKL + CMG 14-12 supernatant and stimulated with 7% vol/vol of supernatant from the Δ*psmα1-4* Δ*spa* strain. Cytokines were measured after 12 h of stimulation. Average cytokine abundance in pg/ml is shown ± SD.

*Under LOD measurement used in mean and SD calculation or only measured value reported

#One or more measurements omitted from mean and SD calculation because the coefficient of variation for duplicate samples was greater than 30% or because the measured value exceeded the detection maximum

>X All measurements were over detection maximum

Table 5: No RANKL → RANKL					
Cytokine	**WT vehicle**	**WT Δ*psmα1-4* Δ*spa***	***Tlr2*$^{-/-}$ Δ*psmα1-4* Δ*spa***	***Tlr9*$^{-/-}$ Δ*psmα1-4* Δ*spa***	***Tlr2/9*$^{-/-}$ Δ*psmα1-4* Δ*spa***
G-CSF	*0.86 ± 0.32	2786.00 ± 176.60	*1.10 ± 0.45	2507.33 ± 156.30	*0.99 ± 0.37
GM-CSF	13.42 ± 1.67	21.33 ± 2.46	8.32 ± 2.14	23.02 ± 2.96	*8.26 ± 3.77
INFγ	*0.68 ± 0.08	3.58 ± 1.02	0.86 ± 0.20	3.42 ± 1.18	*0.80 ± 0.28
IL-1α	12.68 ± 2.95	86.24 ± 12.75	16.46 ± 5.41	80.67 ± 6.67	14.64 ± 14.07
IL-1β	*1.11 ± 0.37	4.99 ± 0.35	*1.11 ± 0.37	4.22 ± 1.40	<0.90
IL-2	5.21 ± 1.19	10.30 ± 1.30	6.59 ± 2.86	6.86 ± 1.97	5.11 ± 3.39
IL-4	<0.55	<0.55	<0.55	<0.55	<0.55
IL-5	1.44 ± 0.42	3.64 ± 0.45	1.72 ± 0.24	3.04 ± 0.52	1.37 ± 0.12
IL-6	1.17 ± 0.58	364.28 ± 20.56	2.06 ± 0.74	481.89 ± 96.28	1.45 ± 0.58
IL-7	*0.88 ± 0.19	*0.84 ± 0.09	*0.83 ± 0.10	*0.86 ± 0.15	*0.88 ± 0.19
IL-9	17.10 ± 7.63	74.87 ± 5.26	18.73 ± 6.33	64.50 ± 5.38	17.16 ± 5.01
IL-10	2.90 ± 0.31	342.56 ± 40.25	3.24 ± 0.51	302.45 ± 13.55	1.94 ± 0.24
IL-12 (p40)	2.51 ± 0.75	4.24 ± 0.76	*1.01 ± 0.25	4.97 ± 0.68	1.79 ± 1.27
IL-12 (p70)	1.69 ± 0.40	#8.90 ± 4.09	*2.21 ± 0.86	4.54 ± 0.60	*2.41 ± 1.11
IL-13	4.70 ± 0.48	5.32 ± 0.62	1.58 ± 0.15	7.08 ± 1.81	1.92 ± 0.48
IL-15	*4.02 ± 3.66	8.48 ± 3.66	*3.22 ± 2.45	7.39 ± 4.17	*2.91 ± 1.38
IL-17	1.42 ± 0.10	27.74 ± 1.73	1.50 ± 0.45	26.85 ± 1.16	0.87 ± 0.17
IP-10	1477.00 ± 423.47	647.46 ± 92.92	300.88 ± 20.84	816.43 ± 195.73	398.81 ±76.14
KC	109.90 ± 21.33	3742.67 ± 468.76	90.86 ± 25.27	3921.67 ± 290.82	59.02 ± 13.01
MCP-1	733.01 ± 72.76	2742.33 ± 377.35	526.79 ± 31.64	3080.33 ± 276.73	752.70 ± 37.47
MIP-1α	167.32 ± 15.79	#14596	164.44 ± 31.64	#11801.50 ± 594.68	136.90 ± 7.27
MIP-1β	461.63 ± 46.86	>9967	441.94 ± 14.42	>9967	335.25 ± 29.34
MIP-2	637.85 ± 46.31	>14319	2116.33 ± 704.98	>14319	1144.40 ± 181.17
RANTES	6.21 ± 1.69	80.11 ± 9.63	3.38 ± 0.78	84.47 ±0.59	3.65 ± 1.25
TNFα	5.03 ± 0.69	127.58 ± 12.27	6.35 ± 2.39	122.10 ± 3.70	4.55 ± 0.95

Loss of TLR2 does not affect bacterial burdens during *S. aureus* osteomyelitis

Because TLR2 has been shown to promote the host response to *S. aureus*, we hypothesized that loss of TLR2 would alter the pathogenesis of osteomyelitis (142,144,199). We first tested whether loss of TLR2 would compromise host containment of *S. aureus* during osteomyelitis. At 14 days post-infection (dpi), no significant differences in colony forming units (CFU) were detected in infected femurs from *Tlr2*$^{-/-}$ mice compared to WT. To determine whether loss of TLR2 enhances dissemination from the inoculation site in the femur, we also measured bacterial burdens in the liver and kidneys. There were no significant differences in burdens between genotypes (**Fig. 6A)**. It has been reported that TLR2 signaling plays a role in host bacterial burden control at early timepoints during *S. aureus* skin infection (108,110). To address the possibility that loss of TLR2 causes deficits in bacterial burden control early during osteomyelitis, we performed a time course using a reduced inoculum, to increase resolution on small differences in bacterial load. At 1 dpi there was a significant increase in femur CFU in WT mice compared to *Tlr2*$^{-/-}$, but this difference was not detected at 2 or 5 dpi (**Fig. 6B**). To better characterize the role of TLR2 in host bacterial control in post-traumatic osteomyelitis, we also tested whether *S. aureus* lacking mature lipoproteins due to inactivation of the lipoprotein diacylglycerol transferase (*lgt*) gene would induce infection of altered severity. Prior work suggests that this strain may evade host detection due its lack of TLR2-ligating lipoproteins (147). WT and *Tlr2*$^{-/-}$ mice were infected with the *lgt*::Tn strain, and a set of WT mice was also infected with WT *S. aureus* as a control. In this study, both WT and *Tlr2*$^{-/-}$ mice infected with the *lgt*::Tn strain incurred lower femur bacterial burdens than WT mice infected with the WT strain (**Fig. 7**). Because several previous studies have found TLR2 essential to host survival during septic infection, we also induced sepsis via retro-orbital injections of WT *S. aureus* in WT and *Tlr2*$^{-/-}$ mice. We did not detect any significant differences in weight loss, survival, or bacterial burdens in *Tlr2*$^{-/-}$ mice compared to WT mice (**Fig. 8A-C**). In sum, these results indicate that TLR2 is not a major contributor to the control of bacterial burdens in this model of *S. aureus* osteomyelitis.

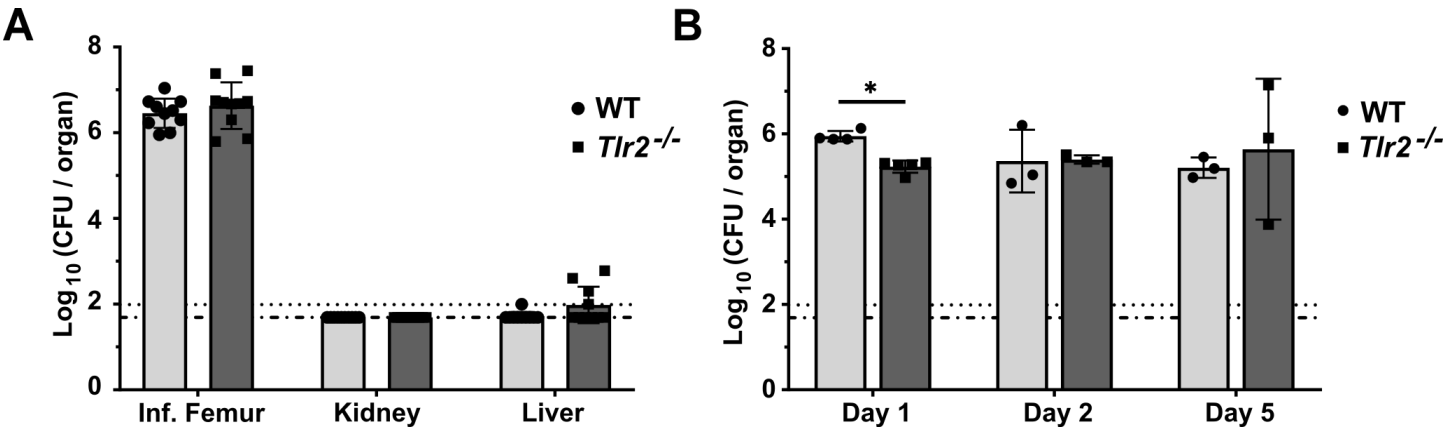

Figure 6. TLR-deficiency does not alter bacterial burden control in *S. aureus* osteomyelitis. A) WT or *Tlr2*$^{-/-}$ female, 8-week-old mice were subjected to osteomyelitis by intraosseous injection of 10^6 CFU of *S. aureus*. Kidneys, livers, and infected femurs were collected at 14 days post-infection (dpi). Femurs, kidneys, and livers were extracted and homogenized for CFU enumeration. Dotted lines indicate the Log_{10} transformed limits of detection. Log_{10} transformed CFUs/femur values were compared between genotypes by unpaired t-test. Data were pooled from two independent experiments, n = 10 mice per genotype. Error is plotted as SD. **B)** WT or *Tlr2*$^{-/-}$ female, 8-week-old mice were subjected to osteomyelitis by intraosseous injection of 10^5 CFU of *S. aureus*. Infected femurs were collected at day 1 (WT n = 4, *Tlr2*$^{-/-}$ n = 5), day 2 (WT n = 3, *Tlr2*$^{-/-}$ n = 3), or day 5 (WT n = 3, *Tlr2*$^{-/-}$ n = 3). CFU burdens were compared between genotypes by Mann-Whitney test, *p < 0.05. If not denoted with asterisks, statistical difference between genotypes was not significant.

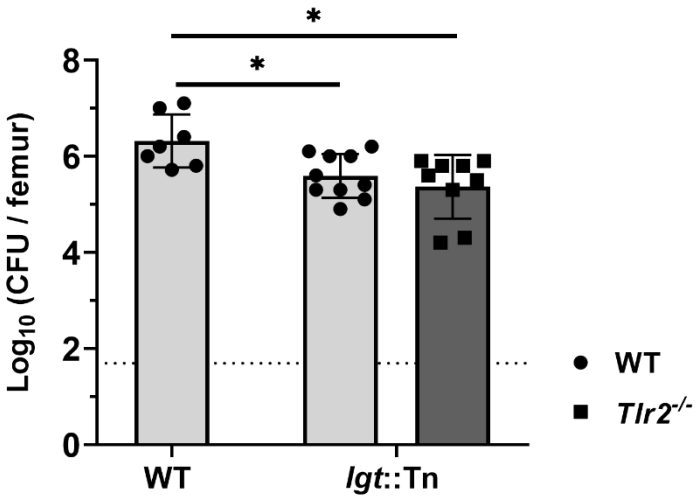

Figure 7. Deficiency in *S. aureus* lipoprotein maturation lowers bacterial burdens during osteomyelitis. WT or *Tlr2*$^{-/-}$ female, 8-week-old mice were subjected to osteomyelitis by intraosseous injection of 10^6 CFU of the WT *S. aureus* strain (WT mice only) or *lgt*::Tn strain of *S. aureus*. At 14 dpi, mice were euthanized, and femurs were collected for CFU enumeration. Log_{10} transformed CFU/femur values were compared using a Brown-Forsythe and Welch ANOVA with Dunnett's T3 multiple comparisons test, *p < 0.05. Results are pooled from two independent experiments. For *lgt*::Tn, n = 10 WT mice and n = 9 *Tlr2*$^{-/-}$ mice. For infections with WT *S. aureus*, n = 7 WT mice. Error is plotted as SD. The dotted line indicates the lower limit of detection.

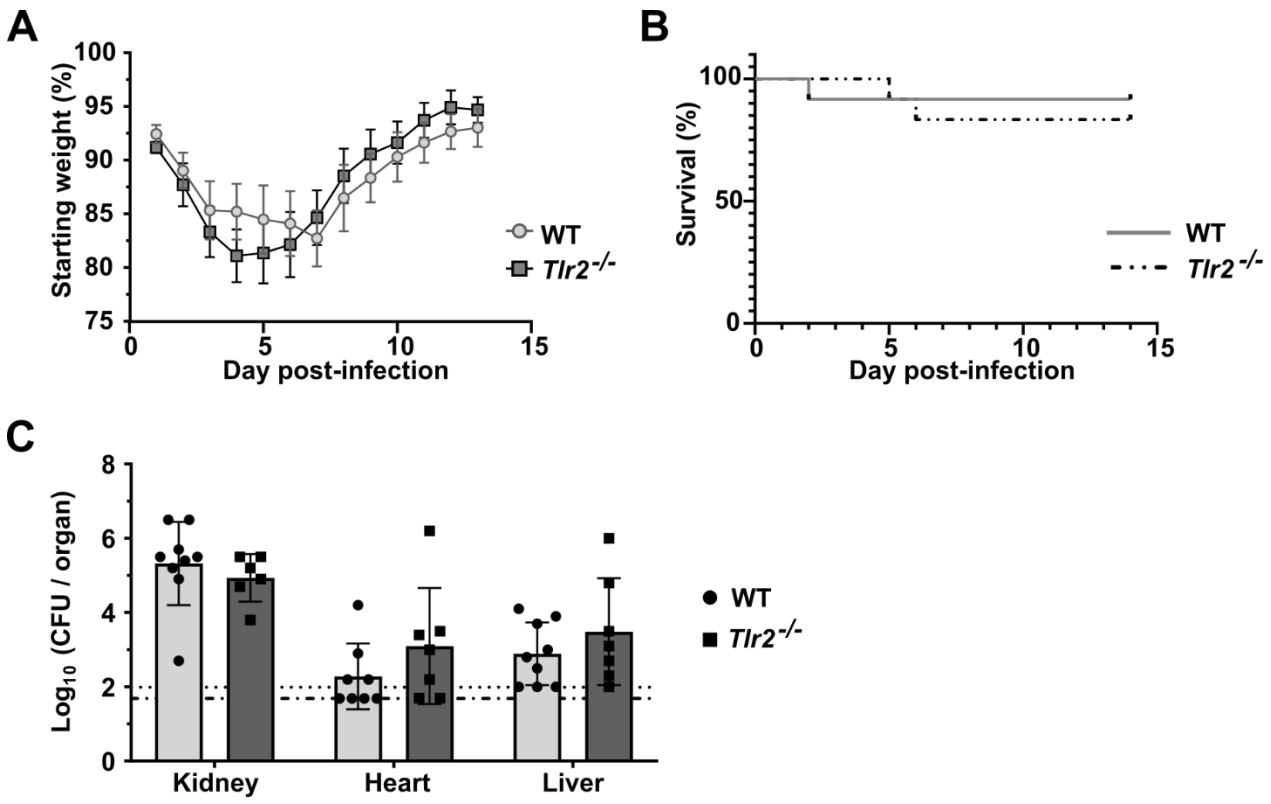

Figure 8. Deficiency in TLR2 does not significantly impact weight loss, survival, or bacterial burden control during intravenous infection with *S. aureus*. WT, male, 9-week-old mice were infected with 5 x 10^6 CFU of WT *S. aureus* via retro-orbital injection. **A.)** Mice were weighed daily over the 14-day infection time course. The average %-starting weight for each genotype is shown with error plotted as standard error of the mean. For WT and *Tlr2*$^{-/-}$, n = 10 mice per group. Groups were compared at each timepoint by multiple t-tests with correction for multiple comparisons. No significant differences were detected. **B.)** Mortality events due to infection were recorded over the course of infection. Mice were monitored daily for humane endpoint criteria and euthanized if needed. Survival curves were compared between genotypes using a Log-rank test. No significant differences were detected. **C.)** Mice surviving until the endpoint of infection at day 14 were euthanized and organs were collected for CFU enumeration. For kidney, n = 9 WT mice and n = 6 *Tlr2*$^{-/-}$ mice. For heart, n = 8 WT mice and n = 7 *Tlr2*$^{-/-}$ mice. For liver, n = 9 WT mice and n = 7 *Tlr2*$^{-/-}$ mice. Results represent one experimental replicate and error is plotted as SD. Log_{10} transformed CFU/organ values were compared by multiple Mann-Whitney tests with correction for multiple comparisons. No significant differences were detected. Dotted lines indicate the Log_{10} transformed limits of detection.

Loss of TLR2 does not impact osteolysis or callus formation during *S. aureus* osteomyelitis

Based on the observation that TLR2 is a major driver of *S. aureus* supernatant-stimulated osteoclastogenesis *in vitro*, we hypothesized that TLR2 contributes to pathologic changes in cortical and trabecular bone during osteomyelitis. To test this hypothesis, we used micro-computed tomography (μCT) to measure and compare callus formation, cortical bone destruction, and trabecular bone volume in WT and *Tlr2*$^{-/-}$ mice subjected to osteomyelitis. There were no significant differences in cortical bone loss, callus formation, or percent-trabecular bone volume/total volume (%-BV/TV) between genotypes (**Fig. 9A-F**). We also performed histomorphometry on histologic sections from infected femurs to evaluate osteoclastogenesis *in vivo* (230,231). There were no significant differences between genotypes (**Fig. 9G**). In summary, our data show that TLR2 does not significantly contribute to bone damage during post-traumatic osteomyelitis.

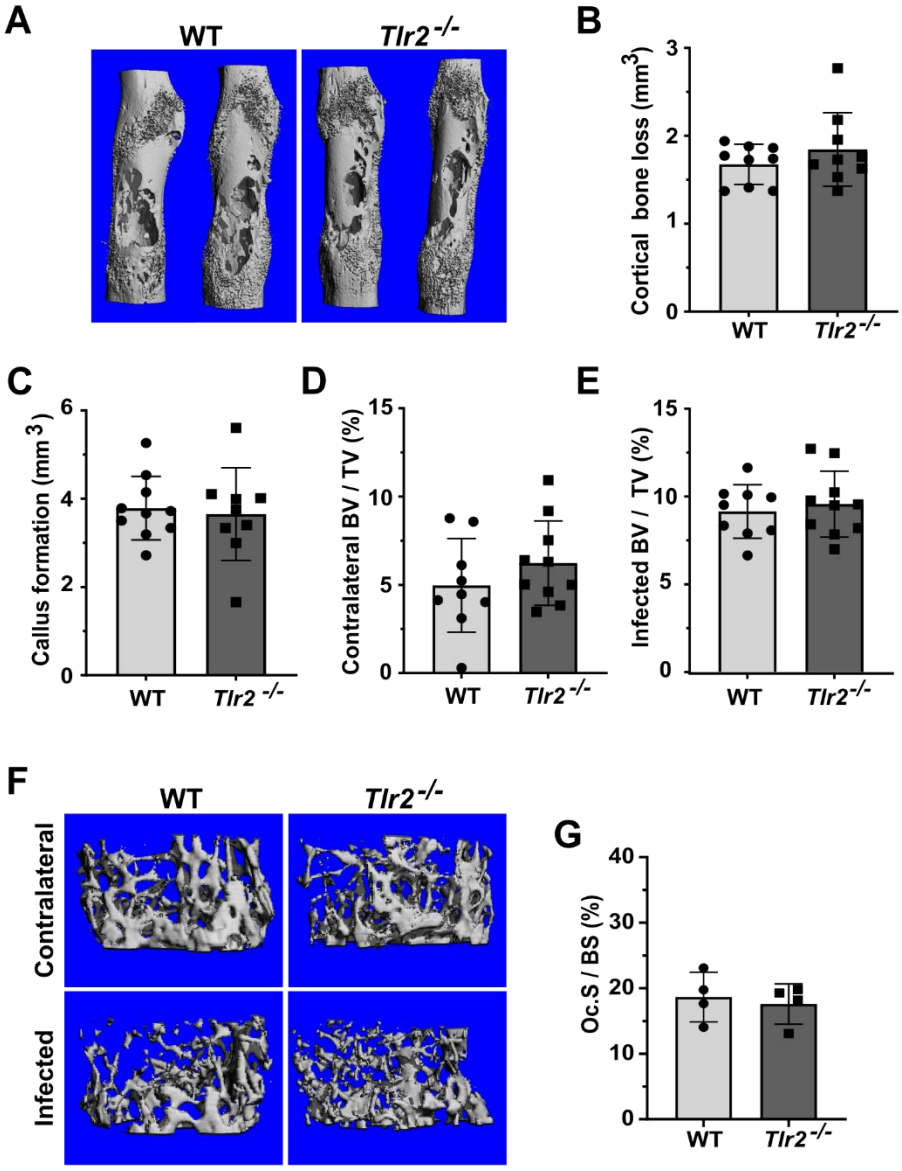

Figure 9. TLR2 does not significantly contribute to bone damage during *S. aureus* osteomyelitis. Mice were subjected to osteomyelitis by intraosseous injection of 10^6 CFU of *S. aureus.* Femurs were extracted on day 14 post-infection. Infected and contralateral femurs were isolated. Bone parameters were assessed using micro-computed tomography (μCT). Results are compiled from two independent experiments. For all graphs, error bars denote SD. If not denoted with asterisks, statistical difference between genotypes was not significant. **A)** Representative 3D images of infected femurs were constructed by μCT **B)** Cortical bone loss was calculated using μCT and values were compared between genotypes by unpaired t-test. For cortical bone, n = 10 for WT and n = 9 for *Tlr2*$^{-/-}$. **C).** Callus formation was measured by μCT and values were compared between genotypes by unpaired t-test. For cortical bone, n = 10 for WT and n = 9 for *Tlr2*$^{-/-}$. **D)** The bone volume/total volume (%-BV/TV) of contralateral femurs was calculated using μCT and values were compared by unpaired t-test. For trabecular bone, n = 9 for WT and n = 10 for *Tlr2*$^{-/-}$ **E)** The %-BV/TV of infected femurs was calculated using μCT and values were compared between genotypes by unpaired t-test. For trabecular bone, n = 9 for WT and n = 10 for *Tlr2*$^{-/-}$. **F)** Representative images of trabecular bone in infected and contralateral femurs are shown. Images represent median infected femur %-BV/TV **G)** Histomorphometry was performed on TRAP-stained femur sections to measure TRAP$^+$ cell surface on trabecular bone relative to total trabecular volume. %-Osteoclast surface/bone surface (Oc.S/BS) was compared between genotypes by Mann-Whitney U test. No significant differences were detected.

Dual loss of TLR2 and TLR9 does not compromise bacterial burden control during osteomyelitis

Since we did not observe TLR2-dependent changes in bone pathology during *S. aureus* osteomyelitis, we hypothesized that other TLRs known to sense staphylococcal PAMPs compensate for the loss of TLR2 *in vivo*. While our *in vitro* studies did not indicate TLR9 to be a driver of osteoclastogenesis during exposure to bacterial supernatants, TLR9 agonism does modulate osteoclast differentiation *in vitro* in models using chemical agonism (13,14,17). Moreover, TLR9 is a major sensor of bacterial DNA and is suggested to modulate immune cell anti-staphylococcal activity *in vitro* (25,31). Therefore, we next sought to determine the impact of dual loss of TLR2 and TLR9 on the pathogenesis of *S. aureus* osteomyelitis. We first assessed whether *Tlr9*$^{-/-}$ mice had any defects in the ability to control bacterial burdens during osteomyelitis. No significant differences in femur, kidney, or liver bacterial burdens between WT and *Tlr9*$^{-/-}$ mice were detected at the end of infection on day 14 (**Fig. 10**). Next, we induced *S. aureus* osteomyelitis in *Tlr2/9*$^{-/-}$ mice. At 1 and 2 dpi there were no differences in femur bacterial burdens between *Tlr2/9*$^{-/-}$ mice and WT. At 5 dpi there was a modest but significant decrease in bacterial burdens in the infected femurs of *Tlr2/9*$^{-/-}$ mice, but this difference was no longer evident by 7 dpi, and there were no significant differences at 14 dpi (**Fig. 11**). To assess whether loss of TLR2 and TLR9 affects host control of bacterial dissemination to organs outside of the infected femur, we measured CFU burdens in the contralateral femur, kidney, liver over a 14-day time course of infection. No significant differences were detected on 1, 2, 5, 7, or 14 dpi (**Fig. 12A-C**). Moreover, experiments were repeated using a lower inoculum dose to ensure that differences in bacterial burdens between genotypes were not obscured by high bacterial loads. No significant differences were detected on 7 dpi, the midpoint of infection (**Fig. 12D**). Since loss of TLRs 2 and 9 did not impact bacterial burden control in osteomyelitis, we next interrogated whether this finding is specific to bone infection. We carried out septic infections in WT and *Tlr2/9*$^{-/-}$ mice. No significant differences were detected in organ bacterial burdens at 4 dpi when comparing *Tlr2/9*$^{-/-}$ to WT mice (**Fig. 13A)**. There was a trend toward greater bacterial burdens in the hearts and livers of *Tlr2/9*$^{-/-}$ mice compared to WT, though this was not statistically significant. Over the course of a 4-day infection, there were no significant differences in %-weight loss between WT and *Tlr2/9*$^{-/-}$ mice (**Fig. 13B**).

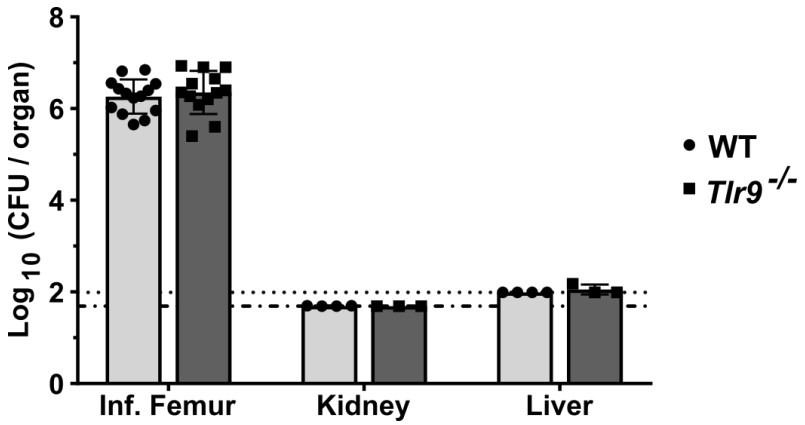

Figure 10. Mice deficient in TLR9 do not incur increased bacterial burdens during osteomyelitis. WT and *Tlr9*$^{-/-}$ mice were subjected to osteomyelitis by intraosseous injection of 10^6 CFU of WT *S. aureus*. Infected femurs, kidneys, and livers were extracted on day 14 post-infection. Organ homogenates were plated for CFU enumeration. Error bars denote SD. Dotted lines indicate Log_{10} transformed limits of detection. CFU burdens were compared by t-test (femur) or Mann-Whitney U test (liver, kidney). If not denoted with asterisks, statistical difference between genotypes was not significant. Results from femurs are compiled from 3 independent experiments, and results from kidneys and livers are compiled from one experimental replicate. For femurs, n = 15 for WT and n = 14 for *Tlr9*$^{-/-}$. For liver and kidneys, n = 4 for WT and n = 3 for *Tlr9*$^{-/-}$.

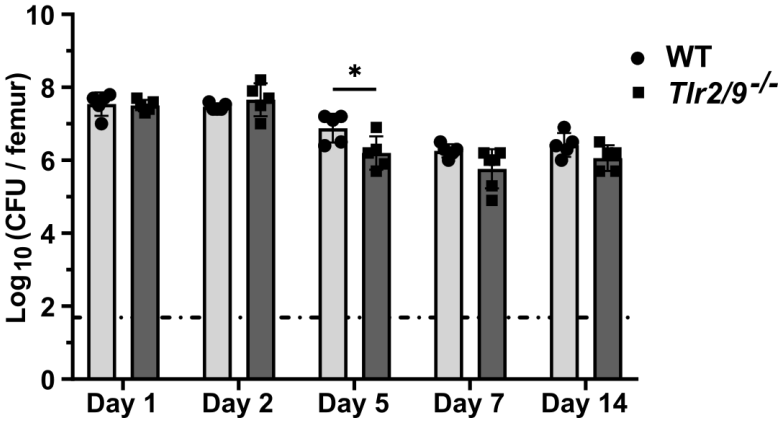

Figure 11. Deficiency in TLR2 and TLR9 does not alter bacterial burdens in the infected femur. WT and *Tlr2/9*$^{-/-}$ mice were subjected to osteomyelitis by intraosseous injection of 10^6 CFU of *S. aureus*. Femurs were collected for CFU enumeration on the indicated days post-infection. The dotted line indicates the Log_{10} transformed limit of detection. Error bars denote SD. Log_{10} CFU burdens were compared between genotypes by unpaired t-test (days 2, 5, and 14), or Mann-Whitney U test (days 1 and 7), depending on data normality. For days 1, 2, 5 and 14, n = 5 per genotype and n = 6 for day 7. *$p < 0.05$.

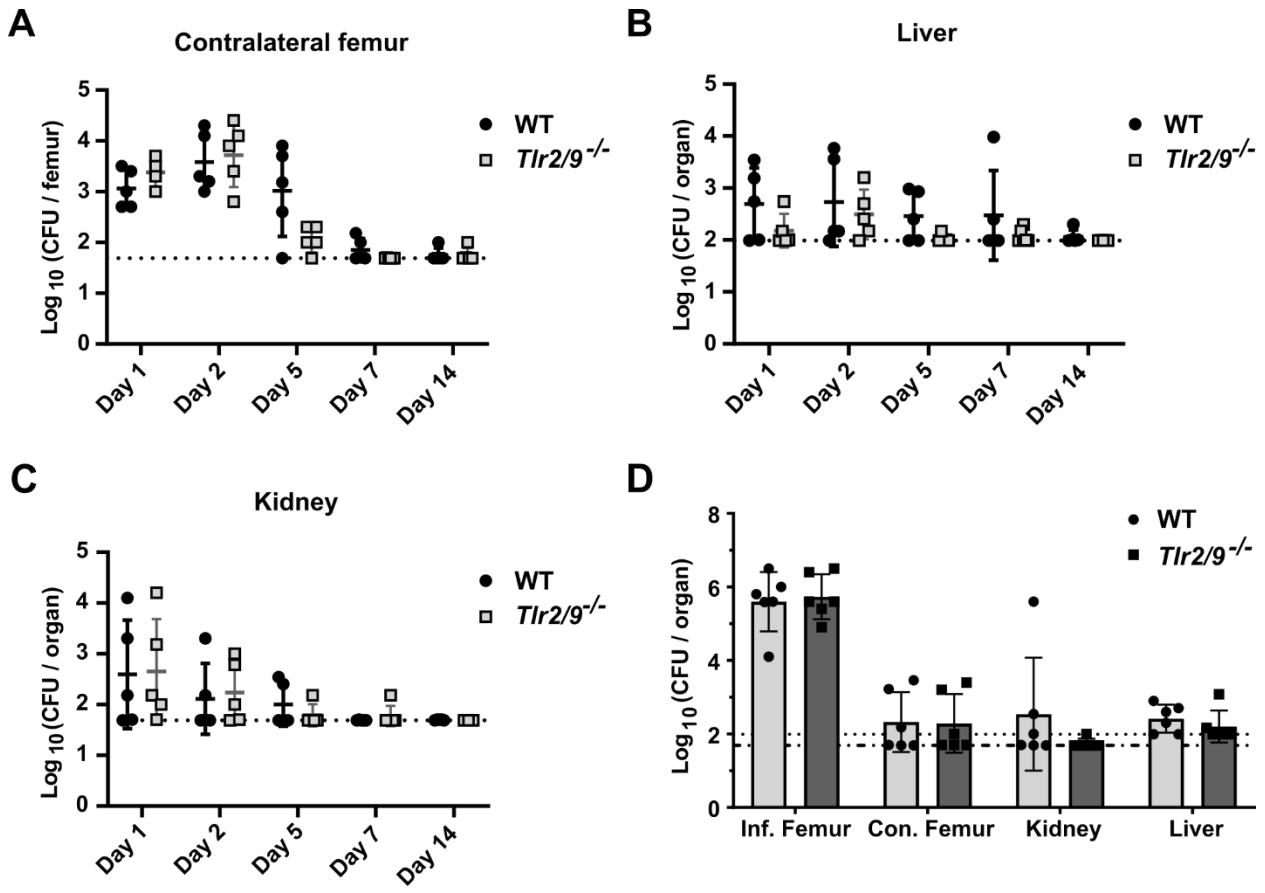

Figure 12. Mice deficient in TLR2 and TLR9 do not incur increased bacterial burdens over multiple infection timepoints. A-C) WT and *Tlr2/9*$^{-/-}$ mice were subjected to osteomyelitis by intraosseous injection of 10^6 CFU of *S. aureus*. Mice were euthanized on the indicated day post-infection and organs were collected for CFU enumeration. CFU burdens from each organ were compared between genotypes for each timepoint using a t-test or Mann-Whitney U test, depending on normality of the data. *$p < 0.05$. If not denoted with asterisks, statistical difference between genotypes was not significant. Error bars denote SD. Dotted lines represent the Log_{10} transformed limits of detection. For days 1, 2, 5, and 14, n = 5 per group. For day 7, n = 6 per group. **D)** WT and *Tlr2/9*$^{-/-}$ mice were subjected to osteomyelitis by intraosseous injection of 10^5 CFU of WT *S. aureus*. Mice were euthanized on day 7 post-infection. Organs were extracted and homogenized for CFU enumeration. CFU burdens were compared between genotypes using a Mann-Whitney U test. No significant differences were detected. n = 5 per group. Error is plotted as ± SD. Dotted lines indicate Log_{10} transformed limits of detection.

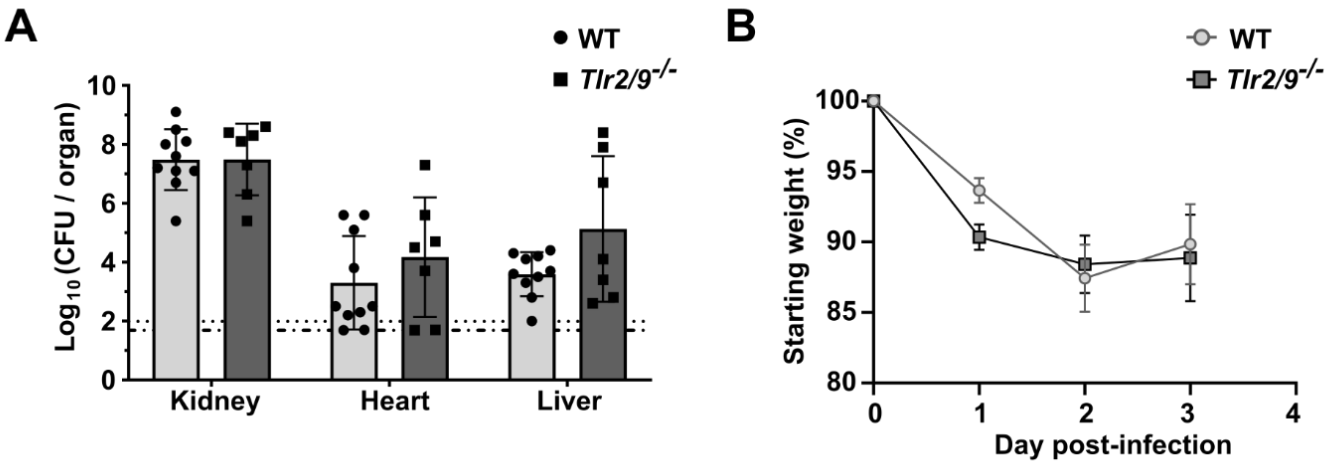

Figure 13. Deficiency in TLR2 and TLR9 does not significantly impact host bacterial burden or weight loss during intravenous infection with *S. aureus*. WT, female, 9-week-old mice were infected with 10^7 CFU of WT *S. aureus* via retro-orbital injection. **A)** At 4 dpi mice were euthanized and organs were collected for CFU enumeration. Results represent one experimental replicate with n = 10 WT mice and n = 7 *Tlr2/9*$^{-/-}$ mice with error plotted as SD. Log_{10} transformed CFU/organ values were compared by multiple Mann-Whitney tests with correction for multiple comparisons. No significant differences were detected. Dotted lines indicate the Log_{10} transformed limits of detection. **B)** Infected mice were weighed daily. The average %-starting weight for each genotype is shown with error plotted as standard error of the mean. The %-starting weights were compared between genotypes by multiple unpaired t-tests with correction for multiple corrections. No significant differences were found.

Dual loss of TLR2 and TLR9 alters callus formation and reduces trabecular bone loss during osteomyelitis

To determine whether loss of both TLR2 and TLR9 alters bone homeostasis during infection, we performed μCT on infected femurs from WT and *Tlr2/9*$^{-/-}$ mice collected at 14 dpi. There were no differences in cortical bone loss between WT and *Tlr2/9*$^{-/-}$ mice (**Fig. 14A-B**). However, *Tlr2/9*$^{-/-}$ mice had a significant decrease in callus formation compared to WT mice (**Fig. 14C**). To determine if the loss of TLR2 and TLR9 alters infection-associated trabecular bone loss, we first performed baseline analyses of uninfected mice to rule out underlying differences in trabecular bone volumes within groups. There were no differences in trabecular measurements between uninfected *Tlr2/9*$^{-/-}$ and WT mice (**Fig. 15A-D**). In infected mice, contralateral and infected femur %-BV/TVs from WT and *Tlr2/9*$^{-/-}$ femurs were compared by two-way ANOVA. This analysis revealed that a significant amount of the variation in these measurements came from the limb type (contralateral versus infected) and from an interaction between the limb type and the mouse genotype (**Fig. 14D-E**). Post-hoc analyses revealed significant differences between the contralateral and infected %BV/TVs for both *Tlr2/9*$^{-/-}$ and WT mice. To better understand the interaction between bone volume and TLR2/9-deficiency, we normalized %BV/TV of infected femurs to the contralateral for each mouse. This analysis revealed that infected *Tlr2/9*$^{-/-}$ mice had significantly greater relative trabecular bone volume compared to WT mice (**Fig. 14F**). To test whether the loss of TLR2 and TLR9 reduces infection-associated osteoclastogenesis, we assessed osteoclast abundance relative to bone volume in the trabecular region using histomorphometry (52). We found no significant differences in osteoclast surface per bone surface between genotypes (**Fig. 14G**). Taken together, these observations suggest that the dual loss of TLR2 and TLR9 significantly reduces reactive callus formation during infection. Loss of TLR2/9 also reduces relative trabecular bone loss, albeit modestly and without a significant reduction in relative osteoclast surface.

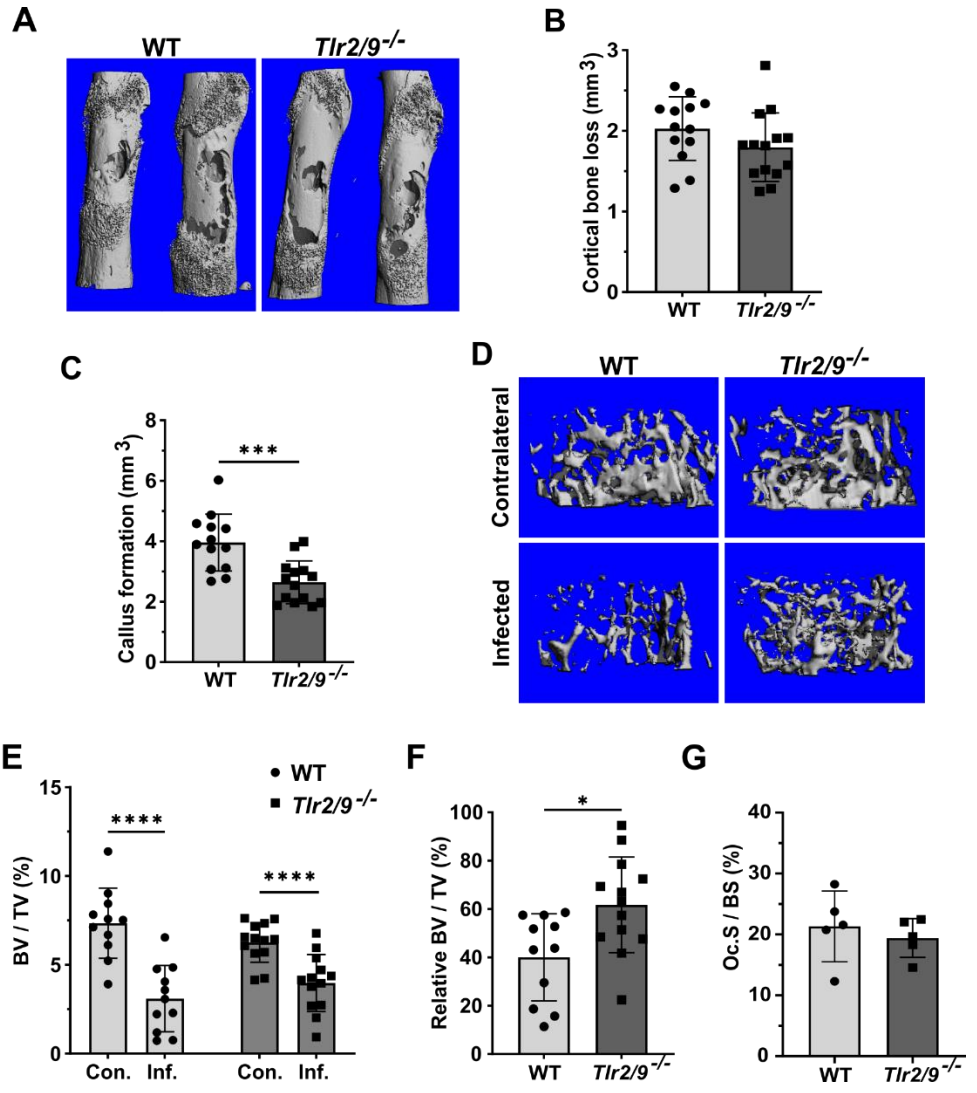

Figure 14. Combined TLR2- and TLR9-deficiency limits infection-induced trabecular bone loss and callus formation. A-H) WT and *Tlr2/9*$^{-/-}$ mice were subjected to osteomyelitis by intraosseous injection of 10^6 CFU of *S. aureus*. For all graphs, error bars denote SD. **A)** Femurs were collected for CFU enumeration on the indicated days post-infection. The dotted line indicates the Log_{10} transformed limit of detection. Log_{10} CFU burdens were compared between genotypes by unpaired t-test (days 2, 5, and 14), or Mann-Whitney U test (days 1 and 7), depending on data normality. For days 1, 2, 5 and 14, n = 5 per genotype and n = 6 for day 7. *p < 0.05. **B-H)** Mice were euthanized on day 14 post-infection and the infected and contralateral femurs were isolated. Bone parameters were assessed using µCT. Results are pooled from independent experimental replicates. For cortical bone, n = 13 for WT and n = 14 for *Tlr2/9*$^{-/-}$ mice. For trabecular bone, n = 11 for WT and n = 13 for *Tlr2/9*$^{-/-}$ mice. If not denoted with asterisks, statistical difference between genotypes was not significant. **B)** Representative 3D images of infected femurs constructed by µCT. **C)** Cortical bone loss was compared between genotypes using an unpaired t-test. **D)** Callus formation was compared between genotypes by unpaired t-test. **E)** Representative images of trabecular bone in infected and contralateral femurs. Images represent median infected femur %-BV/TV. **F)** %-BV/TV values were analyzed by repeated measures two-way ANOVA. ****p < 0.0001 for limb type, p = 0.08729 for genotype and ***p = 0.004 for genotype x limb type. Sidak's test was used to compare %-BV/TV of infected and contralateral limbs within genotypes. ****p < 0.0001. **G)** Infected femur BV/TV was normalized to the contralateral BV/TV and genotypes were compared by unpaired t-test. *p = 0.0109. **H**) Histomorphometry was performed on TRAP-stained femur sections to measure $TRAP^+$ cell surface on trabecular bone relative to total trabecular volume. %-Osteoclast surface/bone surface (Oc.S/BS) was compared between genotypes by Mann-Whitney U test.

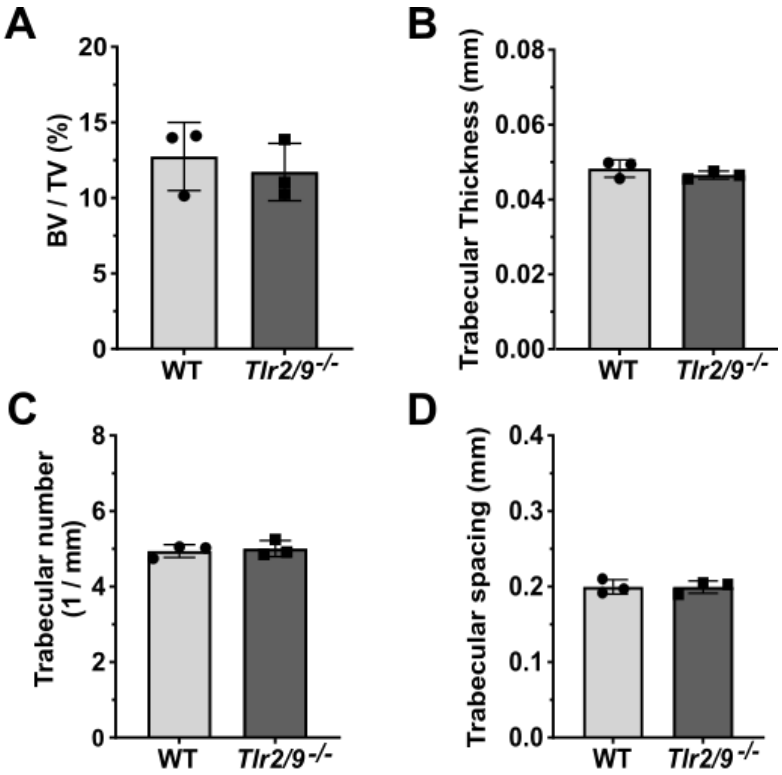

Figure 15. WT and *Tlr2/9*$^{-/-}$ mice have comparable trabecular bone measurements at baseline. 8-9-week-old female mice were euthanized, and femurs were extracted, fixed, and imaged by µCT. Parameters of trabecular bone including %-BV/TV (**A**), trabecular thickness (**B**), trabecular number (**C**), and spacing (**D**) were measured. Comparisons were made between genotypes by Mann-Whitney U test. No significant differences were detected. n = 3 per group. Error bars denote SD.

Compensation by TLR2/9-independent immune responses may sustain cytokine levels during osteomyelitis

Dual deficiency of TLR2 and TLR9 did not have a significant effect on host ability to contain bacteria in the infected bone and did not alter bacterial load in organs secondary to the infectious focus. We next hypothesized that redundancy in innate immune pathways upstream of cytokine production allowed for significant innate immune response to bacteria in the absence of TLR2 and TLR9. To test this, we examined levels of the inflammatory cytokine IL-1β in infected and contralateral femurs from WT and *Tlr2/9*$^{-/-}$ mice that underwent surgical induction of osteomyelitis. IL-1β levels in contralateral femurs were reduced in *Tlr2/9*$^{-/-}$ mice compared to WT mice at 5 and 14 dpi, but this difference was not statistically significant (**Fig. 16A**). There was a large spread in cytokine abundance in infected femurs. No significant differences between *Tlr2/9*$^{-/-}$ and WT were detected (**Fig. 16B**). At 5 and 14 dpi, no significant differences in CFU burdens were detected in *Tlr2/9*$^{-/-}$ compared to WT femurs (**Fig. 16C-D**).

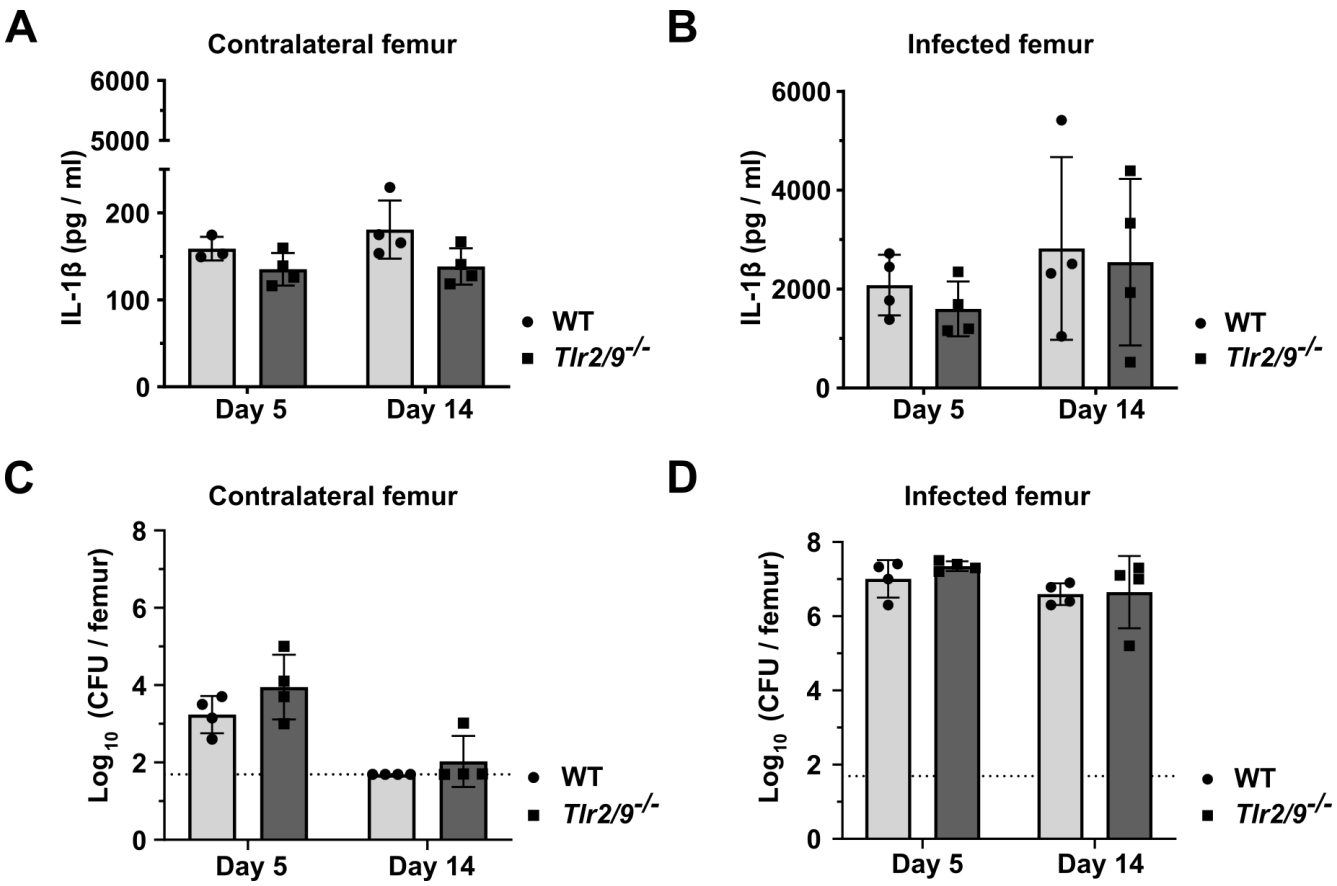

Figure 16. Deficiency in TLR2 and TLR9 does not alter femur IL-1β levels or bacterial burdens. WT and *Tlr2/9*$^{-/-}$ female mice were subjected to osteomyelitis by intraosseous injection of 10^6 CFU of *S. aureus***.** On the indicated dpi, mice were euthanized, and femurs were collected. Femurs were homogenized in a buffer containing protease inhibitor. **A-B)** Homogenates were centrifuged to pellet bone fragments. The supernatant was used in an ELISA to measure IL-1β levels. A Mann Whitney test was used to compare IL-1β levels between *Tlr2/9*$^{-/-}$ and WT femurs for each timepoint. No significant differences were detected. Error is plotted as SD. For contralateral, n = 3 mice for WT and n = 4 mice for *Tlr2/9*$^{-/-}$. For infected, n = 4 mice for both WT and *Tlr2/9*$^{-/-}$. **C-D)** Femur homogenates were plated to enumerate bacterial CFU. A Mann-Whitney test was used to compare Log_{10} transformed CFU/ml values between genotypes for each timepoint. No significant differences were detected. Error is plotted as standard deviation and n = 4 mice for each group.

TLR2- and TLR9-independent mechanisms promote osteoclastogenesis in RANKL-primed precursors during intracellular bacterial infection

Our *in vivo* findings suggest that TLR2 and TLR9 modestly impact infection-induced trabecular bone loss, but do not alter osteoclastogenesis in trabecular bone *in vivo*. To identify whether *S. aureus* can promote osteoclastogenesis through TLR2- or TLR9-independent mechanisms, we next studied the response of RANKL-primed osteoclast precursors to intracellular infection with WT *S. aureus*. We hypothesized that osteoclast precursors deficient in TLR2 and/or TLR9 would maintain the ability to differentiate through bacterial activation of alternative immune pathways. We infected RANKL-primed BMDMs from WT, *Tlr2*$^{-/-}$, *Tlr9*$^{-/-}$, and *Tlr2/9*$^{-/-}$ mice and found that infection significantly increased osteoclast numbers compared to vehicle in all cell genotypes (**Fig. 17A-B**). To control for stochastic differences in osteoclast formation, counts were also normalized to vehicle control for each genotype to quantify the relative magnitude of increase in osteoclastogenesis resulting from infection. This analysis revealed that all genotypes had increased osteoclastogenesis from infection; however, WT cells incurred significantly greater infection-induced osteoclastogenesis than cells lacking TLR2, TLR9, or TLR2/9. (**Fig. 17C**). To confirm that differences in bacterial load did not contribute to differences in osteoclast number identified between genotypes, CFU were enumerated from cell lysates immediately following infection and at 2 dpi. There were no significant differences in bacterial burdens between genotypes immediately after bacterial internalization or at 2 dpi (**Fig. 18A-B**). From these data we conclude that TLR2 and TLR9 are partially responsible for infection-induced osteoclastogenesis in RANKL-primed cells, but TLR2- and TLR9-independent mechanisms contribute significantly to osteoclast formation during intracellular infection.

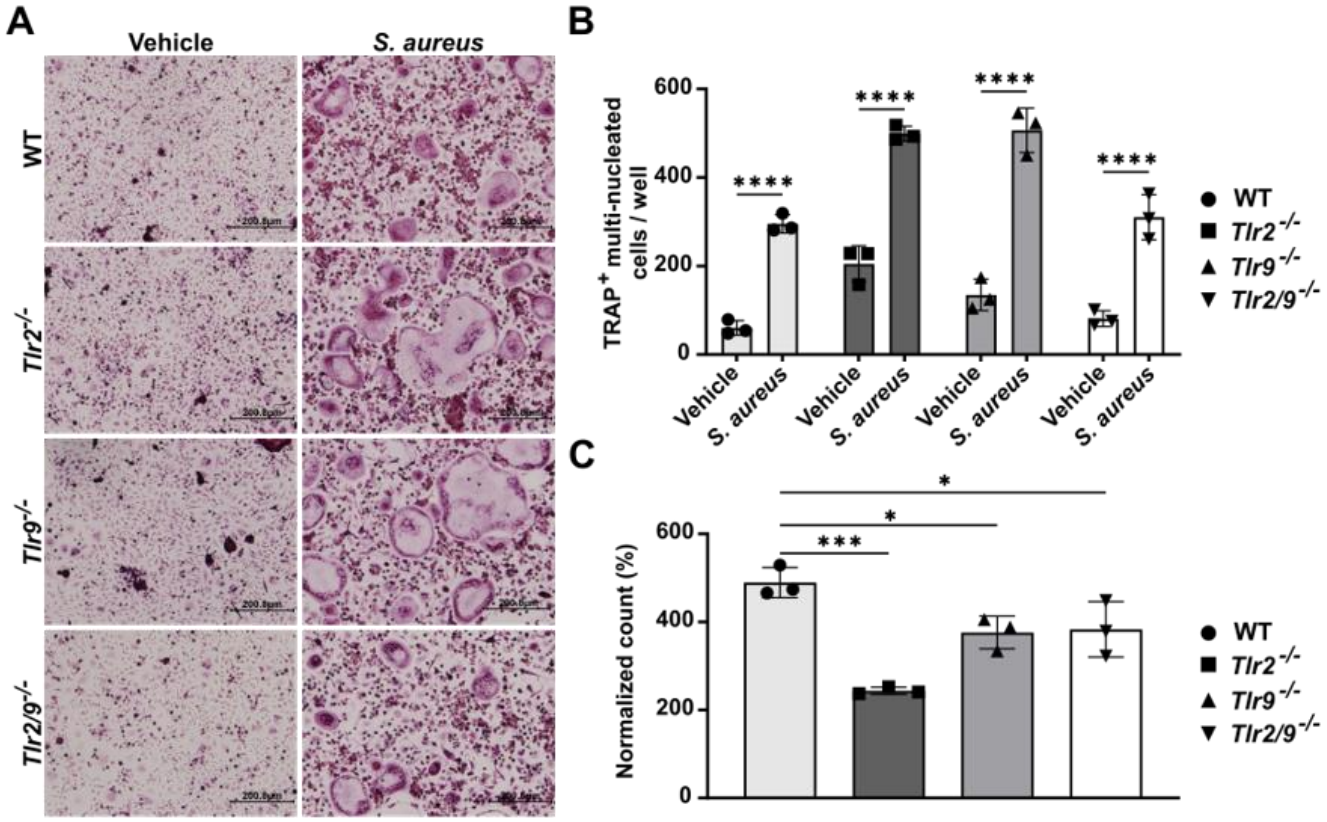

Figure 17. Increased osteoclastogenesis in RANKL-primed precursors infected with *S. aureus* is only partially mediated by TLR2 and TLR9. A-C) BMDMs were cultured with 35 ng/ml RANKL + CMG 14-12 supernatant for 2 days. Cells were then infected with *S. aureus* at an MOI of 25 in the absence of RANKL, using gentamicin protection. For all, *p < 0.05, **p < 0.01, ***p < 0.001, ****p < 0.0001. If not denoted with asterisks, statistical difference between genotypes was not significant. Error bars denote SD, n = 3 technical replicates per group. Data are representative of 3 independent experiments. **A)** Representative images of TRAP-stained cells at day 2 post-infection. **B)** After 2 days of infection, cells were fixed and stained, and $TRAP^+$, multinucleated (3 ≥ nuclei) osteoclasts were quantified. A two-way ANOVA was used to assess the effect of genotype and treatment and Sidak's test was used to compare each vehicle to *S. aureus* for each genotype. **C)** Counts were normalized to vehicle and analyzed by one-way ANOVA and Dunnett's test of multiple comparisons was used to compare each genotype to WT.

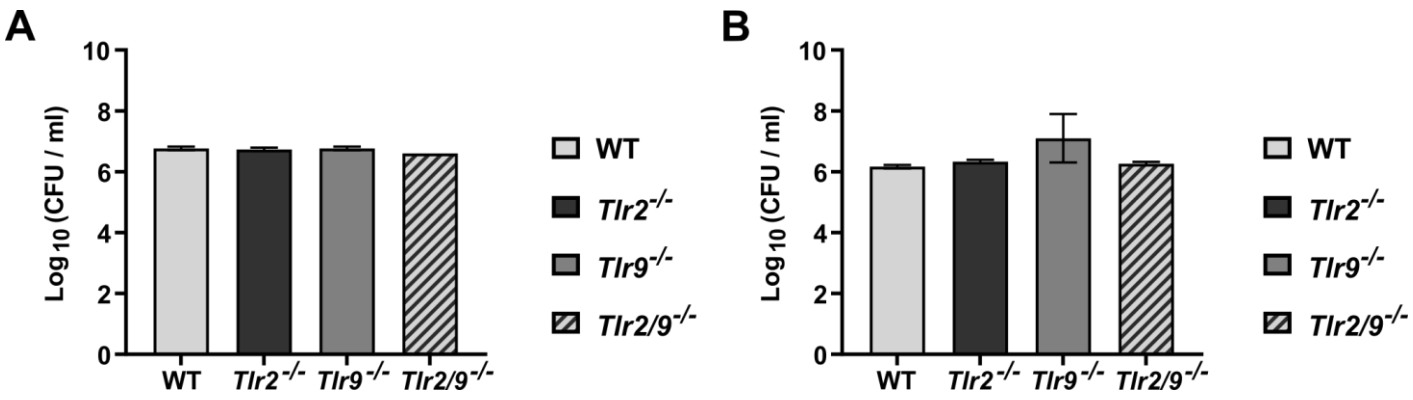

Figure 18. Bacterial load is not affected by loss of TLR2 and/or 9. A-B) BMDMs of the indicated genotype were primed with RANKL + CMG 14-12 supernatant for 2 days. RANKL was withdrawn and cells were infected with WT *S. aureus* at a MOI of 25. CFU were enumerated from cell lysates at the indicated timepoint. Dotted lines indicate the limit of detection. For all, n = 3 technical replicates per group. **A)** Log_{10} CFU were analyzed by nonparametric one-way ANOVA. A Kruskal-Wallis post-hoc test was used to compare CFU between knockout and WT cells and no significant differences were detected. **B)** After 2 days of infection, cells were lysed, serially diluted, and plated to measure CFU. Log_{10} CFU burdens were analyzed by non-parametric one-way ANOVA. No significant differences were detected.

Discussion

Dysregulation of bone homeostasis is a hallmark of osteomyelitis pathogenesis in both animal models and human disease (5,7,22,103). This manifests as both bone loss and abnormal bone formation. While the effects of *S. aureus* toxins contribute to the perturbation of bone homeostasis through direct cell lysis, previous studies indicate that inflammation generated by host sensing of bacteria also contributes to altered bone homeostasis (22,101,103,232–234). The presence of inflammatory cytokines in the bone microenvironment and direct PRR engagement can alter the differentiation and function of bone-resorbing osteoclasts, leading to bone loss (101,102,235,236). Thus, defining the specific pathogen sensing receptors and immune signaling pathways that contribute most to the dysregulation of bone homeostasis is a vital prerequisite to understanding how to limit bone damage during osteomyelitis. In this study, we sought to determine how two PRRs capable of sensing staphylococcal PAMPs, TLR2 and TLR9, contribute to bacterial burden control and dysregulation of bone homeostasis in the specific context of post-traumatic osteomyelitis.

In vitro experiments in this study focused on determining the consequences of *S. aureus* -mediated ligation of TLR2 and TLR9 in osteoclast lineage cells. Prior work has shown that engagement of TLRs 2, 4, and 9 in RANKL-primed osteoclast precursors by purified agonists increases osteoclast formation (125–127). Positive regulation of osteoclastogenesis through TLR engagement is associated with increases in c-Fos expression and parallel changes to the cytokine milieu (126). Our results are in line with these observations, as *S. aureus* supernatant promoted osteoclastogenesis in RANKL-primed precursors in a TLR2-dependent manner. However, this finding did not translate *in vivo*, where TLR2-deficiency did not significantly alter parameters of bone homeostasis nor affect relative osteoclast surface. Thus, although the role of TLR2 in driving osteoclastogenesis has been relatively straightforward in cell culture studies, our *in vivo* results suggest that TLR2 plays a less crucial role in bone loss during osteomyelitis. This finding is reflected in previous publications demonstrating that the role of TLR2 in bone loss varies by infection model (130,232,234,237). The most unequivocal evidence that TLR2 can act as a modulator of trabecular bone loss comes from a 2013 study in which mice were intravenously administered formaldehyde-fixed *S. aureus* or chemical TLR2 agonists. Trabecular bone loss occurred in a TLR2-dependent manner, in line with parallel *in vitro* experiments (130). The disparity between these data and the current study may reflect the differences in modeling systemic TLR2 engagement with purified PAMPs versus infection with live bacteria, which are capable of dynamic metabolism, virulence factor production, and replication to provide a wide variety of pathogen-derived molecules for host detection.

The potential for redundancy in innate immune pathways provided a rationale for testing the effect of dual loss of TLR2 and TLR9, with the expectation that *Tlr2/9*$^{-/-}$ mice would have reduced bone loss, reduced osteoclast surface, and less dysregulation of bone homeostasis during osteomyelitis. *Tlr2/9*$^{-/-}$ mice had a modest attenuation of trabecular bone loss, supporting our hypothesis that compensation between TLR2 and TLR9 limited the effects of TLR2-deficiency on bone loss. However, there was no concomitant decrease in relative osteoclast surface. Taken alongside data showing that TLR2- and TLR9-deficient osteoclast precursors undergo osteoclastogenesis upon intracellular infection with *S. aureus*, these data suggest that TLR2- and TLR9-independent pathways have the potential to modulate osteoclastogenesis during osteomyelitis. For instance, the detection of damage-associated molecular patterns (DAMPs) could be contributing to inflammatory bone damage through other innate immune receptors. TLR4 has been shown to promote osteoclast-mediated bone erosion during arthritis through detection of neutrophil-derived S100A8/A9, presenting the possibility that TLR4 plays a role in osteomyelitis, even in those cases triggered by Gram-positive pathogens (238). Moreover, cell types outside of the osteoclast compartment may influence osteoclastogenesis in a cell-extrinsic manner that is not solely dependent on TLR2 and TLR9. Because prior exposure to RANKL determines whether a BMDM can differentiate into an osteoclast upon TLR engagement, it is possible that changes to osteoclastogenesis may occur in *Tlr2*$^{-/-}$ and/or *Tlr2/9*$^{-/-}$ mice, but because of opposing effects of TLR ligation pre- and post- RANKL, net osteoclastogenesis is unchanged (123,126,127,205,239). Exposure to RANKL blunted release of most of the cytokines we measured. However, RANKL-primed WT and TLR2-null cells retained the ability to produce small amounts of IL-6 and IL-1α, presenting the possibility that, in microenvironments containing RANKL, NF-κB activation through the RANK receptor could augment cytokine release downstream of TLRs. Thus, the *in vitro* and *in vivo* findings presented here support the notion that TLR2- and 9-independent mechanisms, including engagement of other PRRs, cytokine signaling, as well as activation of undiscovered innate immune pathways, function in osteoclast lineage cells to drive pathologic changes to bone during *S. aureus* infection.

We observed that *Tlr2/9*$^{-/-}$ mice had significant decreases in callus formation. Although callus formation is a normal part of fracture repair, we observed that mice with osteomyelitis do not reach healing resolution around the bacterial inoculation site (22,38,51). Thus, excessive callus formation is aberrant in the setting of infection. Our results suggest that TLR2 and TLR9 are influencing bone forming cells, likely mesenchymal stromal cells such as osteoblasts, to promote callus formation. TLR signaling can occur in osteoblasts, with several articles reporting that TLR2 and TLR4 signaling alters osteoblast differentiation and RANKL presentation (209,240–242). However, *in vivo*, loss of TLRs 2, 4,

and 9 did not alter fracture repair in a calvarial model of bone healing, while abrogation of interleukin-1 type 1 receptor (IL-1R1) signaling significantly enhanced defect closure (236). Thus, it is possible that TLR2 and TLR9 alter osteoblast activity during osteomyelitis by modulating elaboration of IL-1R1 cytokines.

Our results demonstrate that neither TLR2 nor TLR9 significantly contributes to host control of bacterial burdens in the model of post-traumatic osteomyelitis we used, suggesting that other pathways may play more prominent roles in constraining *S. aureus* infection in bone. Evidence that TLR2 is critical to host defense against *S. aureus* originated in a mouse model of intravenous septic infection, where receptor deficiency significantly accelerated host mortality (144). Furthermore, in a *S. aureus* craniotomy biofilm infection model, TLR2, but not TLR9, was critical for host bacterial containment through caspase1-mediated activation of IL-1β, which was reduced in *Tlr2*$^{-/-}$ mice (199). Despite these findings, the conclusion that TLR2 exerts a significant effect on host anti-staphylococcal defenses has not been fully supported by all studies, with results varying based on tissue specificity and the infection model (108,142,144,145,234). Additionally, in sepsis, only mice deficient in myeloid differentiation factor 88 (MyD88) incurred significantly increased bacterial burdens in blood and organs at multiple points, highlighting that MyD88-driven signaling pathways in addition to TLR2 heavily contribute to anti-staphylococcal defenses (144). Cytokine elaboration likely underlies MyD88-driven host control of bacterial burdens in disparate infection sites, even when different upstream receptors are required for activation. To this point, activation of cytokines, namely IL-1β and TNF-α, are critical for host control of bacterial expansion and immune cell recruitment in bone and implant-associated infection (51,111,232). Our measurements of IL-1β in the infected and contralateral femurs following induction of *S. aureus* osteomyelitis did not significantly differ between from WT and *Tlr2/9*$^{-/-}$ mice. Additional experiments must be done to substantiate this finding, but it overall suggests that redundancy in host bacterial detection enables a sufficient immune response to *S. aureus* when TLRs 2 and 9 are absent.

Our study has limitations that should be considered when interpreting the data. First, because we relied mainly on *in vitro* measurements of osteoclastogenesis to provide rationale for our *in vivo* studies and to substantiate *in vivo* findings, conclusions on TLR2- or TLR9-dependent changes to cellular function, such as osteoclast resorption, cannot be drawn from the data. Additionally, previous studies have indicated that cytokines are major drivers of osteoclast bone resorption during infection *in vitro* with *S. aureus* and can drive osteoclastogenesis *in vivo* (120). To better understand why mice lacking TLR2 and TLR9 did not have significant decreases in osteoclastogenesis or changes to bacterial burden control *in vivo*, it will be important to understand how cytokines are affected by the loss of these receptors. IL-1R1 cytokines are major influencers of bone pathology during osteomyelitis and

in inflammatory bone loss more generally (51,102). Thus, exploration into the pathways upstream of inflammasome activation will be critical in future work. Finally, our studies revealed a strong impact of TLR2 and TLR9 on callus formation. Studying osteoblast-mediated bone pathology during osteomyelitis is also an important future direction for this work.

Overall, this study shows that, despite the clear role of TLR ligation in governing osteoclast differentiation in cell culture, TLR2 and TLR9 signaling contributes only modestly to inflammatory bone loss during *S. aureus* osteomyelitis. Importantly, reduction in bone loss came without significant change in relative osteoclast surface in the trabecular bone. Interestingly, our work shows that TLR2 and TLR9 may contribute to callus formation. Because loss of TLR2 and TLR9 did not alter control of bacterial burdens, other innate immune pathways may be more influential in promoting host responses to osteomyelitis. Continued work on the role of inflammation-generating host responses will be critical to uncovering the specific mechanisms at play in osteolysis during infection.

CHAPTER III: THE ROLE OF THE INFLAMMASOME IN THE OSTEOCLAST RESPONSE TO *STAPHYLOCOCCUS AUREUS* OSTEOMYELITIS

Introduction

Inflammation is a classic double-edged sword; a strong immune response to pathogen is critical to host survival, yet if inflammation becomes too intense, tissue damage results. In *Staphylococcus aureus* osteomyelitis, inflammation generated by the immune response to bacteria alters the differentiation and function of bone cells, resulting in loss of homeostasis and bone damage. Interleukin-1 receptor type 1 (IL-1R1) cytokines IL-1α and IL-1β have been identified as major regulators of bone homeostasis in inflammatory diseases of bone including osteomyelitis (102). These IL-1R1 cytokines profoundly impact bone-resorbing osteoclasts by promoting differentiation of progenitor cells and by enhancing resorption by mature cells (112,119). In the context of *S. aureus* infection, IL-1R1 cytokines also promote the host immune response, in part by mediating the neutrophil recruitment to the infection site (51,109). Thus, the IL-1R1 signaling axis is of central importance to infection resolution, but IL-1R1 responses can come at an expense to bone health and homeostasis. Though the effects of IL-1α and IL-1β on osteoclast differentiation and resorption have been well-characterized, fewer studies have focused on the pathways responsible for activating these cytokines during bone infection. This is particularly important for the activation of IL-1β, which is produced in a pro form and requires proteolytic processing to liberate its biologic activity (162,175) The nucleotide binding and oligomerization, leucine-rich repeat, pyrin domain-containing 3 (NLRP3) inflammasome is a major activator of IL-1β (162,243). The NLRP3 inflammasome can also initiate pyroptosis, a highly inflammatory form of cell death (163). The aim of this chapter is to understand the contribution of the NLRP3 inflammasome to both anti-staphylococcal defenses and bone damage during *Staphylococcus aureus* osteomyelitis.

NLRP3 is sensor of cellular damage that assembles into a multiprotein complex upon priming through a pattern recognition receptor (PRR), which initiates nuclear factor-kappa B (NFkB) responses, followed by exposure to damage-related stimuli, including potassium efflux and reactive oxygen species (152,161,162). The NLRP3 inflammasome is comprised of caspase-1, apoptosis-associated speck-like protein containing CARD (ASC), and NIMA-related kinase 7 (NEK7) (152). When assembled in the complex, caspase-1 auto-activates and subsequently cleaves and activates substrates including pro-IL-1β, pro-IL-18, and pro-gasdermin D. In some cell types, gasdermin D cleavage into its N-terminal form results in pyroptotic cell death (163). The NLRP3 inflammasome promotes host responses to *S.*

aureus in multiple infection sites (109,156,200). NLRP3 activation and the IL-1R1 signaling axis are activated in both mouse models and human cases of osteomyelitis (51,111,194). The inflammasome has also been shown to play a role in promoting fracture healing and bone homeostasis (195,196). The cell types involved in inflammasome-based regulation of bone homeostasis have not been identified and it is not clear as to whether osteoclast precursors or mature cells can activate an inflammasome. In this chapter, we test the hypothesis that osteoclast lineage cells activate the inflammasome in response to *S. aureus*, thereby promoting dysregulation of bone homeostasis. Osteoclasts arise from the myeloid lineage, differentiating from monocytes into large, multinucleated, bone-resorbing cells in response to the canonical differentiation factor receptor activator of NFκB ligand (RANKL) (54). Transcriptional and epigenetic reprogramming occur during the differentiation process, known as osteoclastogenesis (93,227,244). The monocytic osteoclast precursor cell also harbors the potential to become a macrophage (245). Importantly, macrophages are potent activators of NLRP3 and engage this response during exposure to live *S. aureus* and staphylococcal toxins (27,28). Whether osteoclasts can engage in a comparable inflammasome response via NLRP3 is not known. While Chapter II mainly examined how host detection of *S. aureus* through PRRs alters osteoclast differentiation, this chapter focuses on the osteoclast's capacity to directly respond to pathogens by mounting an inflammatory response. We also explore how the broader inflammatory consequences of inflammasome activation and cell death influence bone homeostasis in a mouse model of *S. aureus* osteomyelitis.

Materials and Methods

Animal use

C57BL/6J mice (Jackson stock #000664) were used for all *in vivo* and *in vitro* experiments that employed wild type (WT) animals as controls. WT control mice used in the osteomyelitis model were ordered from The Jackson Laboratory (Bar Harbor, ME) and delivered to our housing facility 1-2 weeks prior to undergoing surgery. *Nlrp3*$^{-/-}$ mice (Jax stock #21302, B6.129S6-Nlrp3tm1Bhk/J) were ordered from The Jackson Laboratory for use in osteomyelitis experiments (246). *Nlrp3*$^{-/-}$ mice arrived at our facility 1-2 weeks prior to the procedure. *Nlrp3*$^{-/-}$ mice were housed with sterile food/bedding. *Caspase1/11*$^{-/-}$ mice (Jax stock #016621, B6N.129S2-Casp1tm1Flv/J) were gifted to our lab by Dr. Young Kim at Vanderbilt University (247). Mice were bred in-house via homozygous crosses. *Caspase1/11*$^{-/-}$ mice were utilized for whole bone marrow collection or used in osteomyelitis experiments. For all genotypes, mice underwent surgical induction of osteomyelitis at 7-8 weeks of age.

Bacterial strains and growth conditions

Experiments were performed with either the erythromycin- and tetracycline-sensitive, USA300-lineage, LAC clinical isolate strain of *S. aureus* (AH1263, referred to as WT) or a derivative strain lacking the alpha-type phenol-soluble modulins (Δ*psmα1-4*) (22,214). Bacterial cultures used in both *in vitro* and *in vivo* infection experiments were grown overnight at 37°C in tryptic soy broth (TSB) with shaking at 180 rpm. 10 μg/ml erythromycin was added to the culture media of the Δ*psmα1-4* strain. Bacterial inocula were prepared by back-diluting overnight cultures 1:100 into TSB and then incubating an additional 3 h at 37°C with shaking at 180 rpm. The subcultures were then centrifuged for 5 min at 4000 x g to pellet bacterial cells. The bacterial inoculum was adjusted to the desired concentration by diluting in 1X phosphate-buffered saline (PBS) and measuring optical density. All post-infection CFU were enumerated after growth on trypticase soy agar (TSA) plates.

Preparation of bacterial supernatants

Concentrated bacterial supernatants were prepared as previously reported (22). In brief, 1-2 bacterial colonies were inoculated into 250 ml Erlenmeyer flasks containing 50 ml of sterile RPMI medium with 1% casamino acids (Fisher Scientific). Flasks were sealed with rubber stoppers and cultured for 15 h at 37°C and shaking at 180 rpm. To pellet bacteria, cultures were then centrifuged at 4000 x g for 10 min. To prepare concentrated supernatants, culture supernatants were sterilized using a 0.22 μm polyethersulfone filter and then concentrated to a final volume of ~1.5 ml using an Amicon Ultra 3-kDa nominal molecular weight column (MilliporeSigma, Burlington, MA). Supernatants were again filter sterilized and single-use aliquots were prepared on ice and frozen at −80°C.

Unconcentrated supernatants were prepared by inoculating 1 colony into a 50 ml conical containing 15 ml of sterile RPMI medium with 1% casamino acids (Fisher Scientific). Cultures were grown anaerobically (caps sealed) for 15 h at 37°C and shaking at 180 rpm. To pellet bacteria, cultures were then centrifuged at 4000 x g for 10 min. Culture supernatants were then filter-sterilized twice. Single-use aliquots were prepared on ice and frozen at −80°C.

Whole bone marrow isolation and bone marrow-derived monocyte enrichment

Whole bone marrow (WBM) was isolated from male or female C57BL/6J mice aged between 8 and 12 weeks. WBM was flushed from femurs using unsupplemented MEM-α medium (Gibco, Waltham, MA), passed through a 100 μM cell strainer, and centrifuged at 1500 rpm x 5 min. Red blood cells were lysed in ammonium-chloride-potassium buffer for 10 min, and then 1X PBS was added to deactivate lysis. Cells were centrifuged again and resuspended in 100% fetal bovine serum (FBS) for

counting. WBM cell preparations were then frozen in 10% dimethyl sulfoxide (DMSO) in FBS and stored in liquid nitrogen until ready to use. Cryopreserved vials of WBM cells were rapidly thawed in a 37°C water bath and then washed in MEM-α medium supplemented with 10% FBS and 1X penicillin-streptomycin to remove DMSO. To enrich for bone marrow-derived monocytes (BMDMs), WBM cells were seeded at 8-10 million cells per 10 cm tissue culture-treated dish in MEM-α medium + 10% FBS + 1X penicillin-streptomycin supplemented with macrophage colony-stimulating factor (M-CSF). Supernatant from the CMG14-12 cell line served as the M-CSF source and was added at a vol/vol ratio of 1:10, providing a high dose of M-CSF for positive selection of monocytes (72). After four days of differentiation, BMDMs were scraped off 10 cm dishes and plated for macrophage or osteoclast differentiation.

Osteoclast and macrophage differentiation

BMDMs were differentiated from WBM as described in the above section. After 4 days of culture, cells were scraped off 10 cm dishes. Depending on the downstream assay, BMDMs were either seeded at 50,000 cells/well into 96-well plates or at 250,000 cells/well into 24-well plates. For all ELISA experiments, cells were cultured in 96-well plates. For experiments involving protein collection for western blot or RNA isolation for qRT-PCR, 24-well plates were used for cell culture. Unless otherwise noted, cells were cultured in MEM-α medium supplemented with 10% FBS and 1X penicillin-streptomycin (referred to as culture media). Macrophages were differentiated in culture media containing CMG 14-12 supernatant at a vol/vol ratio of 1:40 to provide an M-CSF source (248). In 96-well plates, osteoclasts were maintained in culture media with CMG 14-12 supernatant at 1:40 and recombinant receptor activator of nuclear factor (NF)-κB (RANKL) (R&D Systems catalog #462-TR) at 35 ng/ml (96-well plate) or 100 ng/ml (24-well plate). RANKL stimulation continued for either 2 days to generate pre-osteoclasts, which are not yet multinucleated and are still upregulating the osteoclast differentiation program, or 5-7 days to generate mature osteoclasts. Macrophage comparators were cultured in parallel for the same duration. For all, culture medium was changed every 2 days. All cell cultures were incubated at 37°C with 5.0% CO_2.

Nanostring Ncounter

BMDMs were cultured in 24-well plates for 2 or 7 days in culture media supplemented with CMG 14-12 supernatant (macrophages) or with 35 ng/ml RANKL and CMG 14-12 supernatant. Cells cultured for 2 days in RANKL were considered pre-osteoclasts, and cells cultured for 7 days in RANKL were considered mature osteoclasts. Cells were stimulated for 6 h with concentrated supernatant from the

Δ*psmα1-4* strain of *S. aureus* or an RPMI medium control. After the stimulation, cell monolayers were washed once in warm 1X PBS and then collected in Buffer RLT (Qiagen, Germantown, MD) supplemented with β-mercaptoethanol. Cell lysates were obtained by centrifugation in a Qiashredder column (Qiagen) at 13,000 rpm for 2 min. Samples were frozen at -80C prior to RNA isolation using the RNeasy Kit, according to manufacturer's instructions. RNA concentrations were measured using a Biotek Synergy HT Microplate Reader (Agilent Winooski, VT). Each biological replicate represents a separate cell culture experiment, though RNA was isolated for all replicates at the same time. The NanoString assay was performed by the Vanderbilt Technologies for Advanced Geonomics (VANTAGE) Core using the nCounter Mouse Immunology Panel V2 (catalog #115000052) on the nCounter Max Analyzer (NanoString, Seattle, Washington). 100 ng of RNA per sample was input into the hybridization reaction.

Inflammasome induction using TLR agonists

Macrophages and osteoclasts were primed with 500 ng/ml of lipopolysaccharide (LPS) derived from *E. coli*. Stimulation was carried out for 3 – 4 h, as indicated in the figure legend, to prime cells for induction of the inflammasome. Nigericin at 15μM concentration (Invivogen catalog #tlrl-nig) was used as a second signal inflammasome inducer. Priming was always done in serum-free media supplemented with supernatant from the CMG 14-12 cell line and RANKL, as appropriate.

Protein isolation and purification

Protein isolation and purification was performed using a protocol provided by Dr. Igor Brodsky of U Penn. Cells were stimulated in serum-free media. At the indicated collection timepoint, the plates were centrifuged at 1200 rpm at 4°C for 5 min to pellet debris. Cell supernatants were then collected into pre-cooled Eppendorf tubes containing a protease inhibitor cocktail. 6N Trichloroacetic acid (TCA) was then added to each tube at a volume equivalent to 10% of the sample volume. Samples were mixed by inverting and stored at 4°C overnight. TCA precipitation was continued the next day. Tubes were centrifuged at 14,5000 x g for 15 min at 4°C to pellet protein. Pellets were washed three times by resuspending in cold 100% acetone and centrifuging at 14,500 x g for 10 min (1st wash) or 5 min (2nd and 3rd washes). Acetone was removed and samples were dried on a 55°C heat block with Eppendorf tube lids open for 3-5 mins. A buffer containing 4% SDS and 0.5M Tris HCL spiked with 25mM dithiothreitol (DTT) was mixed at a 1:1 ratio with 2X Laemmli buffer containing 10% β-mercaptoethanol. Using this buffer, each pellet was resuspended in a 48 μl volume and then boiled at 100°C for 10 min. Samples were stored at -80°C or immediately loaded onto an SDS-PAGE gel.

Cell lysates were collected by adding 100 µl of lysis buffer (20 mM HEPES pH 7.5, 150 nM NaCl, 10% Glycerol, 1% Triton X, 1mM EDTA in water) supplemented with protease inhibitor (Roche, catalog # 04693124001) to the culture plate. The plate was placed on a shaker at 4°C for 5 min. Then each well was scraped with a sterile, ice-cold p100 pipette tip. Lysates were collected into pre-cooled Eppendorf tubes and rested on ice for 5 mins. Tubes were then centrifuged at 13,000 rpm for 15 min. 68 µl of the supernatant was moved to a new tube with Laemmli buffer at a final concentration of 1X and β-mercaptoethanol at a final concentration of 7% vol/vol. Samples were boiled at 100°C for 10 min and either stored at -80°C or immediately loaded onto an SDS-PAGE gel.

Immunoblot

Protein samples were size-separated by electrophoresis using the BioRad Mini-PROTEAN Tetra Cell system. Cell supernatant or lysate samples were loaded into 12% SDS-PAGE gels (BioRad mini-PROTEAN gel, catalog # 4561041) at a volume of 40 µl/well. Gels were run on ice starting at 55 V and were incrementally turned up to 120 V. Proteins were transferred to nitrocellulose membranes using a Trans-Blot Turbo machine (Bio-Rad, catalog # 1704150) on the mixed molecular weight (lysate samples) or low molecular weight (supernatant samples) settings. Membranes were blocked in Intercept Blocking Buffer (Li-Cor, catalog # 927-70001) for 45 min – 1 h with gentle shaking at RT. Membranes were then incubated overnight in primary antibody at 4°C with gentle shaking. The primary antibodies and concentrations used are as follows: anti-β actin (Sigma #A5441 at 1:2000), anti-caspase-1 (AdipoGen # AG-20B-0042-C100 at 1:1000), anti-gasdermin D (Abcam #ab209845 at 1:1000), anti-IL-1β (R&D Systems # AF-401-NA at 0.25 µg/ml), and anti-TLR2 (Abcam # ab209217). Following primary antibody incubation, membranes were washed 3 times x 5 min in 0.1% Tween in 1X PBS (PBS-t). Membranes were then incubated with fluorescent secondary antibodies at 1:10,000 in 0.1% PBS-t for 1-2 h. The secondary antibodies used include: IRDye 800CW goat anti-rabbit (Li-Cor catalog # 26-68071), Alexa 680 goat anti-mouse (Life Technologies catalog #A21057), IR Dye 680 donkey anti-mouse (Li-Cor catalog #926-68072), and IRDye 800CW donkey anti-goat IgG (Li-Cor catalog #926-32214). Membranes were again washed in PBS-t for 3 x 5 min. Membranes were washed one more time in 1X PBS and then immediately imaged using the Odyssey CLx Imager (Li-Cor, Lincoln, NE). Fluorescent intensities of protein bands were quantified using the Image Studio 4.0 software (Li-Cor, Lincoln, NE). Figures were made using Sciugo.

Quantitative real time- polymerase chain reaction (qRT-PCR)

After stimulating with LPS derived from LPS derived from *E. coli* (Invivogen, catalog #tlrl-eblps), cells were lysed using Buffer RLT Plus (Qiagen, Germantown, MD) supplemented with 10% β-mercaptoethanol. Cell lysates were obtained by centrifugation in a Qiashredder column (Qiagen, Hilden, Germany) at 13,000 rpm for 2 min. RNA was extracted from cell lysates using the RNeasy Mini Plus Kit (Qiagen) in accordance with the manufacturer's instructions. RNA concentrations were measured using a Biotek Synergy HT Microplate Reader (Agilent Winooski, VT). 500 ng of RNA per sample used to synthesize cDNA using the qScript XLT cDNA Supermix (QuantaBio, Beverly, MA). cDNA was diluted 1:10 in nuclease-free water and frozen at -20°C until ready to use. qRT-PCR was performed using iQ Sybr Green Supermix (Bio-Rad, Hercules, CA). The following primer sequences were used: *Nlrp3*-FW 5'- TGCTCTTCACTGCTATCAAGCCCT-3', *Nlrp3*-RV-5'-ACAAGCCTTTGCTCCAGACCCTAT-3' from citation (197) and *Il1b*-FW 5'-GCAACTGTTCCTGAACTCAACT-3', *Il1b*-RV-5'-ATCTTTTGGGGTCCGTCAACT-3'. Cq values were analyzed using the ΔΔCq method (218).

Lactate dehydrogenase (LDH) detection assay

The LDH-Glo Kit (Promega, catalog #J2380) was used to approximate %-cell death based on the abundance of the enzyme lactate dehydrogenase (LDH) in the culture media of cells treated with experimental or control stimuli. This assay works by providing a substrate for oxidation by LDH, which liberates NADH to generate a luciferin that becomes luminescent when activated by the kit's Ultra-Glo reagent. The readout of relative luminescent units (RLU), an approximation of LDH abundance, is used to calculate cell death. To perform the assay, cells were stimulated with the indicated experimental or control stimuli, and then medium samples were collected into cold LDH storage buffer (200mM Tris-HCl pH 7.3, 10% Glycerol, 1% BSA) at a ratio of 1:25 vol/vol. One set of three technical replicate wells was treated with Triton X to induce maximal cell death. Media from 3 cell-free control wells were also collected. Samples were either run immediately or stored at -80°C until ready to use. All samples and reagents were equilibrated to RT before the LDH detection assay was performed. 50 µl of each sample or standard was assayed in duplicate in a white-walled 96-well plate. 50 µl of Detection Enzyme Mix with Reductase Substrate was added to each well and plates were incubated at RT for 1 h. Luminescence was read on the Biotek Synergy HT Microplate Reader (Agilent Winooski, VT). RLU duplicate values were averaged. The %-cell death was calculated as: [(RLU sample – RLU no cell control)/ (RLU max – RLU no cell control)] x 100.

Enzyme-Linked Immunosorbent Assay (ELISA)

IL-1β was measured from cell culture medium samples using the IL-1β Mouse ELISA Kit (Abcam, #ab100704). To assay 100 µl of sample per well in duplicate, media samples were diluted in Assay Diluent B at a 2:1 ratio. Standard curves were generated using recombinant IL-1β supplied in the kit to perform serial dilutions according to the manufacturer's instructions. Serum-free cell culture medium diluted 2:1 in Assay Diluent B was used as the diluent for the curve. The assay was carried out as described in the product manual. Absorbance was read at 450 nm using the Biotek Synergy HT Microplate Reader (Agilent Winooski, VT). IL-1β concentrations were interpolated from the sigmoidal standard curve using GraphPad Prism. To determine concentrations in the experimental samples, the interpolated values were scaled up by the dilution factor.

Measurement of caspase-1 activation by luminescent assay

Caspase-1 activity was measured in cells in culture plates using the Caspase-1-Glo Inflammasome Assay (Promega, catalog #G9951). Macrophages and osteoclasts were cultured for 5 days in black-walled 96-well plates (Greiner, catalog #655090). On the day caspase-1 activity was measured, media were changed. The media volume was replaced so that each well had a total volume of 100 µl with either vehicle control or 500 ng/ml LPS derived from *E. coli* (Invivogen, catalog #tlrl-eblps) added in. Stimulation was carried out for 5 h. The Caspase-1-Glo substrate was prepared by adding the Caspase-1 Buffer to the lyophilized Z-WEHD substrate to create the Glo mixture. Then, the MG-132 inhibitor (inhibits non-specific caspase activity) was added to the reconstituted Z-WEHD substrate (Glo mixture). Just before adding this mixture to the well, nigericin was added to all wells at a final concentration of 15 µM. The Glo mixture was added at 100 µl per well to the 100 µl culture medium already in each well. As a negative control, the caspase-1 inhibitor AcYVAD was added to half of the wells. The plate was incubated for 1 h at RT and then luminescence was measured using the Biotek Synergy HT Microplate Reader (Agilent Winooski, VT).

In vitro infection by gentamicin protection assay

At 2 h before infection, osteoclasts and macrophages were transitioned to serum- and antibiotic-free MEM-α medium supplemented with CMG 14-12 supernatant at a vol/vol ratio of 1:40, with or without RANKL. Bacterial inocula were prepared from AH1263 and adjusted to a concentration of approximately 5 x 10^8 CFU/ml in sterile 1X PBS. For 96-well plates, cell monolayers were infected with *S. aureus* by adding 2.5 x 10^6 CFU in 5 µl per well for a multiplicity of infection (MOI) of 50 or 5.0 x 10^6 CFU in 10 µl for a MOI of 100. For 24-well plates, cell monolayers were infected with *S. aureus* by

adding 1.25 x 10^7 CFU in 25 µl per well for a multiplicity of infection (MOI) of 50 or 2.5 x 10^7 CFU in 50 µl for a MOI of 100. Sterile 1X PBS was added to control wells. Plates were centrifuged at 1000 rpm for 1 min to bring bacteria in contact with the cell monolayers. Plates were incubated for 1 h at 37°C to allow for bacterial internalization. Gentamicin was added directly to the wells for an in-well concentration of 100 µg/ml gentamicin to kill extracellular bacteria. After 1 h of incubation, cell monolayers were washed with warm 1X PBS and media (serum-free MEM-α media containing 1X penicillin-streptomycin with CMG 14-12 supernatant +/- RANKL) were replaced. At the indicated timepoint, media were collected for protein isolation or ELISA and lysates were collected for protein isolation.

Murine model of osteomyelitis

All animal experiments were approved by the Vanderbilt University Institutional Animal Care and Use Committee. Mice underwent induction of post-traumatic osteomyelitis as previously described (22,38,51). Briefly, 7- to 8-week-old mice were anesthetized using 3-3.5% isoflurane for induction and 1-1.5% for maintenance. Mice received subcutaneous injections of sustained-release buprenorphine (0.5-1 mg/kg) prior to the procedure to maintain analgesia for 48 h post-infection. After induction of anesthesia, the left hindlimb and flank were prepared for surgery, and the diaphysis of the femur was exposed using sterile technique. An approximately 1 mm defect was made in one side of the cortical bone using trephination with a 21-gauge needle. An inoculum containing either 1 x 10^5 CFU or 1 x 10^6 CFU of AH1263 in 2 µl sterile 1X PBS was injected into the cortical defect using a micropipette. Muscle fascia and skin were then closed with sutures and the mice were allowed to recover from anesthesia. Mice were monitored and weighed daily until the experimental end point. Mice were monitored for humane endpoint criteria, which included inability to eat or drink, immobility or lethargy, hunched posture, and weight loss greater than 20% body weight occurring after 4 days post-infection. No mice in this study met criteria for humane endpoint euthanasia. At the experimental endpoint, mice were euthanized. If a femur was fractured during extraction, the sample was excluded from imaging analyses.

CFU enumeration

At the desired endpoint post-induction of osteomyelitis, femurs, kidneys, and livers were sterilely dissected from euthanized mice. Femurs or kidneys were singly placed in NAVY bead lysis tubes (Next Advance, Troy, NY) containing 500 µl of sterile 1X PBS. Because of the larger size, livers were split into two bead lysis tubes prior to homogenizing. Tissues were then homogenized at 4°C using a Bullet Blender at the highest setting for 3 intervals of 5 min each. Homogenates were serially diluted in sterile 1X PBS and plated on TSA plates. Plates were incubated overnight at 30°C and CFU were counted

the next day. The limit of detection for this workflow is 1.69 and 1.99 Log_{10} transformed CFU for femurs/kidneys and liver, respectively.

Micro-computed tomography (μCT) of cortical and trabecular bone in femurs

Femurs were dissected from mice at day 14 post-infection, fixed in 10% neutral buffered formalin for 48 h, and then moved to 70% EtOH before storage at 4°C. Fixed femurs were scanned using a μCT50 (Scanco Medical, Switzerland) instrument and analyzed with μCT Tomography V6.3–4 software (Scanco USA, Inc.). Scans were acquired at 10.0 μm voxel size at 70 kV, 200 μA, and an integration time of 350 ms in a 10.24 mm view to result in 1088 image slices. To accommodate analysis of trabecular and cortical bone, a region of interest was selected on each femur to encompass the trabecular bone of the distal metaphysis, as well as the entire diaphysis so that the cortical defect into which bacteria were inoculated could be visualized. The proximal epiphysis was excluded. Cortical bone destruction, callus formation, and trabecular bone volume were determined by contouring the indicated regions of interest as previously described (22,249). Briefly, to analyze cortical bone loss and callus formation, 818 slices were contoured, centered around the midpoint of the defect. For trabecular bone analysis, measurements to the distal trabecular bone were standardized to begin 30 slices above the growth plate. 101 slices total were analyzed.

Bone histology and histomorphometric analysis of osteoclasts in trabecular bone

After imaging by μCT, fixed femurs were decalcified for four days in 20% EDTA pH 7.4 at 4˚C, with a solution change on day 2. Decalcified femurs were processed into paraffin and embedded, then sectioned at 4μm thickness through the infectious nidus and bone marrow cavity using a Leica RM2255 microtome. Sectioned femurs were stained for TRAP with hematoxylin counterstain. Slides containing TRAP-stained histologic sections were then imaged at 10X on a Biotek Cytation 5 Image Reader (Agilent, Winooski, VT). Histomorphometry was performed on the imaged slides using BIOQUANT OSTEO software (BIOQUANT, Nashville TN). The analysis was performed on a region of interest of trabeculae proximal to the growth plate in the distal femur. Guided by ASBMR standards, osteoclast surface and bone surface were calculated to quantify percent osteoclast surface/bone surface (52). The BIOQUANT-defined L2 (bone surface) and L3 (osteoclast surface) arrays were used to quantify bone surface and osteoclast surface respectively.

Statistical analyses

Data were plotted and analyzed using GraphPad Prism software (Version 9). For all experiments, data were checked for normality prior to statistical analysis using either the D'Agostino-Pearson test or the Shapiro-Wilk test. For ELISA results, a two-way ANOVA was used to assess the relative contribution of treatment versus cell type or genotype to data variation. A post hoc Sidak's multiple comparisons test was used to make specific comparisons between groups, usually comparing osteoclasts to macrophages. In comparisons of only two groups, including the qRT-PCR experiments, data were compared by an unpaired parametric t-test. When comparing two groups of mice, such as when cortical bone destruction, callus formation, or osteoclast abundance were being compared between WT and knockout, an unpaired t-test or non-parametric Mann Whitney test was used, depending on data normality and sample size. When comparing weight loss over infection time course between WT and knockout mice, multiple t-tests with correction for multiple comparisons were used. When comparing organ and femur CFU burdens between genotypes, multiple Mann-Whitney tests were used with correction for multiple comparisons. This was chosen because of the potential relationship between infected femur burdens and bacterial dissemination to other organs.

Results

Osteoclast differentiation alters transcriptional response to *S. aureus* supernatant

To begin to understand how osteoclast differentiation alters the cellular response to *S. aureus*, we first examined how osteoclasts at different stages of osteoclastogenesis differentially alter gene expression in response to staphylococcal stimuli. Toward this goal, we first confirmed that the culture conditions in 24-well plates were sufficient to generate osteoclasts in the early and advanced stages of osteoclastogenesis. To do this, bone marrow-derived monocytes (BMDMs) were cultured in CMG 14-12 supernatant and 35 ng/ml RANKL for 2 or 7 days. Macrophage comparators were cultured in parallel. qRT-PCR was utilized to measure the expression of genes that are activated as part of RANK-induced transcriptional reprogramming, including the master osteoclast-identity transcription factor nuclear factor of activated T cells cytoplasmic 1 (*Nfatc1*), the co-receptor osteoclast-associated receptor (*Oscar*), and the bone-resorptive protease cathepsin K (*Ctsk*). For each gene, expression in RANKL-exposed cells was normalized to macrophage controls which do not express high levels of osteoclast marker genes (**Fig. 19A-D**). Mature osteoclasts had significantly greater relative expression of *Ctsk*

and *Oscar* compared to pre-osteoclasts. These results show that the increasing duration of RANKL exposure (2 day versus 7 days) results in increased expression of osteoclastogenic genes.

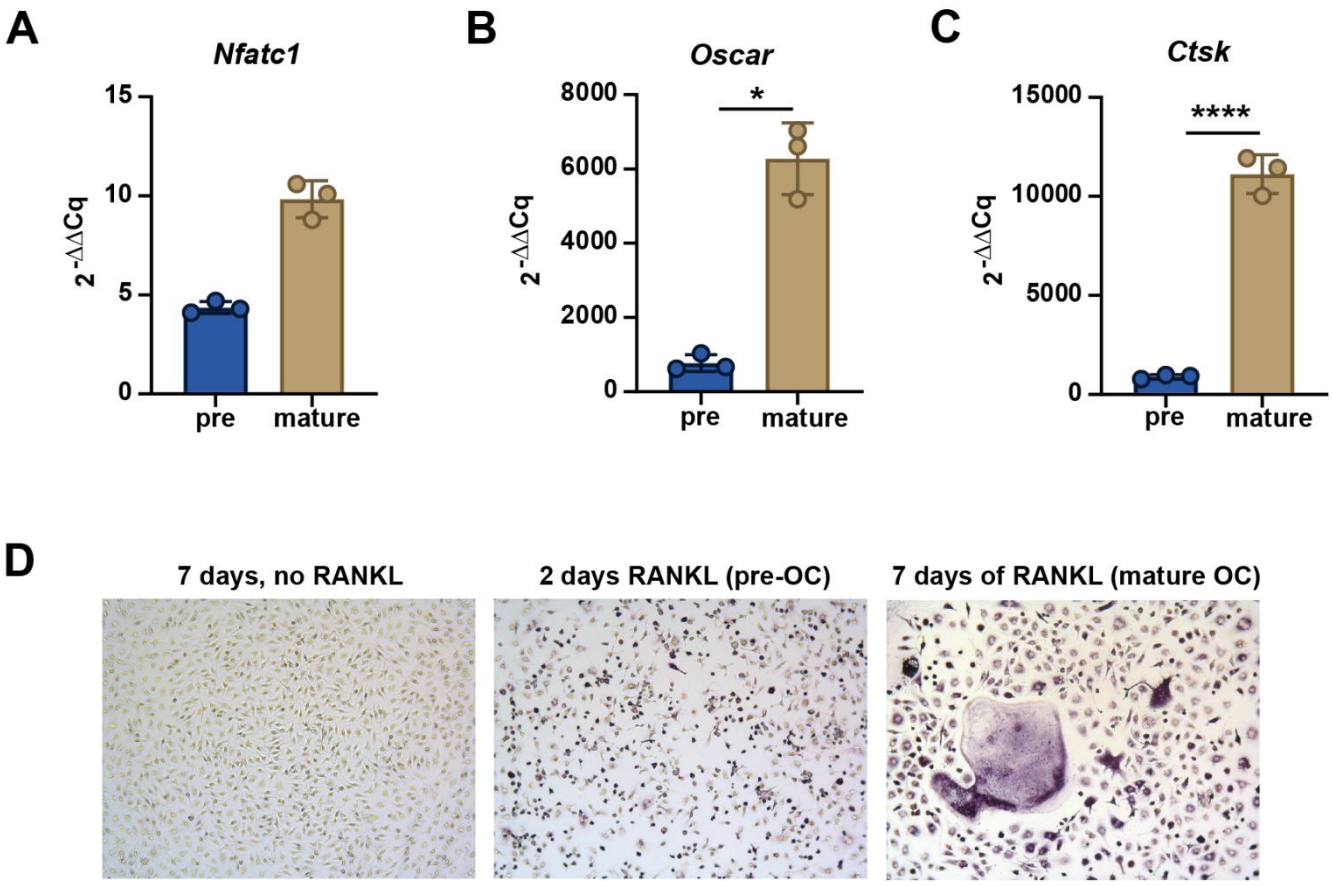

Figure 19. Increasing duration of RANKL treatment increases transcription of osteoclast identity genes. A-C) Whole bone marrow cells were isolated from 8–12-week-old C57BL/6J mice and differentiated into bone marrow-derived monocytes (BMDMs) using CMG 14-12 supernatant as an M-CSF source. BMDMs were then cultured with CMG 14-12 supernatant and 35 ng/ml RANKL for either 2 or 7 days to generate pre-osteoclasts and mature osteoclasts. A comparator population of macrophages was generated in parallel, and those cells received CMG 14-12 supernatant only for 2 or 7 days. Cells were collected for RNA isolation and qRT-PCR was performed. The ΔCq method was used to compute transcriptional changes to *Nfatc1* **(A)**, *Oscar* **(B)**, and *Ctsk* **(C)**. For each gene, expression of RANKL-stimulated cells was normalized to the macrophage comparator. Comparisons were made between ΔΔCq values of 2- and 7-day RANKL-treated cells using a t-test, *p < 0.05 ****p < 0.0001. If no asterisk is denoted, then the comparison was not statistically significant. The $2^{-\Delta\Delta Cq}$ value represents the fold-change induction of expression as normalized to the appropriate macrophage comparator. **D)** A separate plate of cells was fixed and stained for tartrate-resistant acid phosphatase (TRAP) to identify osteoclasts. Representative images were taken using a 10X objective at the indicated timepoint with or without RANKL.

We next tested how pre- and mature osteoclasts alter gene expression in response to *S. aureus* supernatant. To do this, pre- and mature osteoclasts and macrophage comparators were stimulated for 6 h with supernatant prepared from the Δ*psmα1-4* strain of *S. aureus* or a RPMI medium control. Gene expression was measured using the NanoString nCounter System to measure transcript abundance of a pre-defined panel of immunology-related genes. Genes that were differentially expressed upon stimulation with *S. aureus* supernatant were identified. These results showed that differentiating osteoclasts did not differentially express any of the measured genes, whereas the 2-day macrophage comparators had 8 significantly differentially expressed genes (**Fig. 20A-B**). 7-day macrophages showed the greatest transcriptional changes in response to stimulation with *S. aureus* supernatant (**Fig. 20C**). Mature osteoclasts also differentially expressed a variety of genes including transcripts related to cytokine signaling and neutrophil recruitment (**Fig. 20D**). The *Il1b* transcript was significantly upregulated in 2- and 7-day macrophages and mature osteoclasts responding to *S. aureus* supernatant. These results show that while osteoclast differentiation does change cellular response to *S. aureus* supernatants, the ability to upregulate *Il1b* is preserved. This finding led us to hypothesize that osteoclasts prime an IL-1β-activating inflammasome in response to bacterial stimulation.

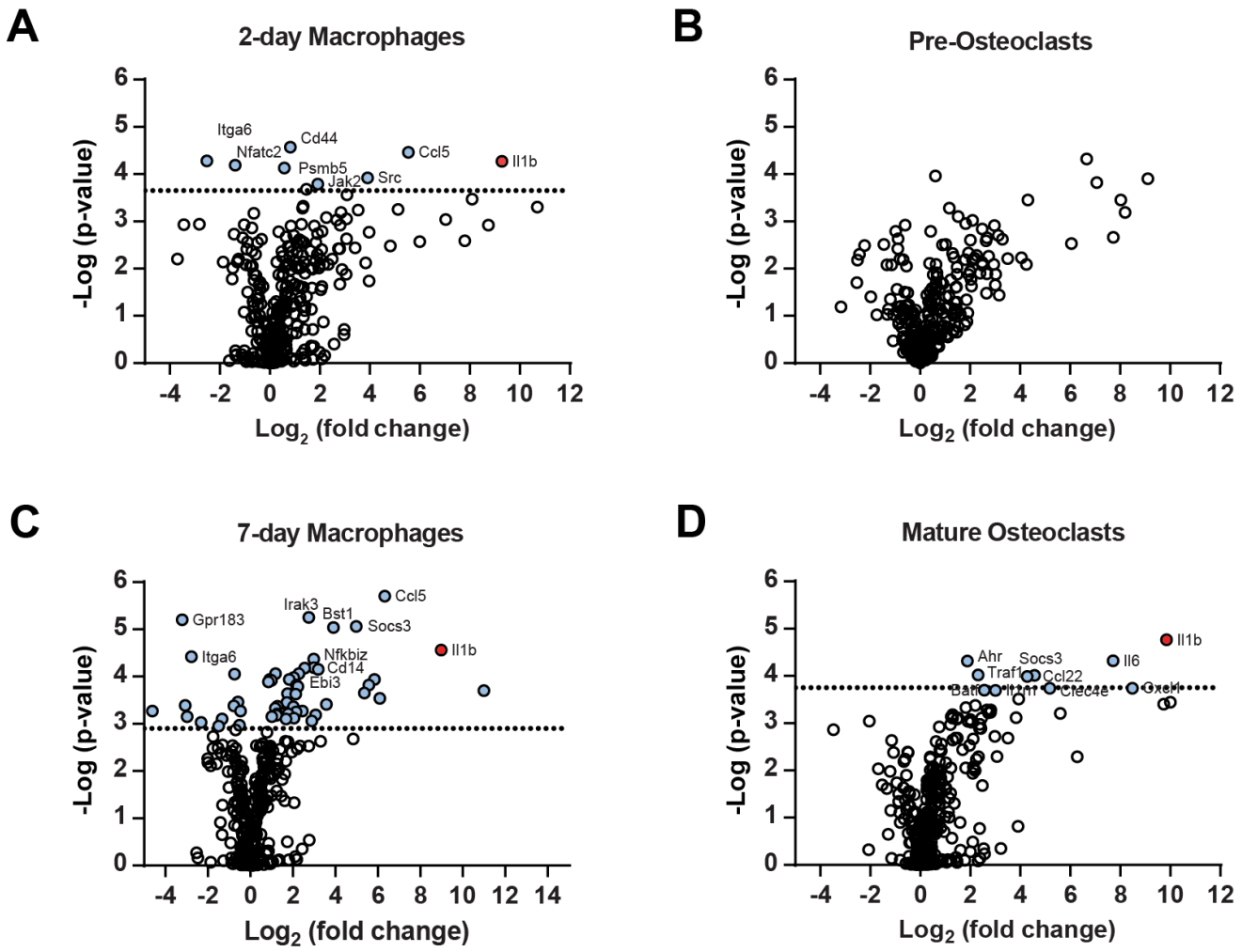

Figure 20. Osteoclast differentiation alters transcriptional response to *S. aureus* supernatant. Whole bone marrow cells were isolated from 8–12-week-old C57BL/6J mice and differentiated into bone marrow-derived monocytes (BMDMs) using CMG 14-12 supernatant as an M-CSF source. BMDMs were cultured with CMG 14-12 supernatant (macrophages) or 35 ng/ml RANKL + CMG 14-12 supernatant (pre- or mature osteoclasts) for 2 days **(A-B)** or 7 days **(C-D).** Cells were stimulated for 6 h with 5% vol/vol of concentrated Δ*psmα1-4* supernatant or RPMI control. Transcript abundance of immunology-related genes was measured using the NanoString nCounter System. Differential expression was calculated using the nSolver Advanced Analysis Software. The Benjamini-Yekutieli correction was applied to adjust p-values for multiple comparisons. Dotted lines indicate the adjusted p-value above which *p ≤ 0.05. Significantly differentially expressed genes are marked in blue. The significantly upregulated *Il1b* gene is marked in red. For each cell type, the top 10 most significantly differentially expressed genes are labeled with the gene name. Each data point is compiled from three independent cell culture experiments for n = 3 biological replicates.

LPS and *S. aureus* supernatants prime the osteoclast inflammasome

To determine whether osteoclasts can activate the inflammasome, we first tested whether NLRP3 inflammasome priming could be induced in osteoclasts. We measured changes to gene transcription and protein abundance in response to either lipopolysaccharide (LPS), a canonical NLRP3 priming agent, or supernatant prepared from *S. aureus* culture. Pre-osteoclasts (2 days of culture) and mature osteoclasts (5 days of culture) were cultured alongside macrophage comparators. Cells were then stimulated with either LPS, supernatant prepared from Δ*psmα1-4* strain of *S. aureus*, or the relevant vehicle control. After 4 h of stimulation, cell lysates were collected for measurement of gene expression by qRT-PCR and for protein detection by immunoblot. qRT-PCR revealed that mature osteoclasts and macrophage comparators both upregulated the *Nlrp3* gene in response to LPS and, to a lesser extent, in response to *S. aureus* supernatant (**Fig. 21A**). *Il1b* transcription was also elevated in mature osteoclasts and macrophage comparators responding to LPS or *S. aureus* supernatant (**Fig. 21B**). However, the increase in *Il1b* transcription was significantly greater in macrophages compared to osteoclasts for both LPS and *S. aureus* supernatant stimulation. Priming was also assessed by detecting changes in the levels of proteins involved in inflammasome activation and assembly, including Toll-like receptor 2 (TLR2), which can facilitate priming, as well as pro-caspase-1, which contains the catalytic activity necessary for protein cleavage, and the caspase-1-substrates pro-IL-1β and pro-gasdermin D. Immunoblotting showed that both pre- and mature osteoclasts and macrophage comparators harbored detectable levels of TLR2, pro-gasdermin D, and pro-caspase-1, regardless of stimulation (**Fig. 22A-B**). LPS stimulation increased levels of TLR2 and pro-IL-1β in pre and mature osteoclasts and in macrophages. This difference was quantified by measuring the fluorescence intensity of the protein bands **(Fig. 22C).** Stimulation with Δ*psmα1-4* supernatant increased levels of TLR2, pro-caspase-1, and pro-IL-1β in macrophages. Pre- and mature osteoclasts increased abundance of pro-IL-1β in response to Δ*psmα1-4* supernatants, but the magnitude of increase was lower than in macrophages (**Fig**. **22C**). Stimulation with LPS or *S. aureus* supernatant did not change pro-gasdermin levels in macrophages or osteoclasts. Notably, both pre- and mature osteoclasts had stronger pro-gasdermin D bands than macrophages at baseline. Overall, the immunoblot results show that both LPS and *S. aureus* supernatant induce priming in osteoclasts based on accumulation of proteins involved in inflammasome activation. When considered alongside the gene expression data, these results suggest that osteoclasts and macrophages undergo transcriptional and translational priming in response to LPS. Staphylococcal supernatants are weaker priming agents for osteoclasts, in comparison to macrophages.

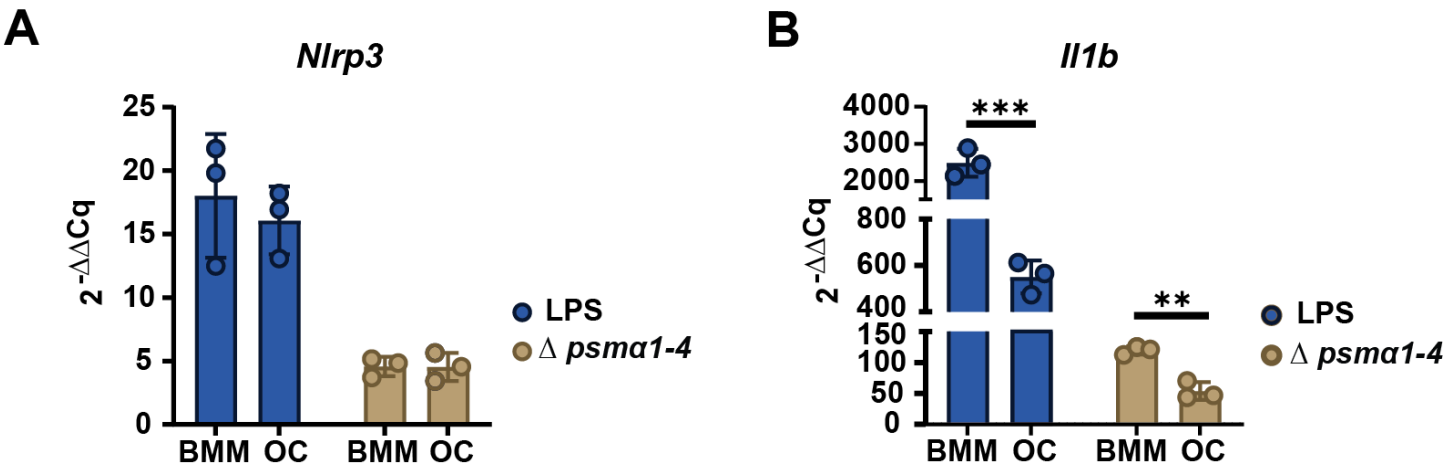

Figure 21. Osteoclasts undergo transcriptional priming in response to LPS and *S. aureus* supernatant. A-B) Whole bone marrow cells were isolated from 8–12-week-old female C57BL/6J mice and differentiated into bone marrow-derived monocytes (BMDMs) using CMG 14-12 supernatant as an M-CSF source. BMDMs were cultured with CMG 14-12 supernatant (macrophages, abbreviated as BMM) or 100 ng/ml RANKL + CMG 14-12 supernatant (osteoclasts, abbreviated as OC) for 5 days. Cells were transitioned to serum-free media and stimulated with either 500 ng/ml LPS, 10% vol/vol unconcentrated supernatant from the Δ*psmα1-4* strain of *S. aureus*, or the relevant vehicle control. After 4 h of stimulation, cell lysates were collected for RNA extraction. Transcripts for the *Nlrp3* and *Il1b* genes were measured by qRT-PCR. The y axis, $2^{-\Delta\Delta Cq}$, represents the fold-change induction of transcription in response to LPS or supernatant, normalized to relevant vehicle control. ΔΔCq values were compared between cell types using an unpaired t-test, **p = 0.0055 and ***p = 0.0002. If not denoted with asterisks, statistical difference between cell types was not statistically significant. Error is plotted as standard deviation and n = 3 technical replicates per group.

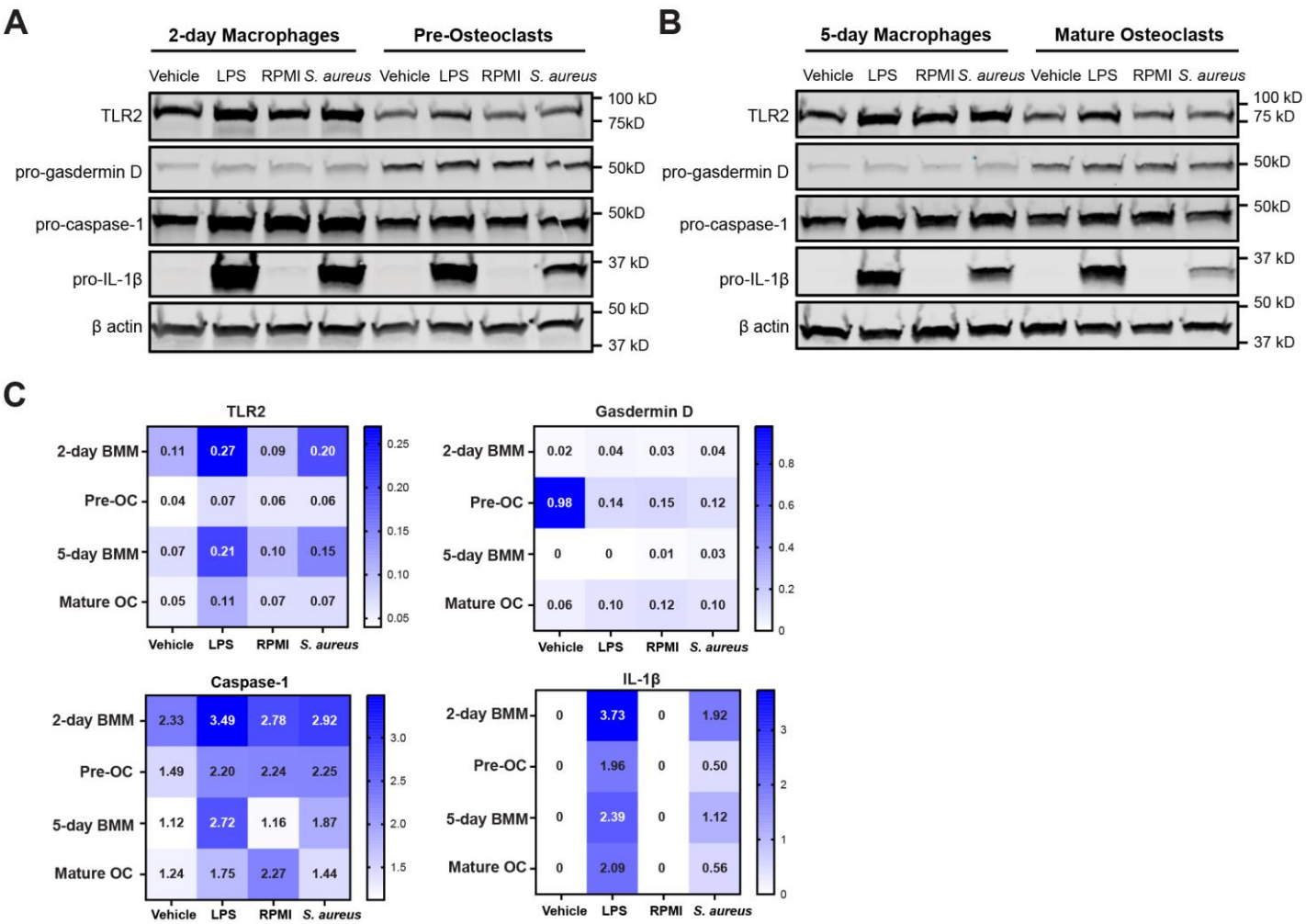

Figure 22: Osteoclast differentiation reduces inflammasome priming in response to *S. aureus* supernatants, while priming in response to LPS is maintained. A-C) Whole bone marrow cells were isolated from 8–12-week-old female C57BL/6J mice and differentiated into bone marrow-derived monocytes (BMDMs) using CMG 14-12 supernatant as an M-CSF source. BMDMs were cultured with CMG 14-12 supernatant (macrophages) or 100 ng/ml RANKL + CMG 14-12 supernatant (osteoclasts) for 2 days **(A, C)** or 5 days **(B, C).** Cells were transitioned to serum-free media and stimulated with either 500 ng/ml LPS, 10% vol/vol unconcentrated supernatant from the Δ*psmα1-4* strain of *S. aureus*, or the relevant vehicle control. After 4 h of stimulation, cell lysates were collected for immunoblot. β actin served as the loading control. Fluorescence intensity of the protein bands was measured using Image Studio (Li-Cor). The intensity values of each protein target were normalized to the loading control by dividing FI_{target} / $FI_{\beta\ actin}$ for each sample. The resulting values are displayed by protein target in the heatmaps shown **(C)**.

Osteoclasts activate a caspase-1-associated inflammasome in response to LPS

To understand whether osteoclast inflammasome priming by LPS or *S. aureus* supernatant is sufficient for inflammasome activation, we next measured IL-1β release into the cell culture media using ELISA. Osteoclasts released IL-1β in response to the canonical NLRP3-activating stimuli LPS + nigericin, though at a diminished magnitude compared to macrophages (**Fig. 23**). Macrophages, but not osteoclasts, release IL-1β when exposed to *S. aureus* Δ*psmα1-4* supernatant followed by nigericin, suggesting that *S. aureus* supernatants are sufficient to prime the macrophage but not the osteoclast inflammasome. No IL-1β release was observed in response to *S. aureus* supernatant alone or in response to either vehicle control (water or RPMI medium plus nigericin).

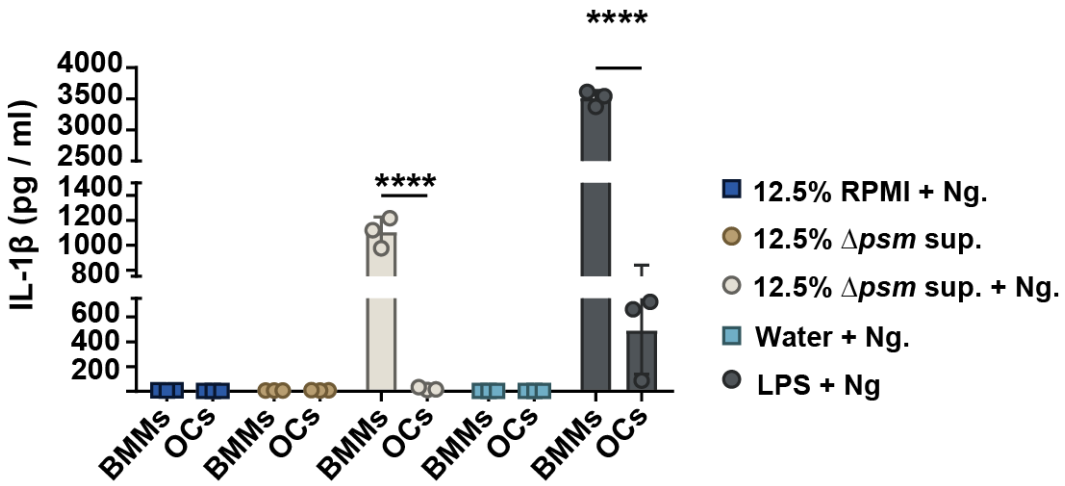

Figure 23. Osteoclasts release IL-1β in response to priming with canonical stimuli, but not *S. aureus* supernatant. Whole bone marrow cells were isolated from 8–12-week-old female C57BL/6J mice and differentiated into bone marrow-derived monocytes (BMDMs) using CMG 14-12 supernatant as an M-CSF source. BMDMs were cultured with CMG 14-12 supernatant (macrophages) or 35 ng/ml RANKL + CMG 14-12 supernatant (osteoclasts) for 5 days. Cells were transitioned to serum-free media and the following stimuli were added: 500 ng/ml LPS or equivalent amount of water, 12.5% vol/vol concentrated Δ*psmα1-4* supernatant or equivalent amount of RPMI vehicle. After 3 h, 15uM nigericin (Ng) was added. 30 min later, cell culture media were collected. IL-1β concentrations were measured from media samples using ELISA. Results were analyzed by 2-way ANOVA, ****p < 0.0001 for cell type, treatment, and interaction. Sidak's multiple comparisons test was used to compare between cell types, ****p<0.0001. If not denoted with asterisks, statistical difference between cell types was not statistically significant. The lower limit of detection is 3.99 pg/ml in this assay. Error is plotted as ± standard deviation and n = 3 technical replicates per group. Results are representative of two independent biological replicate experiments.

After confirming that IL-1β release occurs in osteoclasts stimulated with LPS followed by nigericin, we next examined whether cytokine release coincides with the proteolytic cleavage and activation of pro-caspase-1, pro-gasdermin D, and pro-IL-1β. We measured these proteins in the lysates and supernatants of osteoclasts and macrophages cultured for 5 days and then stimulated with 4 h of LPS to prime the inflammasome, followed by 30 or 60 min of nigericin treatment. Both macrophages and osteoclasts cleaved pro-gasdermin D into its N-terminal form and this was visible in the cell lysates (**Fig. 24**). However, osteoclasts maintained an abundance of pro-gasdermin D, even after the cleaved, p31, N-terminal form appeared, suggesting that regulatory mechanisms may prevent or slow down its cleavage. A similar trend was observed for caspase-1, which was cleaved into its p20 form and released into the cell supernatant by both osteoclasts and macrophages, but remained abundant in the pro form in osteoclast lysates only. Both macrophages and osteoclasts released cleaved IL-1β into the culture medium, confirming that the inflammasome fulfills its cytokine-activating function in osteoclasts. Measured values of cleaved proteins revealed that macrophages cleaved and released over twice as much caspase-1 and IL-1β as osteoclasts (**Table 6**). Thus, osteoclast differentiation still allows activation of an IL-1β-cleaving inflammasome in response to LPS + nigericin, but the inflammasome is not as active in osteoclasts as it is in macrophages.

To confirm that IL-1β activation was consistent with canonical activation of caspase-1 through NLRP3, we also performed an ELISA to measure IL-1β release in WT and caspase-1- and caspase-11-deficient (*Casp1/11*$^{-/-}$) macrophages and osteoclasts. For both macrophages and osteoclasts, WT cells had significantly greater IL-1β release than *Casp1/11*$^{-/-}$ cells (**Fig. 25 A-B**). To better understand the differences in caspase-1 activation in osteoclasts compared to macrophages, we used a luminescent assay to measure caspase-1 catalytic activity in response to LPS and nigericin. This assay revealed that both macrophages and osteoclasts had significant caspase-1 activation in response to LPS + nigericin compared to the respective negative control (caspase-1 inhibition via AcYVAD) (**Fig. 25 C-D**). In terms of magnitude, caspase-1 activation was about three times greater in macrophages compared to osteoclasts. Taken together, the results from figures 24 and 25 demonstrate that osteoclasts can engage a caspase-1-associated inflammasome in response to LPS and nigericin. The amount of IL-1β cleaved by osteoclasts is significantly less than the amount cleaved by macrophages, and this is concordant with the levels activated caspase-1 and cleaved gasdermin D. Thus, these results suggest that osteoclast differentiation may induce negative regulatory mechanisms that dampen the inflammasome.

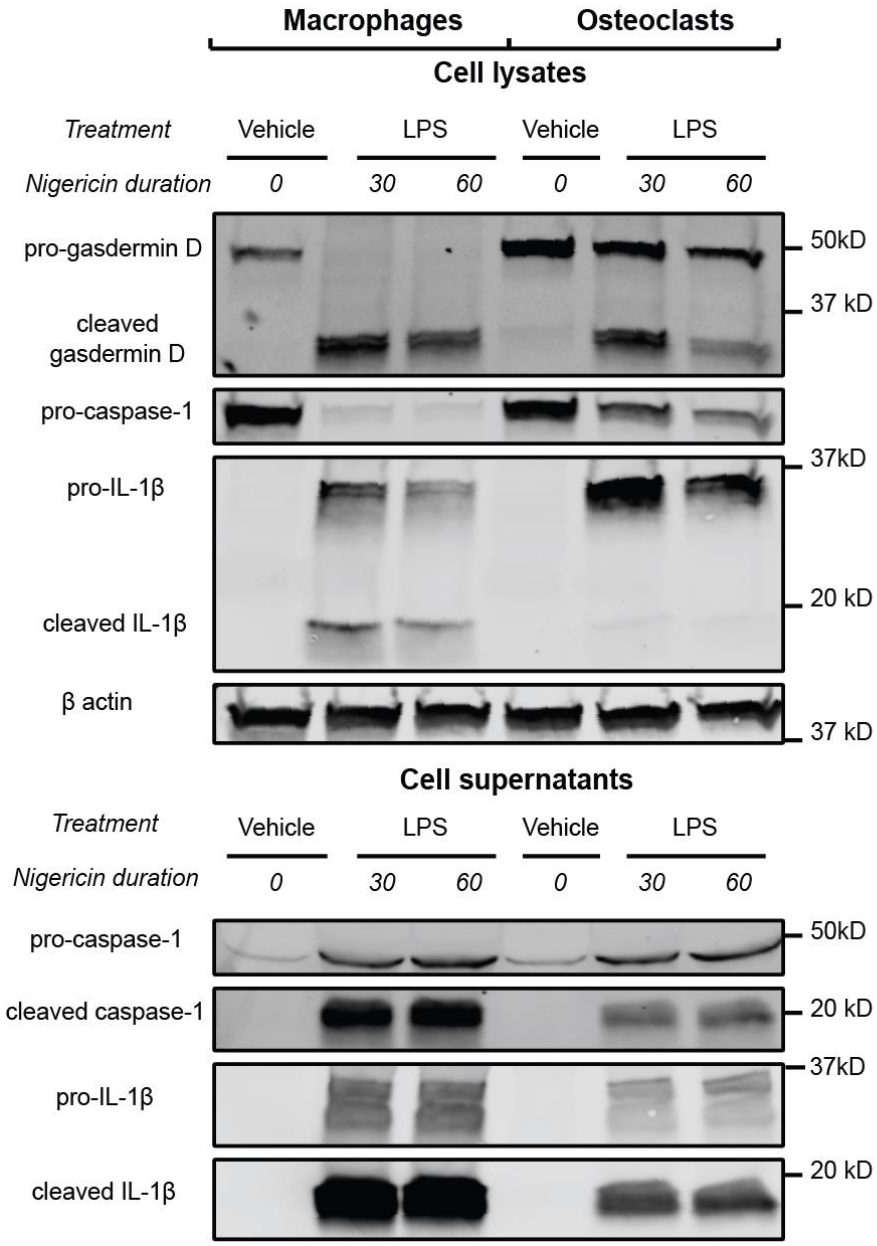

Figure 24. LPS + nigericin activate caspase-1-associated IL-1β processing in osteoclasts. A) Whole bone marrow cells were isolated from 8–12-week-old male C57BL/6J mice and differentiated into bone marrow-derived monocytes (BMDMs) using CMG 14-12 supernatant as an M-CSF source. BMDMs were cultured with CMG 14-12 supernatant (macrophages) or 100 ng/ml RANKL + CMG 14-12 supernatant (osteoclasts) for 5 days. Cells were then placed in serum-free media and stimulated with 500 ng/ml LPS or equivalent amount of water. Following 4 h of priming, LPS-treated cells were stimulated with 15 uM nigericin for either 30 or 60 min. Cell lysates and supernatants were collected for protein extraction. Cell supernatant samples were TCA-purified prior to use. Protein targets were identified by immunoblot. Results are representative of two independent experiments with one replicate experiment shown.

Table 6. Fluorescence intensity (FI) of protein bands from Figure 24. reveals the relative levels of substrate cleavage in osteoclasts compared to macrophages.

OC – osteoclast

BMM – macrophage

Ng. – nigericin

FI values were measured and used to calculate the ratio as indicated in column 3.

For cleaved:pro, $FI_{cleaved} / FI_{pro}$ results in an estimate of how much of the pro substrate remains following LPS + 30 or 60 min nigericin. A low ratio indicates that pro-protein has been left inactivated.

For BMM:OC, FI_{BMM} / FI_{OC} results in an estimate of how much protein cleavage was executed in macrophages compared to osteoclasts. A higher number represents greater cleavage by macrophages.

Target	Type	Comparison	LPS + 30 min Ng. BMM	LPS + 60 min Ng. BMM	LPS + 30 min Ng. OC	LPS + 60 min Ng. OC
IL-1β	Lysate	Cleaved: pro	0.81	1.08	0.01	0.32
Gasdermin D	Lysate	Cleaved: pro	223.24	18.14	0.98	0.84
Target	**Type**	**Comparison**	**LPS + Ng. 30 min**	**LPS + Ng. 60 min**		
cleaved IL-1β	Sup	BMM: OC	2.20	2.45		
cleaved casp1	Sup	BMM: OC	2.32	2.36		

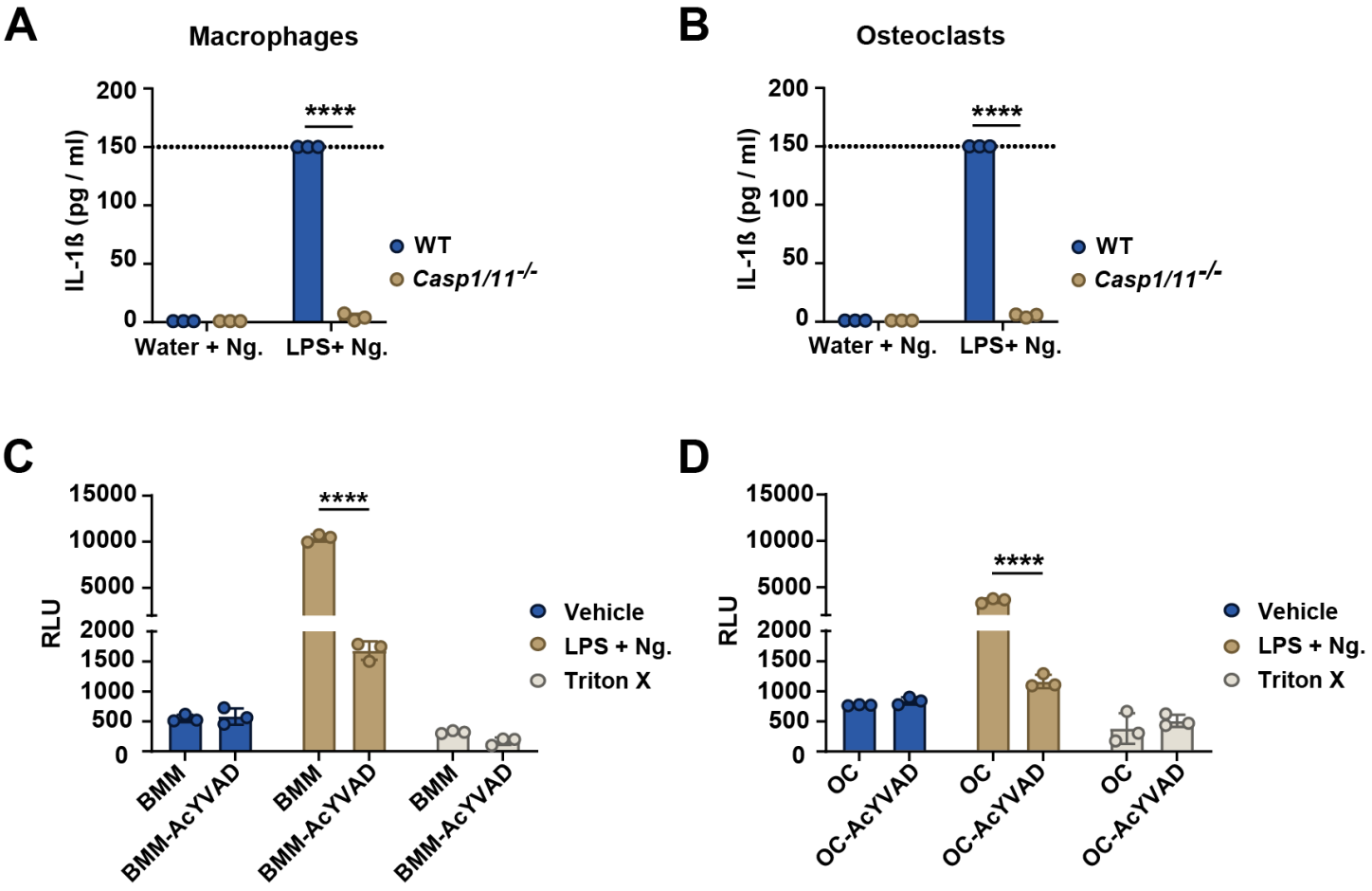

Figure 25. Activation of caspase-1/11 drives IL-1β release in osteoclasts responding to LPS + nigericin. A-B) Whole bone marrow cells were isolated from 8–12-week-old female WT C57BL/6J or *Casp1/11*$^{-/-}$ mice. Cells were differentiated into bone marrow-derived monocytes (BMDMs) using CMG 14-12 supernatant as an M-CSF source. BMDMs were cultured with CMG 14-12 supernatant (macrophages) or 35 ng/ml RANKL + CMG 14-12 supernatant (osteoclasts) for 5 days. Cells were primed with LPS for 3 h followed by treatment with 15μM nigericin (Ng.) for 30 min. Cell culture supernatants were then collected for measurement of IL-1β by ELISA. IL-1β concentrations were evaluated by a two-way ANOVA with Sidak's multiple comparison's test to assess differences between WT and *Casp1/11*$^{-/-}$ macrophages or osteoclasts for each treatment, ****$p < 0.0001$. If not denoted with asterisks, statistical difference between cell types was not statistically significant. Error is represented as standard deviation and there are n = 3 technical replicates per group. The detection maximum for this assay is denoted by the dotted line at y = 150. **C-D)** Whole bone marrow cells were isolated from 8–12-week-old female WT C57BL/6J mice and were differentiated into BMDMs using CMG 14-12 supernatant as an M-CSF source. BMDMs were cultured with CMG 14-12 supernatant (macrophages) or 35 ng/ml RANKL + CMG 14-12 supernatant (osteoclasts) for 5 days. Cells were then primed with LPS or vehicle control for 5 h. The cells were then treated with 15 μM Ng. with or without AcYVAD caspase inhibitor. Triton X served as a negative control. The Caspase-1-Glo Inflammasome Assay was used to measure caspase-1 activation. Relative luminescence units (RLU) serve as a proxy for caspase-1 activity. RLU measurements were compared between groups using a two-way ANOVA with Sidak's multiple comparisons test to compare between caspase inhibitor and no inhibitor, ****$p < 0.0001$. If no asterisk is shown, comparison was not statistically significant. Error is represented as standard deviation and n = 3 technical replicates per group.

Osteoclast inflammasome activation is restricted during *S. aureus* infection

The studies using LPS as a priming agent indicate that osteoclasts have the capacity to activate an IL-1β-cleaving inflammasome. We next sought to determine whether inflammasome activation occurs in osteoclasts responding to intracellular infection with *S. aureus*. We first infected mature osteoclasts and comparator macrophages with *S. aureus* and measured IL-1β release into the media at 2 and 24 h post-infection. At the early timepoint, no IL-1β release was measured from either cell type (**Fig. 26A**). By the later timepoint, macrophages released IL-1β in response to a multiplicity of infection (MOI) of 50 and 100, which was significantly greater than the amount released by osteoclasts (**Fig. 26B**). To better understand how osteoclasts were affected by infection with *S. aureus*, we also measured cell death in infected cells. Osteoclasts incurred significant cell death at both the 50 and 100 MOI of infection, compared to the vehicle control (**Fig. 26C**). Macrophages incurred less cell death than osteoclasts, with a significant difference detected only between the cells infected at an MOI of 100 and the vehicle-treated cells. Time-lapse imaging studies indicated that large, multinucleated osteoclasts were incurring cell death upon infection, and this was visible by 8 h post-inoculation (**Fig. 26 D**).

Because osteoclast priming was relatively lower upon stimulation with *S. aureus* supernatant compared to LPS, we questioned whether stimulation with *S. aureus* could be inhibitory to inflammasome activation in osteoclasts. To test this, macrophages and osteoclasts were infected with *S. aureus* or a vehicle control at an MOI of 50 or 100. After 24 h of infection, one set of macrophages and osteoclasts infected at an MOI of 100 was exposed to 15 μM nigericin for 30 min to test if inflammasome induction could be potentiated by potassium efflux-inducing stimuli. We expected that if the inflammasome was inhibited, then no activation would occur. In macrophages, 15 μM nigericin increased cleavage of IL-1β and caspase-1 in the cell supernatants, compared to the MOI of 100 infection alone (**Fig. 27**). Osteoclasts had very faint IL-1β and caspase-1 cleavage bands in the cell supernatant when infected at an MOI of 100. This was boosted by nigericin, suggesting that infected osteoclasts remain responsive to inflammasome activation via potassium efflux. Importantly, a set of vehicle-treated cells was also exposed to nigericin and no evidence of inflammasome activation was found in either macrophages or osteoclasts (**data not shown**).

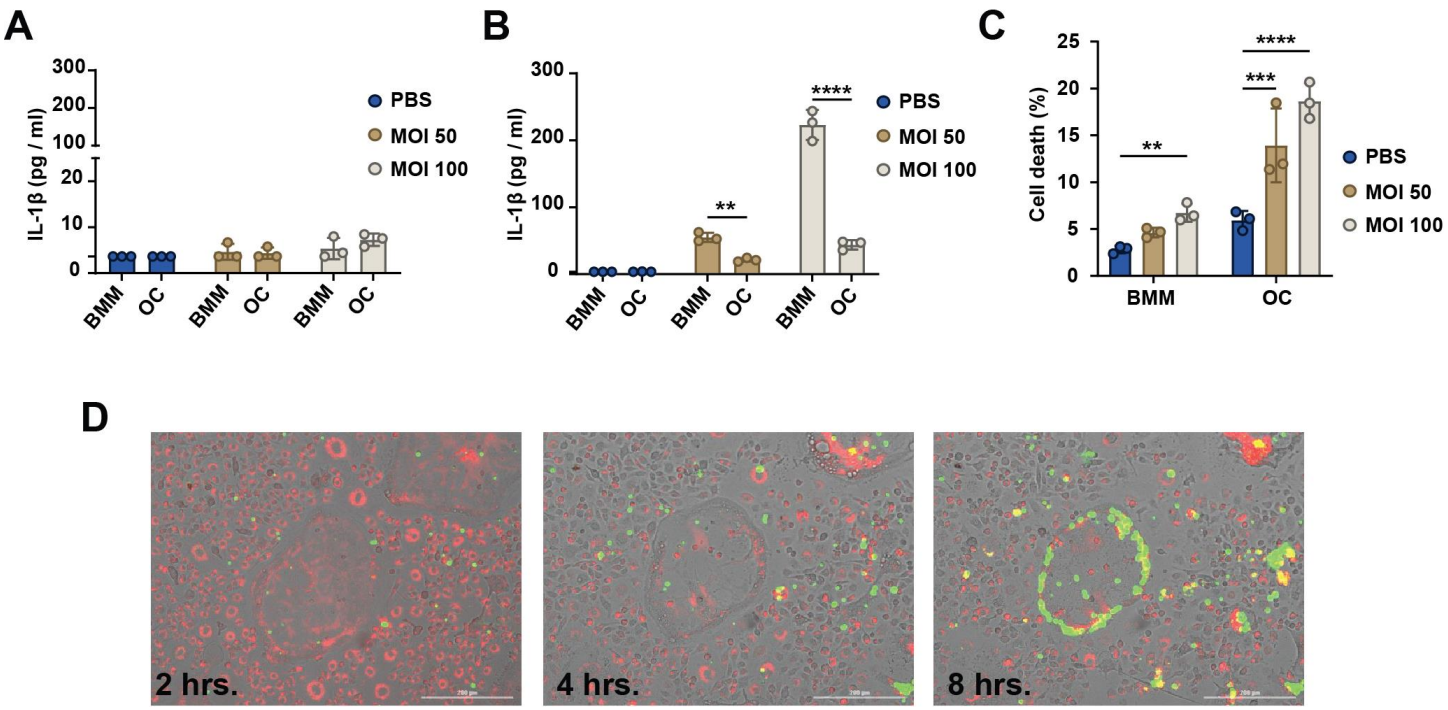

Figure 26. Osteoclasts undergo cell death in response to *S. aureus* infection without significant parallel IL-1β release. A-C) Whole bone marrow cells were isolated from 8–12-week-old male C57BL/6J mice and differentiated into bone marrow-derived monocytes (BMDMs) using CMG 14-12 supernatant as an M-CSF source. BMDMs were cultured with CMG 14-12 supernatant (macrophages, abbreviated as BMM) or 35 ng/ml RANKL + CMG 14-12 supernatant (osteoclasts, abbreviated as OC) for 5 days. Cells were infected with the indicated multiplicity of infection (MOI) of *S. aureus* via gentamicin protection. **A)** Cell culture media samples were collected immediately following the gentamicin incubation, comprising the 2 h post-inoculation timepoint. IL-1β levels were measured from the cell culture media by ELISA. Measurements were compared by 2-way ANOVA. No significant differences were detected. Error is plotted as standard deviation and n= 3 technical replicates per group. **B)** Cell culture media samples were collected at 24 h post-inoculation. IL-1β levels were measured from the cell culture media by ELISA. Measurements were compared by 2-way ANOVA, and Sidak's multiple comparisons test was used to compare between BMM and OC, **p 0.01, ****p < 0.0001. Error is plotted as standard deviation and n= 3 technical replicates per group. **C)** Cell culture media samples were collected at 24 h post-inoculation for measurement of lactate dehydrogenase (LDH) to approximate cell death. LDH measurements were normalized to Triton X-treated control cells, representing 100% cell death. Cytotoxicity was then assessed by 2-way ANOVA. Sidak's multiple comparisons test was used to compare between MOI and vehicle for each cell type, *p < 0.05, ***p < 0.0005, ****p < 0.0001. For each condition, n = 3 technical replicates. **D)** Osteoclasts were cultured for 5 days. Cells were infected at an MOI of 50 with a strain of *S. aureus* that constitutively expresses the mCherry reporter (red). Bacteria were internalized for 1 h followed by 1 h of gentamicin treatment. At this point, the media were changed and Sytox dye was added to the wells (green) to stain the nuclei of dead cells. Cells were imaged on the Biotek Cytation 5 Imaging Reader every 30 min over 22 h. Select images are shown from the 2-, 4-, and 8-h timepoints.

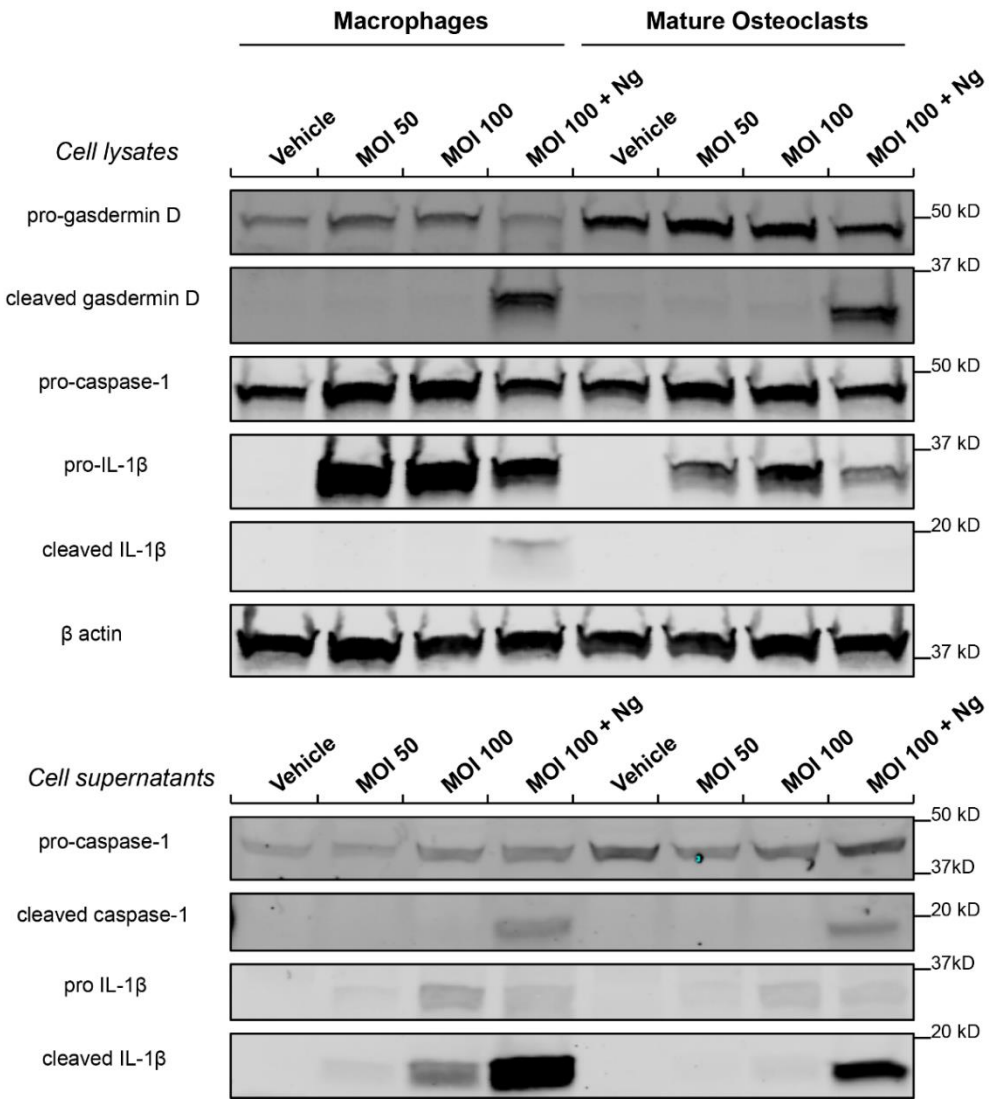

Figure 27. *S. aureus* infection induces caspase-1 and IL-1β cleavage in osteoclasts following exposure to the ionophore nigericin. Whole bone marrow cells were isolated from 8–12-week-old female C57BL/6J mice and differentiated into bone marrow-derived monocytes (BMDMs) using CMG 14-12 supernatant as an M-CSF source. BMDMs were cultured with CMG 14-12 supernatant (macrophages) or 35 ng/ml RANKL + CMG 14-12 supernatant (mature osteoclasts) for 5 days. Cells were placed in serum-free, antibiotic-free media and infected with the indicated multiplicity of infection (MOI) of *S. aureus* (USA 300 LAC) for 1 h. Gentamicin (100 µg/ml) was then added to the media and incubated for 1 h to kill extracellular bacteria. Media were then changed. At the 24 h post-infection timepoint, 15uM nigericin (Ng) was added to the indicated conditions and incubated for 30 min. All cell lysates and supernatants were subsequently collected for protein extraction. Cell supernatant samples were TCA-purified prior to use. The indicated pro and cleaved proteins of interest were detected by immunoblot. β actin served as the loading control.

IL-1β drives osteoclast-associated bone loss in *S. aureus* osteomyelitis

The first part of Chapter III focused on understanding how osteoclast differentiation impacts inflammasome activation. In this section, we examine how inflammasome activation influences bone homeostasis in a mouse model of post-traumatic *S. aureus* osteomyelitis. We seek to identify the upstream regulators of IL-1β activation that govern bone homeostasis and bone loss during infection. We have previously found that IL-1R1-deficient mice lose less trabecular bone during *S. aureus* osteomyelitis (51). These mice also have less trabecular osteoclastogenesis in response to infection, compared to WT mice, while sustaining greater callus formation on the cortical bone (51). To follow up on these findings, we first interrogated the relative contributions of IL-1α versus IL-1β to infection-induced cortical bone destruction, callus formation, and infection-induced trabecular bone loss. We tested this by inducing *S. aureus* osteomyelitis in *Il1b*$^{-/-}$, *Il1a*$^{-/-}$, and WT mice. We found that *Il1a*$^{-/-}$ mice had no changes to cortical bone destruction or callus formation compared to WT (**Fig. 28A-B**). Additionally, while there was a trend toward lower %-bone volume / total volume in the trabecular bone of *Il1a*$^{-/-}$ mice, there was no significant difference compared to WT (**Fig. 28C**). *Il1b*$^{-/-}$ mice had no changes in cortical bone destruction compared to WT mice (**Fig 29A**). However, IL-1β-deficiency resulted in a significant decrease in callus formation compared to WT (**Fig. 29B**). *Il1b*$^{-/-}$ mice also had greater trabecular bone volume compared to WT mice (**Fig 29C**). Thus, we next performed histomorphometry to assess how IL-1β-deficiency affects the increase in trabecular osteoclastogenesis that normally occurs in response to *S. aureus* osteomyelitis. We found a significant decrease in relative osteoclast abundance in the infected femurs of *Il1b*$^{-/-}$ mice compared to WT mice (**Fig 29 D**). In summary, these data suggest that IL-1β, rather than IL-1α, is the predominant IL-1R1 cytokine that drives trabecular bone loss and osteoclastogenesis during *S. aureus* osteomyelitis.

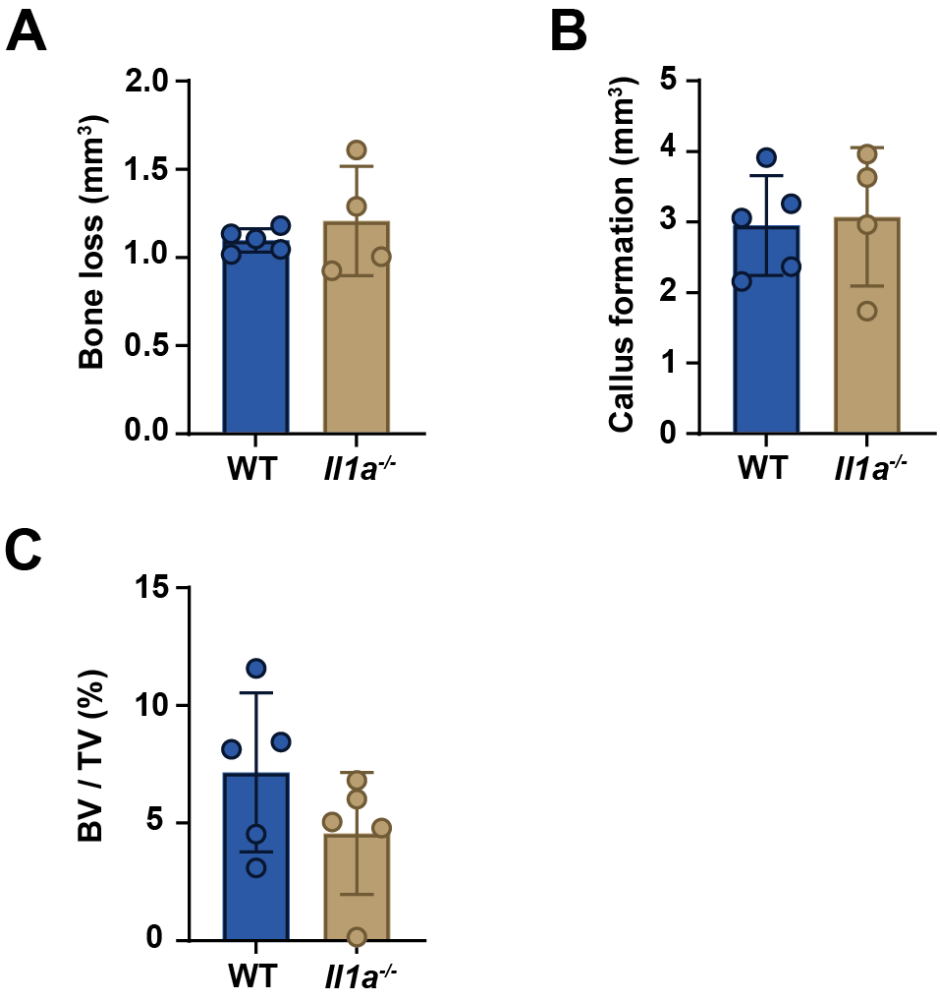

Figure 28. IL-1α-deficiency does not significantly alter changes to bone homeostasis occurring in response to *S. aureus* osteomyelitis. WT and *Il1a*$^{-/-}$ female mice were subjected to osteomyelitis by intraosseous injection of 10^6 CFU of *S. aureus.* Infected femurs and organs were extracted on day 14 post-infection. Error is plotted as standard deviation. Results are representative of one experimental replicate with n = 5 WT mice and n = 5 *Il1a*$^{-/-}$ mice. **A-B)** Femurs were fixed in neutral-buffered formalin and then imaged and analyzed using micro-computed tomography (μCT). Cortical callus formation and cortical bone loss were compared between genotypes by Mann-Whitney test. No significant differences were detected. **C)** Trabecular bone volume in infected femurs was assessed using μCT to compute trabecular bone volume over total volume (%-BV/TV). %-BV/TV of infected femurs was compared between genotypes using a Mann-Whitney test. No significant differences were detected.

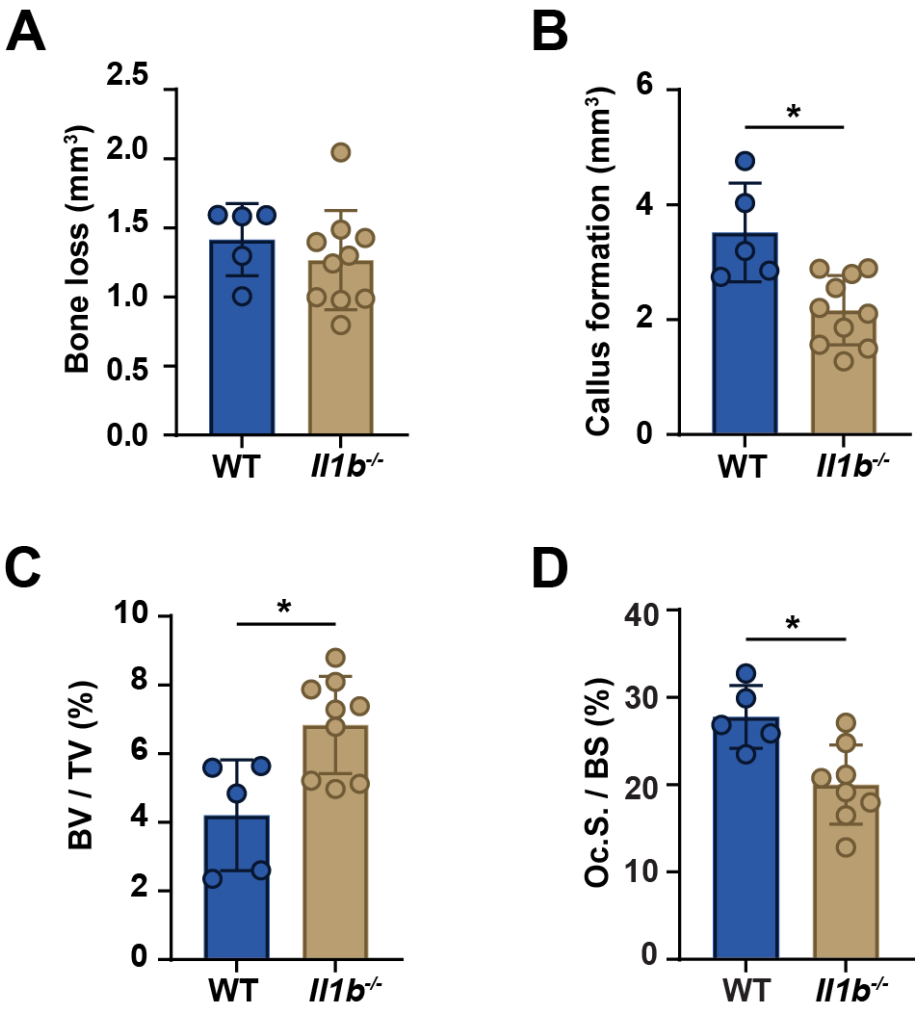

Figure 29. IL-1β-deficiency reduces callus formation, trabecular bone loss, and osteoclast abundance during *S. aureus* osteomyelitis. Female WT and *Il1b*$^{-/-}$ mice were subjected to osteomyelitis by intraosseous injection of 10^6 CFU of *S. aureus.* Infected femurs and organs were extracted on day 14 post-infection. Error is plotted as standard deviation. Results are representative of one experimental replicate with n = 5 WT mice infected on the same day and n = 9 *Il1b*$^{-/-}$ mice infected on consecutive days. **A-B)** Femurs were fixed in neutral-buffered formalin and then imaged and analyzed using micro-computed tomography (μCT). Cortical callus formation and cortical bone loss were compared between genotypes using a Mann-Whitney test, *p < 0.05. **C)** Trabecular bone volume in infected femurs was assessed using μCT to compute trabecular bone volume over total volume (%-BV/TV). %-BV/TV was compared between genotypes in infected femurs using a Mann-Whitney test, * p < 0.05. **D)** Formalin-fixed, infected femurs were decalcified and embedded to prepare for sectioning. Sectioned femurs were stained for tartrate-resistance acid phosphatase (TRAP) and histomorphometry was used to calculate TRAP$^+$ osteoclast surface relative to total bone surface (%-Oc.S./BS). A Mann-Whitney test was used to compared between genotypes, *p < 0.05.

A caspase-1/11-mediated inflammasome contributes to bone homeostasis during *S. aureus* osteomyelitis

Because mice deficient in IL-1β had greater trabecular bone volume, reduced trabecular osteoclastogenesis, and reduced callus formation compared to WT mice, we next sought to identify the pathway acting upstream of IL-1β production during osteomyelitis. Because the NLRP3 is activated by *S. aureus*, we first tested whether the NLRP3 inflammasome promotes host bacterial burden control or regulates bone homeostasis during *S. aureus* osteomyelitis (27,28,154). To do this, *Nlrp3*$^{-/-}$ mice and WT comparators were infected with 10^6 CFU of *S. aureus* to induce osteomyelitis. At 14 days post-infection (dpi), there were no significant differences in bacterial burdens in the infected femurs, kidneys, or livers of *Nlrp3*$^{-/-}$ mice compared to WT mice (**Fig. 30A**). Comparisons in weight lost over the course of infection did not reveal any differences between *Nlrp3*$^{-/-}$ and WT mice (**Fig. 30B**). Moreover, we did not detect differences in cortical bone loss or callus formation in NLRP3-deficient mice compared to WT mice (**Fig. 30C-D**). To assess how trabecular bone volume is changed by infection, we measured %-BV/TV in both the infected and contralateral femurs and compared these between genotypes using Mann-Whitney tests with correction for multiple comparisons. There were no significant differences in %-BV/TV between genotypes (**Fig 30 E**).

Since we did not find that NLRP3-deficiency reduced bacterial burden control, we next hypothesized that an NLRP3-independent inflammasome promotes host defenses during *S. aureus* osteomyelitis. To test this, we explored how deficiency in caspase-1, which can induce IL-1β maturation and gasdermin D cleavage independently of NLRP3 with other inflammasome sensors, would influence bacterial burden control and bone damage during osteomyelitis. We used a caspase-1 knockout mouse strain that also carries an incidental inactivating mutation in the caspase-11 gene (247). WT and *Casp1/11*$^{-/-}$ mice were infected with 10^5 CFU of *S. aureus* to induce osteomyelitis in the femur. This inoculum was reduced in comparison to the 10^6 CFU inoculum used in *Nlrp3*$^{-/-}$ experiments to ensure that we did not hit the highest threshold of bone damage that can be measured in this model. This increases our ability to measure meaningful differences between groups. At 14 dpi, there were no significant differences in bacterial burdens in the infected femurs, kidneys, or livers of *Casp1/11*$^{-/-}$ mice compared to WT (**Fig. 31A**). There were no differences between genotypes in weight loss over the course of infection (**Fig. 31B**). *Casp1/11*$^{-/-}$ mice had a trend toward greater callus formation and greater cortical bone destruction compared to WT mice, but this was not statistically significant (**Fig. 31C-D**). The %-BV/TV of WT and *Casp1/11*$^{-/-}$ contralateral femurs was comparable. However, the %-BV/TV of infected femurs was significantly reduced in *Casp1/11*$^{-/-}$ compared WT (**Fig. 31E**).

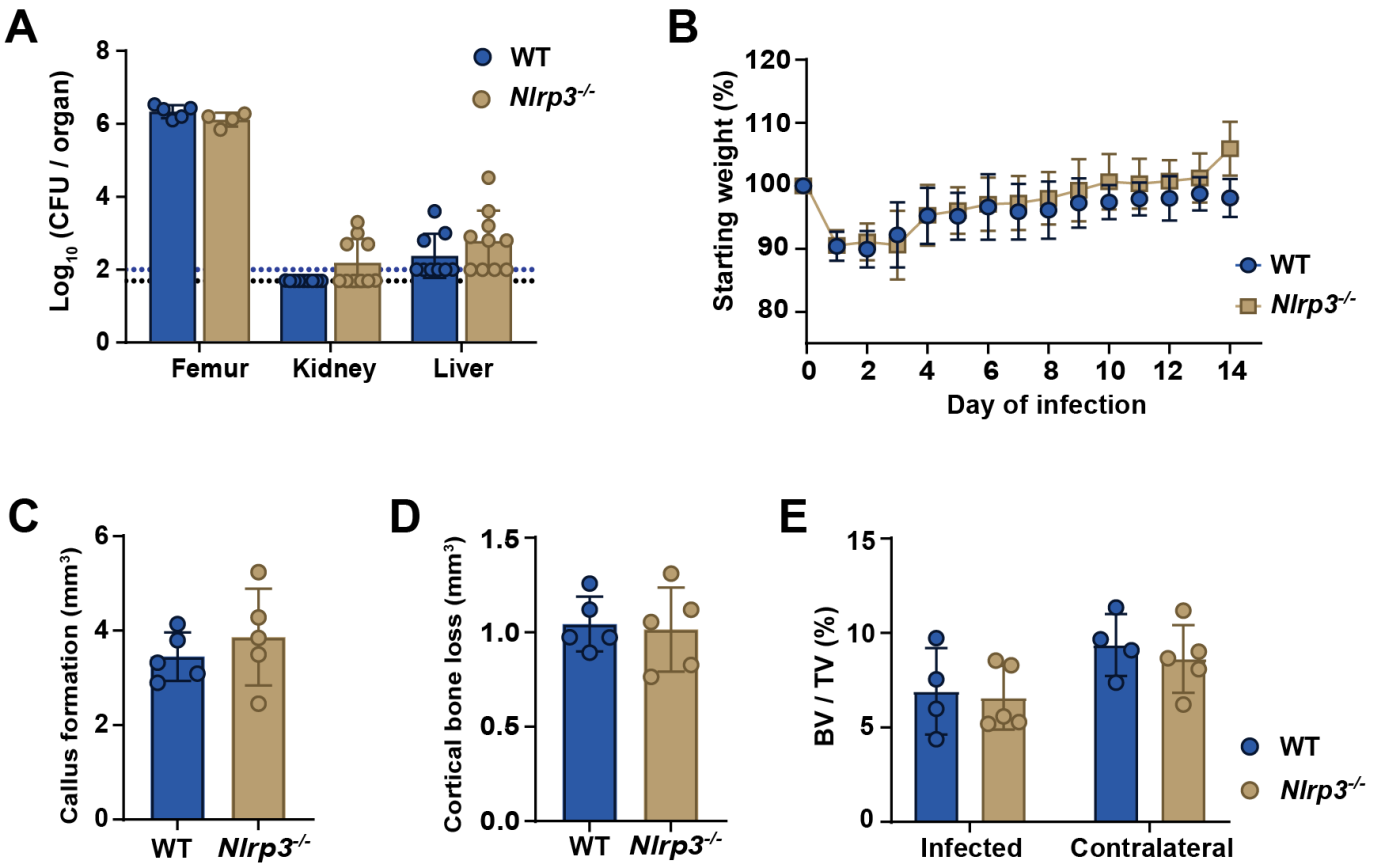

Figure 30. NLRP3-deficiency does not significantly alter bacterial burden control or bone homeostasis during *S. aureus* osteomyelitis. WT and *Nlrp3*$^{-/-}$ mice were subjected to osteomyelitis by intraosseous injection of 10^6 CFU of *S. aureus.* Infected femurs and organs were extracted on day 14 post-infection. **A)** Femurs, kidneys, and livers were homogenized for CFU enumeration. Dotted lines indicate the Log_{10} transformed limits of detection. Log_{10} transformed CFU/femur values were compared between genotypes by multiple Mann-Whitney tests with correction for multiple comparisons. No significant differences were detected. For liver and kidney, data were pooled from the experimental replicate done for CFU enumeration and the experimental replicate done for µCT, resulting in n = 9 WT mice and n = 10 *Nlrp3*$^{-/-}$ mice. For the femurs, results represent one experimental replicate with n = 4 mice per group for WT and n = 5 mice per group for *Nlrp3*$^{-/-}$. Error is plotted as standard deviation. **B)** Mice were weighed before and every day following induction of osteomyelitis. The %-starting weights were compared between genotypes using multiple unpaired t-tests to detect significant differences at each daily timepoint. No significant differences were detected. Results are pooled from two independent experiments with n = 10 mice per genotype. Error is plotted as standard error of the mean. **C)** Callus formation was measured by micro-computed tomography (µCT) and values were compared between genotypes by unpaired t-test. No significant differences were detected. Results are representative of one experimental replicate with n = 5 mice per genotype. **D)** Cortical bone loss was calculated using µCT and values were compared between genotypes by unpaired t-test. No significant differences were detected. Results are representative of one experimental replicate with n = 5 mice per genotype. **E)** Trabecular bone volume was assessed using µCT to compute trabecular bone volume over total volume (%-BV/TV). %-BV/TV was compared between genotypes for the contralateral and infected femurs using Mann-Whitney U-test with correction for multiple comparisons. No significant differences were found. Results are representative of one experimental replicate with n = 5 mice per genotype.

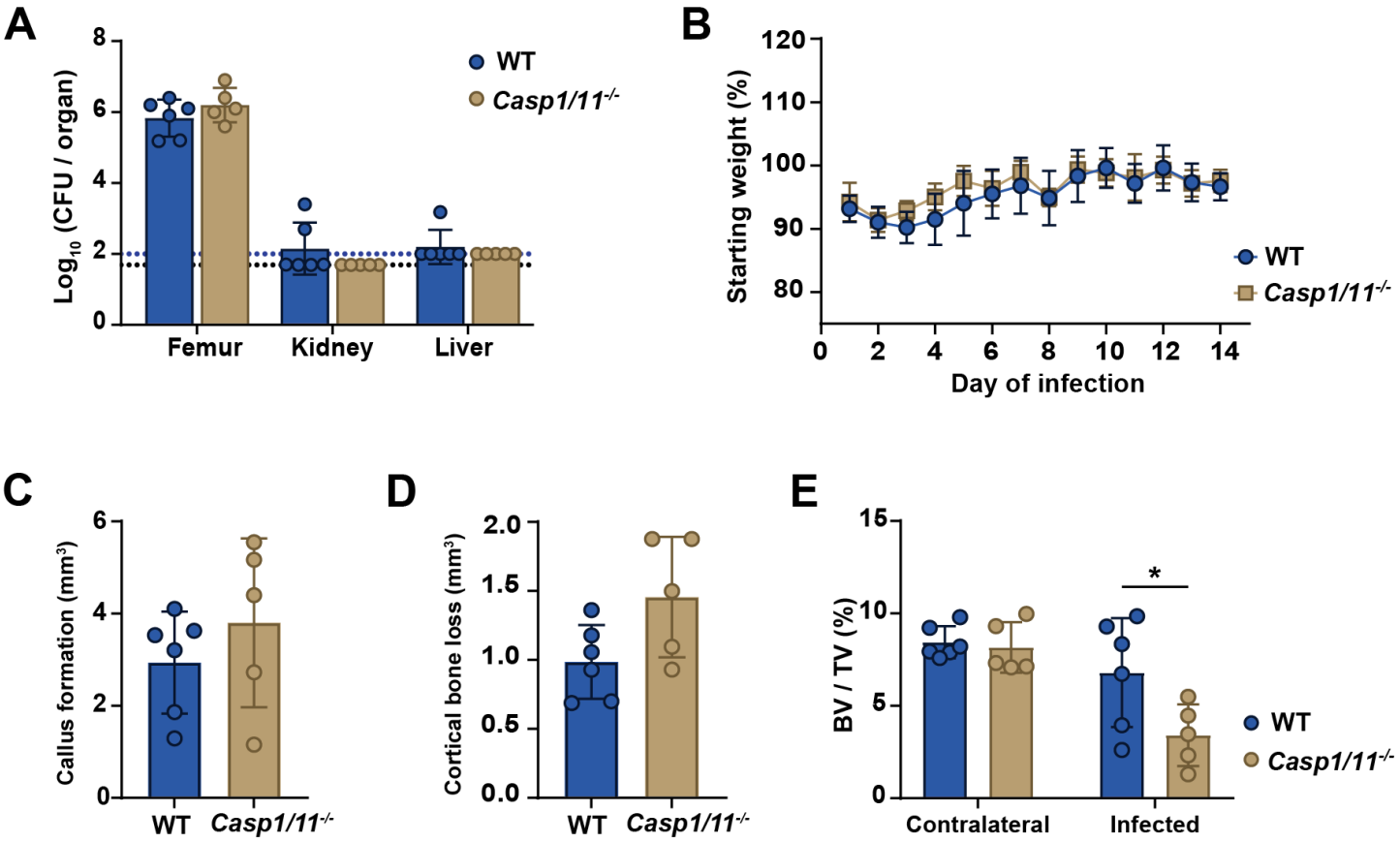

Figure 31. Caspase-1/11-deficiency does not significantly alter the bacterial burden control but does enhance bone loss during *S. aureus* osteomyelitis. WT and *Casp1/1*$^{-/-}$ mice were subjected to osteomyelitis by intraosseous injection of 10^5 CFU of *S. aureus.* Infected femurs and organs were extracted on day 14 post-infection. **A)** Femurs, kidneys, and livers were homogenized for CFU enumeration. Dotted lines indicate the Log_{10} transformed limits of detection. Log_{10} transformed CFU/organ values were compared between genotypes by multiple Mann-Whitney tests. No significant differences were detected. Results represent one experimental replicate with n = 6 mice per group for WT and n = 5 mice per group for *Casp1/11*$^{-/-}$. Error is plotted as standard deviation. **B)** Mice were weighed before and every day following induction of osteomyelitis. The %-starting weights were compared between genotypes using multiple unpaired t-tests to detect significant differences at each daily timepoint. Results represent one experimental replicate with n = 6 mice for WT and n = 6 mice for *Casp1/11*$^{-/-}$. Error is plotted as standard error of the mean. **C)** Callus formation was measured by micro-computed tomography (µCT) and values were compared between genotypes by an unpaired t-test. No significant differences were detected. Results are representative of one experimental replicate with n = 5 mice per genotype. Error is plotted as standard deviation. **D)** Cortical bone loss was calculated using µCT and values were compared between genotypes by unpaired t-test resulting in p = 0.0550. Results are representative of one experimental replicate with n = 5 mice per genotype. Error is plotted as standard deviation. **E)** Trabecular bone volume was measured using µCT to compute trabecular bone volume over total volume (%-BV/TV). The effect of genotype and infection on %-BV/TV was assessed by a two-way ANOVA. Contralateral and infected femur %-BV/TV were compared between genotypes using Sidak's multiple comparisons test, *p < 0.05. Results are representative of one experimental replicate with n = 5 mice for per genotype. Error is plotted as standard deviation.

Discussion

Transcriptional and epigenetic reprogramming through RANK signaling is an essential part of osteoclastogenesis through which monocytes transform into a large, multinucleated, resorbing osteoclasts. Major events in RANK-mediated molecular reprogramming have been elucidated (85,88,92,93,250). Whether the differentiation process entirely restricts osteoclasts from engaging in myeloid-associated inflammatory responses is not fully understood, despite the important role osteoclasts play in inflammatory bone loss and bone damage. In this chapter, we evaluate whether osteoclasts mount an inflammatory response to *S. aureus* by characterizing the inflammasome response to canonical NLRP3 stimuli, *S. aureus* supernatants, and live infection. We found that osteoclasts activate a caspase-1-associated inflammasome in response to the canonical NLRP3 stimuli LPS + nigericin. However, *S. aureus* supernatant did not fully prime the osteoclast inflammasome, as subsequent stimulation with nigericin did not induce IL-1β maturation in osteoclasts, as it did in macrophage comparators. *S. aureus* infection did not strongly activate the osteoclast inflammasome but did increase protein levels of pro-IL-1β. Caspase-1 cleavage and IL-1β maturation occurred in infected osteoclasts when potassium efflux was induced by nigericin, demonstrating that the osteoclast inflammasome retains the capacity to activate during infection. These findings suggest that the priming signal, in addition to upregulating transcription and translation of inflammasome proteins, also controls other aspects of NLRP3 readiness for activation in osteoclasts. Moreover, results from a *S. aureus* osteomyelitis mouse model suggest a role for IL-1β, not IL-1α, in controlling osteoclast-associated bone loss and in the trabecular region and in controlling callus formation near damaged cortical bone. Follow up studies revealed that NLRP3 may not be the driver of IL-1β-associated changes to bone homeostasis but suggests a role for caspase-1/11 in these processes.

Data from qRT-PCR experiments showed that *Il1b* and *Nlrp3* transcription is upregulated in osteoclasts responding to LPS. Immunoblots corroborate this by revealing pro protein accumulation in LPS-stimulated osteoclasts. Thus, these data support that osteoclasts undergo inflammasome priming and activation. However, upon stimulation with LPS + nigericin, osteoclasts leave pro-caspase-1, pro-gasdermin D, and pro-IL-1β un-cleaved. In fact, osteoclasts release and cleave about half as much IL-1β as macrophages in response to LPS + nigericin. Thus, these data point toward post-translational rather than transcriptional mechanisms of negative regulation of NLRP3 in osteoclasts. Why greater cleavage of available pro protein does not occur may be related to post-translational modifications that restrict activation (151). As a proteolytic activator, inhibition of caspase-1 cleavage may be a limiting mechanism. Recently, an N-terminal cleavage species of gasdermin D was shown to bind directly to

caspase-1 to block its activation (184). A similar mechanism could be at play in osteoclasts, which are known to use a p20 cleavage species of gasdermin D to regulate resorption (196). Assembly of the inflammasome itself may be restricted in osteoclasts due to the unique cytoskeletal architecture of these cells (251). To this point, dispersal of the trans-Golgi network is essential to the eventual docking of NLRP3 for assembly. If this does not occur efficiently in osteoclasts, it could restrict activation (176).

The studies presented in this chapter revealed that osteoclasts prime the inflammasome in response to LPS. Importantly, *S. aureus* supernatants were more effective at priming the macrophage inflammasome compared to the osteoclast inflammasome. This suggests that osteoclasts may have specific requirements for priming. To better understand the distinction between LPS and *S. aureus* supernatant priming in osteoclasts, we could test if increasing doses of supernatant or other relevant staphylococcal stimuli effectively prime the osteoclast inflammasome for activation. This would help discern whether it is the type of signal or the strength of signal that most controls priming and activation in osteoclasts. Follow up studies using TLR knockout cells would be helpful in determining how TLR stimulation affects NLRP3 activation. Moreover, in response to intracellular infection with *S. aureus*, significant IL-1β release was not observed in osteoclasts unless nigericin was given as a 2nd signal. It will be interesting to better understand whether *S. aureus* infection simply does not provide the required signals for osteoclast inflammasome activation, or whether *S. aureus* is able to prevent the osteoclast inflammasome from activating. Osteoclasts are known to act as repositories for *S. aureus* at low MOIs (252,253). Thus, understanding the signals that are required for or restrictive of inflammasome activation during infection may lead to insights on how *S. aureus* interacts with osteoclasts. Additionally, osteoclast death was induced by a MOI of 50 and 100. IL-1β release was low in infected osteoclasts, compared to macrophages, suggesting the cell death observed is not pyroptosis. Osteoclasts utilize receptor interacting serine/threonine kinase 1 (RIPK1) as part of gasdermin D-mediated control of resorption (196). Osteoclasts also express other caspases like caspase-3, -7, and -8, thus it is possible that a different form of programmed cell death is incited by infection (196).

In a previous publication, our research group reported an important role for the IL-1R1 receptor in promoting the host immune response to *S. aureus* osteomyelitis (51). Despite having worse bacterial infections, IL-1R1-deficient mice lost less trabecular bone and had less trabecular osteoclast formation (51). This suggests that IL-1R1-medaited inflammatory process drive osteoclast-associated bone loss. The *in vivo* mouse studies shown in this chapter reveal that IL-1β rather than IL-1α promotes osteoclast-associated trabecular bone loss through IL-1R1. From this, we hypothesized that NLRP3 is responsible for IL-1β production and thus expected NLRP3-deificent mice to phenocopy IL-1β-deficient mice. However, these mice had no discernable changes to host bacterial burden control or bone homeostasis

in an infection with 10^6 CFU of *S. aureus*. Caspase-1-deficient mice had more severe trabecular bone loss than WT mice in an infection performed at a lower inoculum, 10^5 CFU, which typically reduces overall bone damage. Importantly, these studies are comprised of one independent experiment with only one inoculum tested for each genotype, and thus must be replicated. However, the findings do suggest that an NLRP3-independent inflammasome like AIM2 could play a role in generating IL-1β in response to bone infection. Moreover, there may be differential effects of the cytokine-releasing versus pyroptosis-inducing consequences of inflammasome activation on bone homeostasis. Thus, while loss of IL-1β may reduce bone loss, preventing pyroptosis as a form of cell death may alter a different aspect of bone homeostasis. This has been reported in *S. aureus* lung infection, where cytokine release promotes the immune response, but cytokine-independent effects cause tissue damage (31). Importantly, gasdermin D is known to play a role in fracture healing and gasdermin D-deficient mice have been reported to have worse bone loss during inflammation due to uninhibited osteoclast resorption (195,196). Thus, it is possible that in *Casp1/11*$^{-/-}$ mice compared to WT, trabecular bone loss was more severe and cortical bone damage was trending toward more severe because the inflammasome plays a role in bone repair and homeostasis.

The studies presented in this chapter have additional limitations that must be considered. In general, we did not use the same parameters for all cell culture experiments shown in this chapter. Earlier experiments used a 7-day culture paradigm, which was modified starting with Figure 23. Additionally, due to a supply chain issue, we were not able to concentrate bacterial supernatants for a long period of time and thus used both unconcentrated and concentrated preparations in these studies. It will be important to repeat key studies with identical parameters. Furthermore, inflammasome priming can be addressed in a variety of ways. In this study, we chose to look at transcriptional and translational induction of inflammasome protein components and targets as a proxy for priming. We did not look at any of the hallmark post-translational modifications that are added or removed during priming in macrophages (151). This is an essential future direction for this work. Additionally, this study was limited to assessing NLRP3 activation following a substantial priming window that allowed for *de novo* transcription. Published work indicates that some cells, including macrophages, can activate NLRP3 following a brief priming period or inhibition of protein synthesis (178,179). We did not test whether osteoclasts can do this, and this phenomenon could explain the unique priming requirements of osteoclasts. While we used control stimuli known to activate on NLRP3 and we confirmed a caspase-1/11 dependence of IL-1β release, experiments to examine NLRP3 oligomerization and to inhibit NLRP3 genetically or chemically are important to confirm NLRP3 is entirely responsible for the cytokine cleavage measured. Additionally, experiments assessing inflammasome responses and cell death

during intracellular infection examined only a few timepoints. A more thorough investigation is needed to confirm that peak cell death is not concurrent with inflammasome activation that may occur between 6 h and 24 h post-inoculation. We are also mindful that we tested only the AH1263 strain of *S. aureus*. Using other clinically relevant strains may yield different results.

In summary, the findings presented in this chapter highlight the inflammatory potential of osteoclast lineage cells. Pursuing a more mechanistic understanding of the molecular events required for full activation of the osteoclast inflammasome will yield insight into the role of osteoclasts in bone damage during osteomyelitis.

CHAPTER IV: CONCLUSIONS AND FUTURE DIRECTIONS

Chapter II: Summary

The work I presented in Chapter II was guided by the following two related hypotheses: 1.) TLR2 and TLR9, which sense bacterial lipoproteins and CpG-DNA, respectively, are major drivers of the host response to staphylococcal infection during osteomyelitis and 2.) TLR2 and TLR9 contribute to the inflammation that drives dysregulation of bone homeostasis through osteoclast-lineage cells. The *in vitro* findings of Chapter II demonstrate that TLR2 is a driver of osteoclast differentiation in response to *S. aureus* supernatants. Cytokine release in RANKL-primed osteoclast precursors and macrophages upon stimulation with *S. aureus* supernatant was almost entirely TLR2-dependent. In response to live infection, RANKL-primed precursors continued differentiation into mature osteoclasts, and this was only partially TLR2- and TLR9-dependent. Thus, *in vitro* findings suggest that TLR2 and TLR9 have the potential to promote osteoclastogenesis during an *in vivo* infection, but other bacterial-sensing mechanisms may also contribute. Using a mouse model of post-traumatic *S. aureus* osteomyelitis, I found that TLR2 is not a significant driver of host bacterial containment, osteoclastogenesis, or dysregulation of bone homeostasis. I hypothesized that redundancy in innate immune pathways allowed host bacterial containment to proceed in the absence of TLR2, and so I next tested whether loss of both TLR2 and TLR9 would alter infection severity or bone pathology during *S. aureus* osteomyelitis. No differences were found in host bacterial burden control in *Tlr2/9*$^{-/-}$ mice compared to WT mice. *Tlr2/9*$^{-/-}$ mice had a significant reduction in callus formation in the cortical bone and a modest, but significant, reduction in trabecular bone loss. There was no parallel change to osteoclastogenesis in the trabecular bone. In combination with findings from a model of systemic *S. aureus* infection, the results from the osteomyelitis experiments support the conclusion that redundancy in the innate immune pathway allows for sufficient antibacterial responses when TLR2 and TLR9 are absent. To begin to test this hypothesis, I also evaluated IL-1β levels in the contralateral and infected femurs of WT and *Tlr2/9*$^{-/-}$ mice. There were no significant differences in cytokine abundance between *Tlr2/9*$^{-/-}$ mice and WT mice. Thus, in summary, the findings I presented in Chapter II demonstrate that TLR2- and TLR9-independent modes of host bacterial detection likely participate in the host response to *S. aureus* osteomyelitis. Future work should further interrogate the basis for the differential role of TLR2

in osteoclastogenesis *in vitro* versus *in vivo*, as a means of determining which innate immune receptors play the greatest role in driving bone pathology.

Chapter II: Future directions

Investigate the RANK-mediated regulation of TLR expression

The experimental paradigms used in the cell culture studies shown in Chapter II are based on the idea that osteoclast precursors in the bone express TLR2 and TLR9. This has been shown in cell culture, where protein and RNA levels of TLR2 and TLR9 have been measured (121,126). In culture studies, sialylation of TLR2 has been shown to enable its binding to Siglec-15 to initiate osteoclast fusion (254). Thus, cell culture findings suggest TLR2 and TLR9 should heavily influence osteoclasts during infection *in vivo*, and yet I did not find this to be the case in the model of *S. aureus* osteomyelitis used in these studies. Confirmation of the assumption that osteoclast precursors and mature cells express TLRs *in vivo* would be of use to researchers in the broad field of osteoimmunology. This could be achieved by using flow cytometry to examine TLR2 and TLR9 abundance on osteoclast precursors isolated from the bone marrow. It would be of particular interest to see whether osteoclast precursors, defined by Charles et al. as monocytes expressing $Cd11b^{lo}/Ly6C^{hi}$, express TLR2 and TLR9 at significant levels (255). Within this population, we could examine how relative levels of RANK on the cell surface correlate with TLR2 and TLR9 expression. This experiment could be done in mice at baseline and at 1, 3-, 5-, 7-, and 14-days post-induction of osteomyelitis. It would be interesting to understand whether inflammation from the infection response alters osteoclastogenic expression of TLRs. Additionally, we could look at TLR2 and TLR9 localization within infected and contralateral femurs from WT mice subjected to *S. aureus* osteomyelitis. This could be done by sectioning femurs and using immunofluorescent antibody staining to detect TLR2 and TLR9, in combination with fluorescent TRAP staining. Through this study, we could see whether $TRAP^{+}$ osteoclasts in the trabecular bone express TLR2 and TLR9 *in vivo*, as has been shown *in vitro*. These data would substantiate continued investigation into how TLR signaling influences osteoclasts during infection.

A major limitation of the work presented in Chapter II is that we did not perform test whether TLR2 or TLR9 play a role in osteoclast function. If the studies described in the prior paragraph support the notion that osteoclasts express TLRs *in vivo*, then it would be appropriate to test how deficiency in TLR2 and/or TLR9 affects osteoclast resorption. This can be done by culturing osteoclasts on either bovine bone chips or on dentin chips. Osteoclasts deficient in TLR2, TLR9, and TLR2/9, and WT control

cells, would be cultured on the bone surface until they begin to show pit formation, indicative of resorption. We could then test whether cellular stimulation with *S. aureus* supernatants or heat-killed bacteria increases resorption. This concept is based on published work showing that infection with live *S. aureus* increases resorption (120). We could measure resorption by assessing the number and size of pits formed on the bone surface or by doing an ELISA for type I collagen. Thus, we could quantify whether cells lacking TLR2 and/or TLR9 resorb different amounts of bone at baseline or in response to *S. aureus* stimulation. This would help to clarify the functional role of TLRs in mature osteoclasts.

Identify novel mechanisms of bacterial sensing that promote osteoclastogenesis

In Chapter II, I showed that RANKL-primed osteoclast precursors progress to osteoclasts when RANKL is withdrawn, and *S. aureus* is inoculated into the culture. Thus, cellular sensing of, or interactions with, *S. aureus* promotes osteoclastogenic signaling in the absence of ongoing RANKL stimulation. The ability of TLR ligation to promote osteoclastogenesis is well established (126,127). Thus, it was surprising to observe that differentiation in response to infection proceeded even in TLR2- and 9-deficient osteoclast precursors. Future experiments should aim to determine TLR2- and TLR9-independent mechanisms of *S. aureus*-mediated osteoclastogenesis. Repeating experiments with *Myd88*$^{-/-}$ cells would be a good first step toward understanding how MyD88-dependent pathways like TLR and IL-1R1 signaling contribute to osteoclast formation in this model. Moreover, there are MyD88-independent pathways that have been shown to promote osteoclast formation. The nucleotide-binding oligomerization domain containing protein 2 (NOD2), a sensor muramyl dipeptide contained within peptidoglycan, can promote osteoclast-induced bone loss in ovariectomy and gingivitis mouse models (256,257). NOD2 inhibitors are commercially available and thus testing the involvement of this sensing mechanism is a feasible approach. If NOD2 inhibition blunts osteoclast formation in WT cells and eliminates formation in *Tlr2/9*$^{-/-}$ cells, then there would be strong rationale to test the effect of NOD2 inhibition on host responses and on bone damage in the osteomyelitis mouse model.

While selection of specific, well-characterized pattern recognition receptors (PRRs) to test in the *in vitro* infection model may ultimately lead to important insights, it is also important to have an unbiased approach. The use of clustered regularly interspaced short palindromic repeats (CRISPR) to edit the genome has been leveraged as a screening technique to identify essential proteins involved in driving specific cellular responses (258). CRISPR could be used to find proteins that are typically not essential for osteoclastogenesis but become essential when *S. aureus* stimulation takes over for RANKL signaling. This could be done using the RAW 264.7 cell line, which can undergo osteoclastogenesis (259). While osteoclastogenic genes like *Nfact1* would be expected to be identified as essential, any

gene not essential to RANKL-mediated osteoclastogenesis, but essential to osteoclastogenesis during *S. aureus* infection, would be a candidate driver of infection-induced osteoclast differentiation.

Identify how redundancy in innate immune pathways enables the host response to bone infection

A major goal of our research group is to understand the specific immune pathways that control responses to bacteria in the bone. It was surprising to learn that TLR2- and TLR9-deficient mice did not have increased mortality or deficits in controlling bacterial burdens during *S. aureus* osteomyelitis. I also observed that *Tlr2/9*$^{-/-}$ mice were able to survive a 4-day systemic infection, which was not predicted based on prior studies (142,144). To follow up on this work, it would be useful to identify how the cells involved in the immune response to bacteria in the bone are altered in the absence of TLR2 and TLR9. Flow cytometry would be a useful approach in categorizing how stages of the immune response are altered in the absence of specific TLRs. We have previously reported that neutrophil abundance in the bone marrow peaks during osteomyelitis at day 5 post-infection (51). Because neutrophils are essential to abscess formation and bacterial containment during *S. aureus* osteomyelitis, examining how their expansion and infiltration into the bone is altered by loss of TLR2 and TLR9 signaling is an appropriate starting point in assessing immune responses (51,225). A limitation of the studies presented in Chapter II is that we did not thoroughly characterize the immune response in TLR2- and TLR9-null mice, since bacterial burden control was not impaired. This does not mean that biologically significant changes to the host response do not occur when TLR2 and TLR9 are absent.

In evaluating what other innate immune pathways contribute to the host response to *S. aureus* in the bone, it is important to consider the established role of IL-1R1 in driving neutrophil-based responses in osteomyelitis and to promoting osteoclast-associated trabecular bone loss (51). Because my preliminary experiments showed that IL-1β levels in the infected femurs were comparable between WT and *Tlr2/9-/-* mice, it is possible that there are other detection mechanisms that can promote IL-1R1 signaling to drive osteoclastogenesis. For instance, inflammasome activation through intracellular peptidoglycan sensing by a PRR like hexokinase could be driving IL-1β-dependent osteoclastogenesis in the trabecular bone (159). To understand the relative contribution of TLR2- and 9-independent immune responses, it would be useful to more comprehensively profile cytokine responses in knockout mice. To do this, we could carry out mock and *S. aureus* osteomyelitis infections in WT, *Tlr2/9*$^{-/-}$ and *Tlr2*$^{-/-}$ mice. We could collect infected/mock-infected femurs at 1-, 5-, and 14-days post-infection and then measure abundance of a panel of cytokines of interest. Using TLR2-single knockout mice would allow for a comparison between the relative contributions of TLR2 and TLR9 to cytokine responses.

The cytokine profile would point to whether a specific family of cytokines, like the TLR9-associated type I interferon response, is altered by lack of TLR2 and/or TLR9. From this information, more targeted hypotheses could be generated regarding the specific PRRs that are compensating for TLR2 and TLR9.

Chapter III: Summary

Data presented in Chapter III demonstrates that osteoclasts, which undergo RANK-mediated molecular reprogramming during differentiation from monocytes, can mount an NLRP3 inflammasome response to lipopolysaccharide (LPS) priming followed by stimulation with nigericin. The magnitude of inflammasome induction in osteoclasts is less than in macrophages, particularly when staphylococcal supernatants are used as priming agents. Overall, these results demonstrate that osteoclasts can generate IL-1β, an IL-1R1 cytokine that has long been known to promote osteoclastogenesis and bone loss in inflammatory disease (102). These findings present the possibility that osteoclast-lineage cells auto-regulate differentiation and function through IL-1β and other inflammasome-dependent processes. However, my *in vitro* studies with infected osteoclasts do no suggest that inflammasome activation readily occurs in response to intracellular infection. Thus, although these studies have caveats and require confirmation, the findings suggest inflammasome activation by osteoclasts is not a direct regulator of the osteoclast response during *S. aureus* osteomyelitis. Therefore, future studies will work to elucidate how negative regulation of the inflammasome in osteoclasts restricts caspase-1 activation and subsequent proteolytic activation of IL-1β and gasdermin D and to understand how osteoclast cell death is induced by *S. aureus* infection.

The mouse model studies presented in Chapter III followed up on published findings showing that IL-1R1 signaling promotes host bacterial containment and drives trabecular osteoclastogenesis and bone loss (51). Our results show that IL-1β, not IL-1α, promotes increased osteoclastogenesis and bone loss in response to *S. aureus*. I predicted that NLRP3 would be upstream of IL-1β potentiation, and thus an *Nlrp3*$^{-/-}$ mouse would phenocopy the *Il1b*$^{-/-}$ mouse. I expected NLRP3-deficiency would result in increased trabecular bone volume / total volume (BV/TV) during osteomyelitis. Contrary to this expectation, NLRP3-deficient mice had no significant differences in callus formation, cortical bone destruction or trabecular BV/TV, compared to WT mice. Caspase-1/11-deficient mice infected with a lower inoculum sustained significant bone damage. Trabecular BV/TV in caspase1/11-deficient mice was significantly lower than in WT mice. Initially, this was a confusing result. However, caspase-1, in addition to IL-18 and IL-1β maturation, also potentiates cell death and is suspected to have regulatory

roles in the bone (195,196). Thus, further study of the caspase-1/11-deficiency phenotype may lead to an enhanced understanding of how the inflammasome functions in the bone.

Chapter III: Future directions

Confirm NLRP3 assembly in osteoclast-lineage cells

Experiments in Chapter III were performed using LPS + nigericin as canonical activating agents of the NLRP3 inflammasome. Many studies have shown that LPS with a K^+ efflux-inducing signal results in NLRP3 oligomerization, assembly, and speck formation via ASC (173). We still need to confirm that this general process proceeds in osteoclasts and that it is responsible for the IL-1β maturation we measure. One way to do this is to repeat the ELISA and immunoblot experiments using *Nlrp3*$^{-/-}$ cells. Additionally, since NLRP3 oligomerizes during inflammasome activation, we can use immunoblotting to detect NLRP3 activation. To do this, osteoclasts will be stimulated with LPS + nigericin. Lysates will be collected for immunoblot and a crosslinking reaction will be used to preserve oligomerization of NLRP3. After running the protein on a non-denaturing gel and transferring to a membrane, NLRP3 can be detected by antibody staining and visualized on the blot as either a monomer or a higher molecular weight oligomer. Additionally, measuring speck formation would not only help to confirm NLRP3 activation, but will also offer clues as to how the cytoskeletal actin structure in osteoclast influences the localization and assemble of NLRP3. Speck formation can be visualized by performing NLRP3 activation experiments with cells from ASC-citrine mice (Jax stock # 030744). The ASC in these cells fluoresces weakly in the green channel, and this becomes significantly stronger when ASC is assembled in the inflammasome. It would be useful to also visualize actin using immunofluorescent antibody staining with a DAPI counterstain. Then speck formation can be identified in cells in the culture that are multinucleated and have an actin ring. It would be very interesting to observe and quantify how many of the cells with 3 or more nuclei are also speck-positive. Heterogeneity within the osteoclast culture is a difficult variable to entirely control. A culture of mature osteoclasts will still have some mononuclear cells and, due to the kinetics of fusion and fission, there is inter-experiment variation. This proposed study has the potential to show whether the more differentiated osteoclasts in the culture have speck formation.

Identify post-translational regulatory mechanisms of the osteoclast inflammasome

The results from qRT-PCR and immunoblot experiments demonstrate that osteoclasts upregulate transcription and translation of NLRP3 inflammasome components in response to LPS, *S. aureus* supernatants, and live infection with *S. aureus*. Despite this, osteoclasts cleave caspase-1 at a lower rate compared to macrophages, and staphylococcal supernatants are relatively weak inducers of the inflammasome response in osteoclasts. Thus, there is a block in the activation of NLRP3 somewhere between synthesis of the components and assembly of the complex. To understand this nuance, first it would be useful to determine whether protein synthesis is required for osteoclast inflammasome activation. In macrophages, protein synthesis is not required, but can boost the magnitude of activation (177). To test whether this is the case in osteoclasts, we could use cycloheximide, which blocks mRNA translocation to the ribosome (260). If treating osteoclasts with cycloheximide before LPS priming inhibits subsequent IL-1β cleavage, then we could conclude that translation is required for priming. Since the data in Chapter III suggests that transcriptional and translational priming occur in osteoclasts, new data from the described experiment would confidently direct focus toward post-translational mechanisms of control of NLRP3 activation and away from continued examination of how priming signals influence pro protein accumulation.

Additionally, it is important to begin to identify post-translational modifications that negatively regulate the inflammasome in osteoclasts. The first post-translational modification I would examine is ubiquitination of NLRP3. This can be done by immunoprecipitating NLRP3 from the cell lysate following LPS treatment or LPS + nigericin treatment. Additionally, testing different TLR2, TLR4, and TLR2/4 stimulating agents as primers in this experiment will help elucidate how the strength and specificity of the TLR signal may control this priming step. Ubiquitination should decrease following TLR priming and disappear following nigericin (177). Thus, comparing how the TLR stimulus and the amount of priming time influences NLRP3 ubiquitination in osteoclasts versus macrophages will determine the signals needed for osteoclasts to perform this step of post-translational priming. Ubiquitination can be visualized by immunoblotting with an anti-ubiquitin antibody post-precipitation of NLRP3.

Assess regulatory roles for gasdermin D in osteoclast inflammasome activation

Recently, a novel role for gasdermin D was identified in osteoclasts. The p20 cleavage product of gasdermin D regulates osteoclast resorption (196). This occurs through activation of caspase-8 and receptor interacting protein kinase 1 (RIPK1) which then activate caspase-3 to cleave gasdermin D (196). I have not observed this p20 fragment in any of my immunoblots. This is likely because it requires an antibody that can detect multiple cleavage products, such as Abcam catalog # ab209845. We have

observed cleavage of gasdermin D into its N-terminal, p31, membrane pore-forming subunit. Thus, it would be extremely interesting to understand if a cell that is actively cleaving gasdermin D into the p20 species through caspase-8/caspase-3 can also activate caspase-1 to cleave gasdermin D at a different site. If this does occur, then defining the mechanism by which a switch from p20 to p31 cleavage occurs is an important future direction. Importantly, caspase-8 can induce pyroptosis by directly cleaving gasdermin D (261). Caspase-1 is activated downstream of gasdermin D pore formation. In fact, K^+ efflux from the pores acts as a second signal for NLRP3 activation. This is not dissimilar to non-canonical inflammasome induction through caspase-11 (261,262). It will be important to discern whether the IL-1β maturation we observed is a result of crosstalk between caspase-1 and caspase-8.

A first step toward defining the relationship between gasdermin D-mediated regulation of osteoclast function and inflammasome activation would be to blot for the p20 cleavage unit in our cells. We could then measure how the relative abundance of this cleavage species changes when inflammasome inducing stimuli (LPS + nigericin) are administered. Examining whether caspase-3 activation via a cleavage product is occurring in osteoclasts stimulated with LPS + nigericin will also be interesting. If results suggest the p20 fragment is produced by osteoclasts that are also cleaving the p31 species, then the question of whether crosstalk between caspase-1 and caspase-8 is occurring would be addressed next. If cells producing the p20 species cannot activate the inflammasome, then there is strong rationale to interrogate how osteoclast differentiation enforces restriction of caspase-1 activation.

Determine the mode of cell death occurring in *S. aureus*-infected osteoclasts

In vitro infection data presented in Chapter III show that osteoclasts die in response to infection with *S. aureus*. Our current experimental evidence suggests this death is not pyroptosis. These experiments need to be repeated with additional parameters to strengthen this preliminary conclusion. Based on current findings, it is necessary to consider whether RANK-induced molecular reprogramming biases osteoclasts toward a certain type of cell death program. This question can be addressed in combination with follow up experiments to confirm that pyroptosis is not responsible for osteoclast death during *S. aureus* infection. To investigate this, we could start by performing a time course of infection with an MOI of 50 and 100. Cell supernatants and lysates and would be collected for use in immunoblotting at 6, 12, 18, and 24 h post-inoculation. To assay the signaling pathway associated with apoptosis, we would then immunoblot for caspase-3, caspase-9, and caspase-7, which are involved in intrinsic apoptosis. As a control, one set of cells would receive the apoptosis-inducing stimuli tumor necrosis alpha (TNFα) and cycloheximide treatment. To assess necroptosis, we would immunoblot for

caspase-8, RIPK1, RIPK3, mixed lineage kinase domain-like (MLKL), and phosphorylated MLKL. Phosphorylated MLKL is the highest confirmatory evidence of necroptosis (263). We would induce pyroptosis using the positive control TNFα + Smac mimetic (birinipant 100 nM) + zVAD(OMe)-FMK (264). Since many cell death signaling proteins are labile, identifying target proteins involved in a programmed cell death cascade may require multiple time courses. Additional experiments would be carried out to define the peak of LDH release (proxy for cell death) in osteoclasts over a time course of infection with *S. aureus*. This information would be used to plan a follow up experiment where ZVAD-fmk (pan-caspase inhibitor) and necrostatin-1 (RIPK1 inhibitor that blocks necroptosis and RIPK1-mediated apoptosis) would be used to test how blocking cell death pathways influences overall cytotoxicity. We would then repeat these experiments using other clinically relevant strains of *S. aureus* to determine the ubiquity of the osteoclast response to infection. This could also lead to insights on how staphylococcal interactions with osteoclasts induce cell death.

Determine the inflammasome sensor responsible for bacterial burden control during *S. aureus* osteomyelitis

The mouse model studies presented in Chapter III must be interpreted with caution because experiments performed in *Nlrp3*$^{-/-}$ and *Casp1/11*$^{-/-}$ mice were done only once with one *S. aureus* strain with one bacterial inoculum. Thus, replicate experiments are needed to ensure the results are rigorous. If upon repeating, NLRP3-deficient mice still have no changes to bacterial burden control compared to WT, then it will be interesting to test whether the absent in melanoma 2 (AIM2) inflammasome is involved in IL-1β elaboration during osteomyelitis. AIM2 is activated by dsDNA and thus is relevant to *S. aureus* infection (165). Performing osteomyelitis experiments in AIM2-deficient mice may recapitulate the abrogation of trabecular osteoclastogenesis and bone loss observed in IL-1β-deficient mice. It will be important to establish a link between inflammasome-sensor deficiency and changes to IL-1β maturation in the bone. This can be done by using ELISA to measure total pro and cleaved IL-1β, or by immunoblot to measure cleaved IL-1β protein relative to pro protein. A proximity ligation assay can also be used as a more specific way to confirm inflammasome activation *in vivo*.

Concluding remarks

In closing, the results I presented in Chapters II and III of my dissertation contribute to the greater understanding of how innate immune processes govern bacterial burden control and pathological dysregulation of bone homeostasis during *S. aureus* osteomyelitis. The results of Chapter II suggest that TLR2 and TLR9 are not major regulators of the host response to *S. aureus* in the bone. These

results implore greater study into how redundancy in the innate immune system enables a sufficient immune response in the absence of TLR2 and TLR9. Results in Chapter III demonstrate that osteoclasts can activate the inflammasome in response to specific stimuli. There is significant potential for follow up work to expand upon these findings to build a more detailed model of the regulatory mechanisms that control the osteoclast inflammasome.

Thank you for reading this dissertation. Your time and consideration are greatly appreciated.

REFERENCES

1. Kavanagh N, Ryan EJ, Widaa A, Sexton G, Fennell J, O'Rourke S, et al. Staphylococcal Osteomyelitis: Disease Progression, Treatment Challenges, and Future Directions. Clin Microbiol Rev. 2018 Apr 14 ;31(2).

2. Walter G, Kemmerer M, Kappler C, Hoffmann R. Treatment Algorithms for Chronic Osteomyelitis. Deutsches Aerzteblatt Online. 2012 Apr 6;109(14):257–64.

3. Chen AF, Schreiber VM, Washington W, Rao N, Evans AR. What is the Rate of Methicillin-resistant *Staphylococcus aureus* and Gram-negative Infections in Open Fractures? Clin Orthop Relat Res. 2013 Oct;471(10):3135–40.

4. Kremers HM, Nwojo ME, Ransom JE, Wood-Wentz CM, Melton LJ, Huddleston PM. Trends in the Epidemiology of Osteomyelitis. Journal of Bone and Joint Surgery. 2015 May 20;97(10):837–45.

5. Calhoun J, Manring MM, Shirtliff M. Osteomyelitis of the Long Bones. Semin Plast Surg. 2009 May 30;23(02):059–72.

6. Funk SS, Copley LAB. Acute Hematogenous Osteomyelitis in Children. Orthopedic Clinics of North America. 2017 Apr;48(2):199–208.

7. Burns TC, Stinner DJ, Mack AW, Potter BK, Beer R, Eckel TT, et al. Microbiology and injury characteristics in severe open tibia fractures from combat. J. Trauma Acute Care Surg. 2012 Apr;72(4):1062–7.

8. Mandell JC, Khurana B, Smith JT, Czuczman GJ, Ghazikhanian V, Smith SE. Osteomyelitis of the lower extremity: pathophysiology, imaging, and classification, with an emphasis on diabetic foot infection. Emerg Radiol. 2018 Apr 20;25(2):175–88.

9. Schwarz EM, Parvizi J, Gehrke T, Aiyer A, Battenberg A, Brown SA, et al. 2018 International Consensus Meeting on Musculoskeletal Infection: Research Priorities from the General Assembly Questions. J Orthop Res. 2019 May 25;37(5):997–1006.

10. Zhou CH, Ren Y, Song HJ, Ali AA, Meng XQ, Xu L, et al. One-stage debridement and bone transport versus first-stage debridement and second-stage bone transport for the management of lower limb post-traumatic osteomyelitis. J Orthop Translat. 2021 May;28:21–7.

11. Lew DP, Waldvogel FA. Osteomyelitis. The Lancet. 2004 Jul 24;364(9431):369–79.

12. Kobayashi H, Fujita R, Hiratsuka S, Shimizu T, Sato D, Hamano H, et al. Differential effects of anti-RANKL monoclonal antibody and zoledronic acid on necrotic bone in a murine model of *Staphylococcus aureus*-induced osteomyelitis. J Orthop Res. 2022 Mar 1;40(3):614–23.

13. Cierny G, Mader JT, Penninck JJ. The Classic: A Clinical Staging System for Adult Osteomyelitis. Clin Orthop Relat Res. 2003 Sep;414:7–24.

14. Guo Y, Song G, Sun M, Wang J, Wang Y. Prevalence and Therapies of Antibiotic-Resistance in *Staphylococcus aureus*. Front Cell Infect Microbiol. 2020 Mar 17;10:1–11.

15. Gimza BD, Cassat JE. Mechanisms of Antibiotic Failure During *Staphylococcus aureus* Osteomyelitis. Front Immunol. 2021 Feb 12;12:1–8.

16. Croes M, van der Wal BCH, Vogely HC. Impact of Bacterial Infections on Osteogenesis: Evidence From In Vivo Studies. J Orthop Res. 2019;37(10):2067–76.

17. Belthur M v., Birchansky SB, Verdugo AA, Mason EO, Hulten KG, Kaplan SL, et al. Pathologic fractures in children with acute *Staphylococcus aureus* osteomyelitis. Journal of Bone and Joint Surgery. 2012 Jan 4;94(1):34–42.

18. Balasubramanian D, Harper L, Shopsin B, Torres VJ. *Staphylococcus aureus* pathogenesis in diverse host environments. Pathog Dis. 2017; 75.

19. Kourtis AP, Hatfield K, Baggs J, Mu Y, See I, Epson E, et al. Vital Signs: Epidemiology and Recent Trends in Methicillin-Resistant and in Methicillin-Susceptible *Staphylococcus aureus* Bloodstream Infections — United States. MMWR Morb Mortal Wkly Rep. 2019 Mar 8;68(9):214–9.

20. Tam K, Torres VJ. *Staphylococcus aureus* Secreted Toxins and Extracellular Enzymes. Fischetti VA, Novick RP, Ferretti JJ, Portnoy DA, Braunstein M, Rood JI, editors. Microbiol Spectr. 2019 Apr 12;7(2):1–34.

21. Jenul C, Horswill AR. Regulation of *Staphylococcus aureus* Virulence. Microbiol Spectr. 2018;6(1):] 669–86.

22. Cassat JE, Hammer ND, Campbell JP, Benson MA, Perrien DS, Mrak LN, et al. A secreted bacterial protease tailors the *Staphylococcus aureus* virulence repertoire to modulate bone remodeling during osteomyelitis. Cell Host Microbe. 2013;12(136):759–72.

23. Nygaard TK, Pallister KB, DuMont AL, DeWald M, Watkins RL, Pallister EQ, et al. Alpha-toxin induces programmed cell death of human T cells, B cells, and monocytes during USA300 infection. PLoS One. 2012;7(5).

24. Inoshima I, Inoshima N, Wilke GA, Powers ME, Frank KM, Wang Y, et al. A *Staphylococcus aureus* pore-forming toxin subverts the activity of ADAM10 to cause lethal infection in mice. Nat Med. 2011 Oct 18;17(10):1310–4.

25. Popov LM, Marceau CD, Starkl PM, Lumb JH, Shah J, Guerrera D, et al. The adherens junctions control susceptibility to *Staphylococcus aureus* α-toxin. Proc Natl Acad Sci. 2015 Nov 17;112(46):14337–42.

26. Wilke GA, Wardenburg JB. Role of a disintegrin and metalloprotease 10 in *Staphylococcus aureus* α-hemolysin–mediated cellular injury. Proc Natl Acad Sci. 2010 Jul 27;107(30):13473–8.

27. Muñoz-Planillo R, Franchi L, Miller LS, Núñez G. A Critical Role for Hemolysins and Bacterial Lipoproteins in *Staphylococcus aureus* -Induced Activation of the Nlrp3 Inflammasome. J Immunol. 2009 Sep 15;183(6):3942–8.

28. Craven RR, Gao X, Allen IC, Gris D, Wardenburg JB, McElvania-TeKippe E, et al. *Staphylococcus aureus* α-Hemolysin Activates the NLRP3-Inflammasome in Human and Mouse Monocytic Cells. Ratner AJ, editor. PLoS One. 2009 Oct 14;4(10):e7446.

29. Smith IDM, Milto KM, Doherty CJ, Amyes SGB, Simpson AHRW, Hall AC. A potential key role for alpha-haemolysin of *Staphylococcus aureus* in mediating chondrocyte death in septic arthritis. Bone Joint Res. 2018 Jul;7(7):457–67.

30. Nilsson IM, Hartford O, Foster T, Tarkowski A. Alpha-Toxin and Gamma-Toxin Jointly Promote *Staphylococcus aureus* Virulence in Murine Septic Arthritis. Fischetti VA, editor. Infect Immun. 1999 Mar ;67(3):1045–9.

31. Kebaier C, Chamberland RR, Allen IC, Gao X, Broglie PM, Hall JD, et al. *Staphylococcus aureus* α-Hemolysin Mediates Virulence in a Murine Model of Severe Pneumonia Through Activation of the NLRP3 Inflammasome. J Infect Dis. 2012 Mar 1;205(5):807–17.

32. DuMont AL, Nygaard TK, Watkins RL, Smith A, Kozhaya L, Kreiswirth BN, et al. Characterization of a new cytotoxin that contributes to *Staphylococcus aureus* pathogenesis. Mol Microbiol. 2011;79(3):814–25.

33. Boguslawski KM, McKeown AN, Day CJ, Lacey KA, Tam K, Vozhilla N, et al. Exploiting species specificity to understand the tropism of a human-specific toxin. Sci Adv. 2020;6(11):7515–26.

34. Wang R, Braughton KR, Kretschmer D, Bach THL, Queck SY, Li M, et al. Identification of novel cytolytic peptides as key virulence determinants for community-associated MRSA. Nat Med. 2007 Dec 11;13(12):1510–4.

35. Queck SY, Jameson-Lee M, Villaruz AE, Bach THL, Khan BA, Sturdevant DE, et al. RNAIII-Independent Target Gene Control by the agr Quorum-Sensing System: Insight into the Evolution of Virulence Regulation in *Staphylococcus aureus*. Mol Cell. 2008 Oct;32(1):150–8.

36. Boles BR, Horswill AR. agr-Mediated Dispersal of *Staphylococcus aureus* Biofilms. Cossart P, editor. PLoS Pathog. 2008 Apr 25;4(4):e1000052.

37. Rasigade JP, Trouillet-Assant S, Ferry T, Diep BA, Sapin A, Lhoste Y, et al. PSMs of Hypervirulent *Staphylococcus aureus* Act as Intracellular Toxins That Kill Infected Osteoblasts. Fitzgerald JR, editor. PLoS One 2013 May 14;8(5):e63176.

38. Ford CA, Spoonmore TJ, Gupta MK, Duvall CL, Guelcher SA, Cassat JE. Diflunisal-loaded poly(propylene sulfide) nanoparticles decrease *S. aureus*-mediated bone destruction during osteomyelitis. J Orthop Res. 2021 Feb 20;39(2):426–37.

39. Hudson MC, Ramp WK, Frankenburg KP. *Staphylococcus aureus* adhesion to bone matrix and bone-associated biomaterials. FEMS Microbiol Lett.1999 Apr 1;173(2):279–84.

40. Fischer B, Vaudaux P, Magnin M, el Mestikawy Y, Proctor RA, Lew DP, et al. Novel animal model for studying the molecular mechanisms of bacterial adhesion to bone-implanted metallic devices: role of fibronectin in *Staphylococcus aureus* adhesion. J Orthop Res. 1996 Nov 1];14(6):914–20.

41. Jefferson KK, Goldmann DA, Pier GB. Use of Confocal Microscopy To Analyze the Rate of Vancomycin Penetration through *Staphylococcus aureus* Biofilms. Antimicrob Agents Chemother. 2005 Jun;49(6):2467–73.

42. Hofstee MI, Riool M, Terjajevs I, Thompson K, Stoddart MJ, Richards RG, et al. Three-Dimensional In Vitro *Staphylococcus aureus* Abscess Communities Display Antibiotic Tolerance and Protection from Neutrophil Clearance. Freitag NE, editor. Infect Immun. 2020 Oct 19;88(11):1–16.

43. de Mesy Bentley KL, Trombetta R, Nishitani K, Bello-Irizarry SN, Ninomiya M, Zhang L, et al. Evidence of *Staphylococcus aureus* Deformation, Proliferation, and Migration in Canaliculi of Live Cortical Bone in Murine Models of Osteomyelitis. J Bone Miner Res. 2017 May;32(5):985–90.

44. de Mesy Bentley KL, MacDonald A, Schwarz EM, Oh I. Chronic Osteomyelitis with *Staphylococcus aureus* Deformation in Submicron Canaliculi of Osteocytes. JBJS Case Connect. 2018 Mar;8(1):e8–e8.

45. Masters EA, de Mesy Bentley KL, Gill AL, Hao SP, Galloway CA, Salminen AT, et al. Identification of Penicillin Binding Protein 4 (PBP4) as a critical factor for *Staphylococcus aureus* bone invasion during osteomyelitis in mice. Otto M, editor. PLoS Pathog. 2020 Oct 22;16(10):e1008988.

46. von Euw S, Wang Y, Laurent G, Drouet C, Babonneau F, Nassif N, et al. Bone mineral: new insights into its chemical composition. Sci Rep. 2019 Jun 11;9(1):8456.

47. Bolamperti S, Villa I, Rubinacci A. Bone remodeling: an operational process ensuring survival and bone mechanical competence. Bone Res. 2022 Jul 18;10(1):48.

48. Hart NH, Newton RU, Tan J, Rantalainen T, Chivers P, Siafarikas A, et al. Biological basis of bone strength: anatomy, physiology and measurement. J Musculoskelet Neuronal Interact. 2020 Sep 1;20(3):347–71.

49. Jerban S, Ma Y, Wei Z, Jang H, Chang EY, Du J. Quantitative Magnetic Resonance Imaging of Cortical and Trabecular Bone. Semin Musculoskelet Radiol. 2020 Aug 29;24(04):386–401.

50. Li J, Bao Q, Chen S, Liu H, Feng J, Qin H, et al. Different bone remodeling levels of trabecular and cortical bone in response to changes in Wnt/β-catenin signaling in mice. J. Orthop Res. 2017 Apr;35(4):812–9.

51. Putnam NE, Fulbright LE, Curry JM, Ford CA, Petronglo JR, Hendrix AS, et al. MyD88 and IL-1R signaling drive antibacterial immunity and osteoclast-driven bone loss during *Staphylococcus aureus* osteomyelitis. Miller LS, editor. PLoS Pathog. 2019 Apr 12;15(4):e1007744.

52. Nguyen J, Tang SY, Nguyen D, Alliston T. Load Regulates Bone Formation and Sclerostin Expression through a TGFβ-Dependent Mechanism. Mei L, editor. PLoS One 2013 Jan 7;8(1):e53813.

53. Adhami MD, Rashid H, Chen H, Clarke JC, Yang Y, Javed A. Loss of Runx2 in Committed Osteoblasts Impairs Postnatal Skeletogenesis. J Bone Miner Res. 2015 Jan;30(1):71–82.

54. Yasuda H, Shima N, Nakagawa N, Yamaguchi K, Kinosaki M, Mochizuki SI, et al. Osteoclast differentiation factor is a ligand for osteoprotegerin/osteoclastogenesis-inhibitory factor and is identical to TRANCE/RANKL. Proc Natl Acad Sci. USA 1998 Mar 31;95(7):3597–602.

55. Jilka RL. Biology of the basic multicellular unit and the pathophysiology of osteoporosis. Med Pediatr Oncol 2003 Sep;41(3):182–5.

56. Ishii M, Egen JG, Klauschen F, Meier-Schellersheim M, Saeki Y, Vacher J, et al. Sphingosine-1-phosphate mobilizes osteoclast precursors and regulates bone homeostasis. Nature. 2009 Mar 8 ;458(7237):524–8.

57. Kikuta J, Kawamura S, Okiji F, Shirazaki M, Sakai S, Saito H, et al. Sphingosine-1-phosphate-mediated osteoclast precursor monocyte migration is a critical point of control in antibone-resorptive action of active vitamin D. Proc Natl Acad Sci. 2013 Apr 23;110(17):7009–13.

58. McDonald MM, Khoo WH, Ng PY, Xiao Y, Zamerli J, Thatcher P, et al. Osteoclasts recycle via osteomorphs during RANKL-stimulated bone resorption. Cell. 2021 Mar;184(5):1330-1347.e13.

59. Veis DJ, O'Brien CA. Osteoclasts, Master Sculptors of Bone. Annual Review of Pathology: Mechanisms of Disease. 2023 Jan 24;18(1):257–81.

60. Nesbitt S, Nesbit A, Helfrich M, Horton M. Biochemical characterization of human osteoclast integrins. Osteoclasts express alpha v beta 3, alpha 2 beta 1, and alpha v beta 1 integrins. J Biol Chem. 1993 Aug;268(22):16737–45.

61. Davies J, Warwick J, Totty N, Philp R, Helfrich M, Horton M. The osteoclast functional antigen, implicated in the regulation of bone resorption, is biochemically related to the vitronectin receptor. Journal of Cell Biology. 1989 Oct 1;109(4):1817–26.

62. Gowen M, Lazner F, Dodds R, Kapadia R, Feild J, Tavaria M, et al. Cathepsin K Knockout Mice Develop Osteopetrosis Due to a Deficit in Matrix Degradation but Not Demineralization. J Bone Miner Res.1999 Oct 1;14(10):1654–63.

63. Xian L, Wu X, Pang L, Lou M, Rosen CJ, Qiu T, et al. Matrix IGF-1 maintains bone mass by activation of mTOR in mesenchymal stem cells. Nat Med. 2012 Jul 24;18(7):1095–101.

64. Ota K, Quint P, Ruan M, Pederson L, Westendorf JJ, Khosla S, et al. TGF-β Induces Wnt10b in Osteoclasts From Female Mice to Enhance Coupling to Osteoblasts. Endocrinology. 2013 Oct 1;154(10):3745–52.

65. Takai H, Kanematsu M, Yano K, Tsuda E, Higashio K, Ikeda K, et al. Transforming Growth Factor-β Stimulates the Production of Osteoprotegerin/Osteoclastogenesis Inhibitory Factor by Bone Marrow Stromal Cells. J Biol Chem. 1998 Oct;273(42):27091–6.

66. Ota K, Quint P, Ruan M, Pederson L, Westendorf JJ, Khosla S, et al. TGF-β Induces Wnt10b in Osteoclasts From Female Mice to Enhance Coupling to Osteoblasts. Endocrinology. 2013 Oct 1;154(10):3745–52.

67. Abdelgawad ME, Delaisse JM, Hinge M, Jensen PR, Alnaimi RW, Rolighed L, et al. Early reversal cells in adult human bone remodeling: osteoblastic nature, catabolic functions and interactions with osteoclasts. Histochem Cell Biol. 2016 Jun 9;145(6):603–15

68. Xiong J, Piemontese M, Onal M, Campbell J, Goellner JJ, Dusevich V, et al. Osteocytes, not Osteoblasts or Lining Cells, are the Main Source of the RANKL Required for Osteoclast Formation in Remodeling Bone. Heymann D, editor. PLoS One. 2015 Sep 22;10(9):e0138189.

69. Xiong J, Onal M, Jilka RL, Weinstein RS, Manolagas SC, O'Brien CA. Matrix-embedded cells control osteoclast formation. Nat Med. 2011.

70. Ikebuchi Y, Aoki S, Honma M, Hayashi M, Sugamori Y, Khan M, et al. Coupling of bone resorption and formation by RANKL reverse signalling. Nature. 2018 Sep 5;561(7722):195–200.

71. Kong YY, Sarosi I, Capparelli C, Yoshida H, Penninger JM, Dunstan CR, et al. OPGL is a key regulator of osteoclastogenesis, lymphocyte development and lymph-node organogenesis. Nature. 2002;397(6717):315–23.

72. Takeshita S, Kaji K, Kudo A. Identification and Characterization of the New Osteoclast Progenitor with Macrophage Phenotypes Being Able to Differentiate into Mature Osteoclasts. J Bone Miner Res. 2000 Aug 1;15(8):1477–88.

73. Levaot N, Ottolenghi A, Mann M, Guterman-Ram G, Kam Z, Geiger B. Osteoclast fusion is initiated by a small subset of RANKL-stimulated monocyte progenitors, which can fuse to RANKL-unstimulated progenitors. Bone. 2015 Oct;79:21–8.

74. Li B, Yu F, Wu F, Wang K, Lou F, Zhang D, et al. Visual Osteoclast Fusion via A Fluorescence Method. Sci Rep. 2018 Dec 5;8(1):10184.

75. Jacome-Galarza CE, Percin GI, Muller JT, Mass E, Lazarov T, Eitler J, et al. Developmental origin, functional maintenance and genetic rescue of osteoclasts. Nature. 2019 Apr 10;568(7753):541–5.

76. Mun SH, Park PSU, Park-Min KH. The M-CSF receptor in osteoclasts and beyond. Exp Mol Med. 2020 Aug 17;52(8):1239–54.

77. Arai F, Miyamoto T, Ohneda O, Inada T, Sudo T, Brasel K, et al. Commitment and Differentiation of Osteoclast Precursor Cells by the Sequential Expression of C-Fms and Receptor Activator of Nuclear Factor κb (Rank) Receptors. Journal of Experimental Medicine. 1999 Dec 20;190(12):1741–54.

78. Dai XM, Ryan GR, Hapel AJ, Dominguez MG, Russell RG, Kapp S, et al. Targeted disruption of the mouse colony-stimulating factor 1 receptor gene results in osteopetrosis, mononuclear phagocyte deficiency, increased primitive progenitor cell frequencies, and reproductive defects. Blood. 2002 Jan 1;99(1):111–20.

79. Stanley ER, Chitu V. CSF-1 Receptor Signaling in Myeloid Cells. Cold Spring Harb Perspect Biol. 2014 Jun 1;6(6):a021857–a021857.

80. Anderson DM, Maraskovsky E, Billingsley WL, Dougall WC, Tometsko ME, Roux ER, et al. A homologue of the TNF receptor and its ligand enhance T-cell growth and dendritic-cell function. Nature. 1997 Nov;390(6656):175–9.

81. Hsu H, Lacey DL, Dunstan CR, Solovyev I, Colombero A, Timms E, et al. Tumor necrosis factor receptor family member RANK mediates osteoclast differentiation and activation induced by osteoprotegerin ligand. Proc Natl Acad Sci. 1999 Mar 30;96(7):3540–5.

82. Darnay BG, Haridas V, Ni J, Moore PA, Aggarwal BB. Characterization of the Intracellular Domain of Receptor Activator of NF-κB (RANK). J Biol Chem. 1998 Aug;273(32):20551–5.

83. Ishida T, Mizushima S ichi, Azuma S, Kobayashi N, Tojo T, Suzuki K, et al. Identification of TRAF6, a Novel Tumor Necrosis Factor Receptor-associated Factor Protein That Mediates Signaling from an Amino-terminal Domain of the CD40 Cytoplasmic Region. J Biol Chem. 1996 Nov;271(46):28745–8.

84. Kobayashi N, Kadono Y, Naito A, Matsumoto K, Yamamoto T, Tanaka S, et al. Segregation of TRAF6-mediated signaling pathways clarifies its role in osteoclastogenesis. EMBO. 2001 Mar 15;20(6):1271–80.

85. Ikeda F, Nishimura R, Matsubara T, Tanaka S, Inoue J ichiro, Reddy S v, et al. Critical roles of c-Jun signaling in regulation of NFAT family and RANKL-regulated osteoclast differentiation. J Clin Invest. 2004 Aug;114(4):475–84.

86. David JP, Sabapathy K, Hoffmann O, Idarraga MH, Wagner EF. JNK1 modulates osteoclastogenesis through both c-Jun phosphorylation-dependent and -independent mechanisms. J Cell Sci. 2002 Nov 15 ;115(22):4317–25.

87. Iotsova V, Caamaño J, Loy J, Yang Y, Lewin A, Bravo R. Osteopetrosis in mice lacking NF-κB1 and NF-κB2. Nat Med. 1997 Nov;3(11):1285–9.

88. Takayanagi H, Kim S, Koga T, Nishina H, Isshiki M, Yoshida H, et al. Induction and Activation of the Transcription Factor NFATc1 (NFAT2) Integrate RANKL Signaling in Terminal Differentiation of Osteoclasts. Dev Cell. 2002;3:889–901. 6

89. Takayanagi H. The Role of NFAT in Osteoclast Formation. Ann N Y Acad Sci. 2007 Nov 1;1116(1):227–37.

90. Kim JH, Kim N. Regulation of NFATc1 in Osteoclast Differentiation. J Bone Metab. 2014;21(4):233.

91. Matsuo K, Galson DL, Zhao C, Peng L, Laplace C, Wang KZQ, et al. Nuclear Factor of Activated T-cells (NFAT) Rescues Osteoclastogenesis in Precursors Lacking c-Fos. J Biol Chem. 2004 Jun 18;279(25):26475–80.

92. Asagiri M, Sato K, Usami T, Ochi S, Nishina H, Yoshida H, et al. Autoamplification of NFATc1 expression determines its essential role in bone homeostasis. Journal of Experimental Medicine. 2005 Nov 7;202(9):1261–9.

93. Yasui T, Hirose J, Tsutsumi S, Nakamura K, Aburatani H, Tanaka S. Epigenetic regulation of osteoclast differentiation: Possible involvement of Jmjd3 in the histone demethylation of Nfatc1. J Bone Miner Res.. 2011;26(11):2665–71.

94. Humphrey MB, Nakamura MC. A Comprehensive Review of Immunoreceptor Regulation of Osteoclasts. Clin Rev Allergy Immunol. 2016 Aug 14;51(1):48–58.

95. Barrow AD, Raynal N, Andersen TL, Slatter DA, Bihan D, Pugh N, et al. OSCAR is a collagen receptor that costimulates osteoclastogenesis in DAP12-deficient humans and mice. J Clin Invest. 2011;121(9):3505–16.

96. Mócsai A, Humphrey MB, van Ziffle JAG, Hu Y, Burghardt A, Spusta SC, et al. The immunomodulatory adapter proteins DAP12 and Fc receptor γ-chain (FcRγ) regulate development of functional osteoclasts through the Syk tyrosine kinase. Proc Natl Acad Sci. 2004 Apr 20;101(16):6158–63.

97. Ishikawa S, Arase N, Suenaga T, Saita Y, Noda M, Kuriyama T, et al. Involvement of FcRgamma in signal transduction of osteoclast-associated receptor (OSCAR). Int Immunol. 2004 Jul 24;16(7):1019–25.

98. Paloneva J, Mandelin J, Kiialainen A, Böhling T, Prudlo J, Hakola P, et al. DAP12/TREM2 Deficiency Results in Impaired Osteoclast Differentiation and Osteoporotic Features. Journal of Experimental Medicine. 2003 Aug 18;198(4):669–75.

99. Koga T, Inui M, Inoue K, Kim S, Suematsu A, Kobayashi E, et al. Costimulatory signals mediated by the ITAM motif cooperate with RANKL for bone homeostasis. Nature. 2004;428(6984):758–63.

100. Kang JY, Kang N, Yang YM, Hong JH, Shin DM. The Role of Ca2+-NFATc1 Signaling and Its Modulation on Osteoclastogenesis. Int J Mol Sci. 2020 May 21;21(10):3646.

101. Sokhi UK, Xia Y, Sosa B, Turajane K, Nishtala SN, Pannellini T, et al. Immune Response to Persistent *Staphyloccocus aureus* Periprosthetic Joint Infection in a Mouse Tibial Implant Model. J Bone Miner Res. 2022 Mar 3;37(3):577–94.

102. Mbalaviele G, Novack D v., Schett G, Teitelbaum SL. Inflammatory osteolysis: a conspiracy against bone. J Clin Invest. 2017 Jun 1;127(6):2030–9.

103. Croes M, Boot W, Kruyt MC, Weinans H, Pouran B, van der Helm YJM, et al. Inflammation-Induced Osteogenesis in a Rabbit Tibia Model. Tissue Eng Part C Methods. 2017 Nov;23(11):673–85.

104. Levescot A, Chang MH, Schnell J, Nelson-Maney N, Yan J, Martínez-Bonet M, et al. IL-1β–driven osteoclastogenic Tregs accelerate bone erosion in arthritis. J Clin Invest. 2021 Sep 15;131(18).

105. Mertens M, Singh JA. Anakinra for rheumatoid arthritis. Cochrane Database of Systematic Reviews 2009 Jan 21;(1).

106. Syversen SW, Jørgensen KK, Goll GL, Brun MK, Sandanger Ø, Bjørlykke KH, et al. Effect of Therapeutic Drug Monitoring vs Standard Therapy During Maintenance Infliximab Therapy on Disease Control in Patients With Immune-Mediated Inflammatory Diseases: A Randomized Clinical Trial. JAMA 2021 Dec 12;326(23):2375.

107. Polzer K, Joosten L, Gasser J, Distler JH, Ruiz G, Baum W, et al. Interleukin-1 is essential for systemic inflammatory bone loss. Ann Rheum Dis. 2010 Jan;69(01):284–90.

108. Miller LS, O'Connell RM, Gutierrez MA, Pietras EM, Shahangian A, Gross CE, et al. MyD88 Mediates Neutrophil Recruitment Initiated by IL-1R but Not TLR2 Activation in Immunity against *Staphylococcus aureus*. Immunity. 2006 Jan;24(1):79–91.

109. Miller LS, Pietras EM, Uricchio LH, Hirano K, Rao S, Lin H, et al. Inflammasome-Mediated Production of IL-1 Is Required for Neutrophil Recruitment against *Staphylococcus aureus* In Vivo. J. Immunol. 2007 Nov 15;179(10):6933–42.

110. Cho JS, Guo Y, Ramos RI, Hebroni F, Plaisier SB, Xuan C, et al. Neutrophil-derived IL-1β Is Sufficient for Abscess Formation in Immunity against *Staphylococcus aureus* in Mice. DeLeo FR, editor. PLoS Pathog. 2012 Nov 29;8(11):e1003047.

111. Wang Y, Ashbaugh AG, Dikeman DA, Zhang J, Ackerman NE, Kim SE, et al. Interleukin-1β and tumor necrosis factor are essential in controlling an experimental orthopedic implant-associated infection. J Orthop Res. 2020 Aug 5;38(8):1800–9.

112. Kim JH, Jin HM, Kim K, Song I, Youn BU, Matsuo K, et al. The Mechanism of Osteoclast Differentiation Induced by IL-1. J Immunol. 2009 Aug 1;183(3):1862–70.

113. Jules J, Zhang P, Ashley JW, Wei S, Shi Z, Liu J, et al. Molecular Basis of Requirement of Receptor Activator of Nuclear Factor κB Signaling for Interleukin 1-mediated Osteoclastogenesis. J Biol Chem. 2012 May 4;287(19):15728–38.

114. Lam J, Takeshita S, Barker JE, Kanagawa O, Ross FP, Teitelbaum SL. TNF-α induces osteoclastogenesis by direct stimulation of macrophages exposed to permissive levels of RANK ligand. J Clin Invest. 2000 Dec 15;106(12):1481–8.

115. Wei S, Kitaura H, Zhou P, Ross FP, Teitelbaum SL. IL-1 mediates TNF-induced osteoclastogenesis. J Clin Invest. 2005 Feb 1;115(2):282–90.

116. Cao Y, Jansen IDC, Sprangers S, de Vries TJ, Everts V. TNF-α has both stimulatory and inhibitory effects on mouse monocyte-derived osteoclastogenesis. J Cell Physiol. 2017 Dec 1;232(12):3273.

117. Ivashkiv LB, Zhao B, Park-Min KH, Takami M. Feedback inhibition of osteoclastogenesis during inflammation by IL-10, M-CSF receptor shedding, and induction of IRF8. Ann N Y Acad Sci. 2011 Nov; 1237(1):88–94.

118. Abu-Amer Y. IL-4 abrogates osteoclastogenesis through STAT6-dependent inhibition of NF-κB. J Clin Invest. 2001 Jun 1;107(11):1375–85.

119. Shiratori T, Kyumoto-Nakamura Y, Kukita A, Uehara N, Zhang J, Koda K, et al. IL-1β Induces Pathologically Activated Osteoclasts Bearing Extremely High Levels of Resorbing Activity: A Possible Pathological Subpopulation of Osteoclasts, Accompanied by Suppressed Expression of Kindlin-3 and Talin-1. J Immunol. 2018 Jan;200(1):218–28.

120. Trouillet-Assant S, Gallet M, Nauroy P, Rasigade JP, Flammier S, Parroche P, et al. Dual Impact of Live *Staphylococcus aureus* on the Osteoclast Lineage, Leading to Increased Bone Resorption. J Infect Dis. 2015 Feb 15;211(4):571–81.

121. Takami M, Kim N, Rho J, Choi Y. Stimulation by Toll-Like Receptors Inhibits Osteoclast Differentiation. J. Immunol. 2002 Aug 1;169(3):1516–23.

122. Amcheslavsky A, Bar-Shavit Z. Interleukin (IL)-12 mediates the anti-osteoclastogenic activity of CpG-oligodeoxynucleotides. J Cell Physiol. 2006 Apr;207(1):244–50.

123. Amcheslavsky A, Bar-Shavit Z. Toll-Like Receptor 9 Ligand Blocks Osteoclast Differentiation Through Induction of Phosphatase. J Bone Miner Res. 2007 May 7;22(8):1301–10.

124. Zou W, Amcheslavsky A, Bar-Shavit Z. CpG oligodeoxynucleotides modulate the osteoclastogenic activity of osteoblasts via toll-like receptor 9. J Biol Chem. 2003;278(19):16732–40.

125. Zou W, Bar-Shavit Z. Dual Modulation of Osteoclast Differentiation by Lipopolysaccharide. J Bone Miner Res. 2002 Jul 1;17(7):1211–8.

126. Krisher T, Bar-Shavit Z. Regulation of Osteoclastogenesis by Integrated Signals From Toll-Like Receptors. J Cell Biochem. 2014 Dec;115(12):2146–54.

127. Souza PPC, Lerner UH. Finding a Toll on the Route: The Fate of Osteoclast Progenitors After Toll-Like Receptor Activation. Front Immunol. 2019 Jul 17;10(July):1–12.

128. Ji JD, Park-Min KH, Shen Z, Fajardo RJ, Goldring SR, McHugh KP, et al. Inhibition of RANK Expression and Osteoclastogenesis by TLRs and IFN-γ in Human Osteoclast Precursors. J. Immunol. 2009 Dec 1;183(11):7223–33.

129. Cao F, Zhou W, Liu G, Xia T, Liu M, Mi B, et al. *Staphylococcus aureus* peptidoglycan promotes osteoclastogenesis via TLR2-mediated activation of the NF-κB/NFATc1 signaling pathway. Am J Transl Res. 2017;9(11):5022–30.

130. Kim J, Yang J, Park OJ, Kang SS, Kim WS, Kurokawa K, et al. Lipoproteins are an important bacterial component responsible for bone destruction through the induction of osteoclast differentiation and activation. J Bone Miner Res. 2013 Nov;28(11):2381–91.

131. Fitzgerald KA, Kagan JC. Toll-like Receptors and the Control of Immunity. Cell 2020 Mar;180(6):1044–66.

132. Rock FL, Hardiman G, Timans JC, Kastelein RA, Bazan JF. A family of human receptors structurally related to Drosophila Toll. Proc Natl Acad Sci. 1998 Jan 20;95(2):588–93.

133. Jin MS, Kim SE, Heo JY, Lee ME, Kim HM, Paik SG, et al. Crystal Structure of the TLR1-TLR2 Heterodimer Induced by Binding of a Tri-Acylated Lipopeptide. Cell. 2007 Sep;130(6):1071–82.

134. Takeuchi O, Kawai T, Mühlradt PF, Morr M, Radolf JD, Zychlinsky A, et al. Discrimination of bacterial lipoproteins by Toll-like receptor 6. Int Immunol. 2001 Jul;13(7):933–40.

135. Hemmi H, Takeuchi O, Kawai T, Kaisho T, Sato S, Sanjo H, et al. A Toll-like receptor recognizes bacterial DNA. Nature. 2000 Dec 7;408(6813):740–5.

136. Fitzgerald KA, Palsson-Mcdermott EM, Bowie AG, Jefferies CA, Mansell AS, Brady G, et al. Mal (MyD88-adapter-like) is required for toll-like recepfor-4 signal transduction. Nature. 2001;413(6851):78–83.

137. Lin YC, Huang DY, Chu CL, Lin YL, Lin WW. The tyrosine kinase syk differentially regulates toll-like receptor signaling downstream of the adaptor molecules TRAF6 and TRAF3. Sci Signal. 2013;6(289):1–13.

138. Parker D, Prince A. *Staphylococcus aureus* Induces Type I IFN Signaling in Dendritic Cells Via TLR9. J. Immunol. 2012 Oct 15;189(8):4040–6.

139. Musilova J, Mulcahy ME, Kuijk MM, McLoughlin RM, Bowie AG. Toll-like receptor 2–dependent endosomal signaling by *Staphylococcus aureus* in monocytes induces type I interferon and promotes intracellular survival. J Biol Chem. 2019 Nov 8;294(45):17031–42.

140. Liu G, Zhao Y. Toll-like receptors and immune regulation: their direct and indirect modulation on regulatory CD4 + CD25 + T cells. Immunology. 2007 Oct;122(2):149–56.

141. Dennis Nurjadi, Klaus Heeg, Alexander N.R. Weber PZ. Toll-like receptor (TLR) -9 promotor polymorphisms and gene expression are associated with persistent *Staphylococcus aureus* nasal carriage. Journal of Clinical Microbiology and Infection. 2018;

142. Yimin, Kohanawa M, Zhao S, Ozaki M, Haga S, Nan G, et al. Contribution of Toll-Like Receptor 2 to the Innate Response against *Staphylococcus aureus* Infection in Mice. Jeyaseelan S, editor. PLoS One. 2013 Sep 13;8(9):e74287.

143. Watanabe I, Ichiki M, Shiratsuchi A, Nakanishi Y. TLR2-Mediated Survival of *Staphylococcus aureus* in Macrophages: A Novel Bacterial Strategy against Host Innate Immunity. J. Immunol. 2007 Apr 15;178(8):4917–25.

144. Takeuchi O, Hoshino K, Akira S. Cutting Edge: TLR2-Deficient and MyD88-Deficient Mice Are Highly Susceptible to *Staphylococcus aureus* Infection. J. Immunol. 2000 Nov 15;165(10):5392–6.

145. Skerrett SJ, Braff MH, Liggitt HD, Rubens CE. Toll-like receptor 2 has a prominent but nonessential role in innate immunity to *Staphylococcus aureus* pneumonia. Physiol Rep. 2017. Nov;5(21):e13491.

146. Schmaler M, Jann NJ, Ferracin F, Landolt LZ, Biswas L, Götz F, et al. Lipoproteins in *Staphylococcus aureus* Mediate Inflammation by TLR2 and Iron-Dependent Growth In Vivo. J. Immunol. 2009 Jun 1;182(11):7110–8.

147. Bubeck Wardenburg J, Williams WA, Missiakas D. Host defenses against *Staphylococcus aureus* infection require recognition of bacterial lipoproteins. Proc Natl Acad Sci. 2006 Sep 12;103(37):13831–6.

148. Kim NH, Sung JY, Choi YJ, Choi SJ, Ahn S, Ji E, et al. Toll-like receptor 2 downregulation and cytokine dysregulation predict mortality in patients with *Staphylococcus aureus* bacteremia. BMC Infect Dis. 2020 Dec 30;20(1):901.

149. Moore CE, Segal S, Berendt AR, Hill AVS, Day NPJ. Lack of Association between Toll-Like Receptor 2 Polymorphisms and Susceptibility to Severe Disease Caused by *Staphylococcus aureus*. Clinical and Vaccine Immunology. 2004 Nov;11(6):1194–7.

150. von Aulock S, Schröder NWJ, Traub S, Gueinzius K, Lorenz E, Hartung T, et al. Heterozygous Toll-Like Receptor 2 Polymorphism Does Not Affect Lipoteichoic Acid-Induced Chemokine and Inflammatory Responses. Infect Immun. 2004 Mar;72(3):1828–31.

151. McKee CM, Coll RC. NLRP3 inflammasome priming: A riddle wrapped in a mystery inside an enigma. J Leukoc Biol. 2020 Sep 3;108(3):937–52.

152. He Y, Hara H, Núñez G. Mechanism and Regulation of NLRP3 Inflammasome Activation. Trends Biochem Sci. 2016 Dec;41(12):1012–21.

153. Cohen TS, Boland ML, Boland BB, Takahashi V, Tovchigrechko A, Lee Y, et al. *S. aureus* Evades Macrophage Killing through NLRP3-Dependent Effects on Mitochondrial Trafficking. Cell Rep. 2018 Feb;22(9):2431–41.

154. Sokolovska A, Becker CE, Ip WKE, Rathinam VAK, Brudner M, Paquette N, et al. Activation of caspase-1 by the NLRP3 inflammasome regulates the NADPH oxidase NOX2 to control phagosome function. Nat Immunol. 2013;14(6):543–53.

155. Wang X, Eagen WJ, Lee JC. Orchestration of human macrophage NLRP3 inflammasome activation by *Staphylococcus aureus* extracellular vesicles. Proc Natl Acad Sci. 2020 Feb 11;117(6):3174–84.

156. Pires S, Parker D. IL-1β activation in response to *Staphylococcus aureus* lung infection requires inflammasome-dependent and independent mechanisms. Eur J Immunol. 2018 Oct;48(10):1707–16.

157. Backert S. Inflammasome Signaling and Bacterial Infections. Backert S, editor. Cham: Springer International Publishing; 2016. (Current Topics in Microbiology and Immunology; vol. 397).

158. Rasmussen G, Idosa BA, Bäckman A, Monecke S, Strålin K, Särndahl E, et al. Caspase-1 Inflammasome Activity in Patients with *Staphylococcus aureus* Bacteremia. Microbiol Immunol. 2019 Aug 12;1348-0421.12738.

159. Wolf AJ, Reyes CN, Liang W, Becker C, Shimada K, Wheeler ML, et al. Hexokinase Is an Innate Immune Receptor for the Detection of Bacterial Peptidoglycan. Cell. 2016 Jul;166(3):624–36.

160. Kahlenberg JM, Lundberg KC, Kertesy SB, Qu Y, Dubyak GR. Potentiation of Caspase-1 Activation by the P2X7 Receptor Is Dependent on TLR Signals and Requires NF-κB-Driven Protein Synthesis. J. Immunol. 2005 Dec 1;175(11):7611–22.

161. Bauernfeind FG, Horvath G, Stutz A, Alnemri ES, MacDonald K, Speert D, et al. Cutting Edge: NF-κB Activating Pattern Recognition and Cytokine Receptors License NLRP3 Inflammasome Activation by Regulating NLRP3 Expression. J. Immunol. 2009 Jul 15;183(2):787–91.

162. Mariathasan S, Weiss DS, Newton K, McBride J, O'Rourke K, Roose-Girma M, et al. Cryopyrin activates the inflammasome in response to toxins and ATP. Nature. 2006;440(7081):228–32.

163. Shi J, Zhao Y, Wang K, Shi X, Wang Y, Huang H, et al. Cleavage of GSDMD by inflammatory caspases determines pyroptotic cell death. Nature. 2015;526(7575):660–5.

164. Thornberry NA, Bull HG, Calaycay JR, Chapman KT, Howard AD, Kostura MJ, et al. A novel heterodimeric cysteine protease is required for interleukin-1β processing in monocytes. Nature.1992 Apr;356(6372):768–74.

165. Lugrin J, Martinon F. The AIM2 inflammasome: Sensor of pathogens and cellular perturbations. Immunol Rev. 2018 Jan 1;281(1):99–114.

166. Deets KA, Doyle RN, Rauch I, Vance RE. Inflammasome activation leads to cDC1- independent cross-priming of CD8 T cells by epithelial cell-derived antigen. Elife. 2021 Dec 1;10.

167. Tourneur L, Witko-Sarsat V. Inflammasome activation: Neutrophils go their own way. J Leukoc Biol. 2019;105(3):433–6.

168. Karmakar M, Minns M, Greenberg EN, Diaz-Aponte J, Pestonjamasp K, Johnson JL, et al. N-GSDMD trafficking to neutrophil organelles facilitates IL-1β release independently of plasma membrane pores and pyroptosis. Nat Commun. 2020 Dec 5;11(1):2212.

169. Zanoni I, Tan Y, di Gioia M, Broggi A, Ruan J, Shi J, et al. An endogenous caspase-11 ligand elicits interleukin-1 release from living dendritic cells. Science. 2016 Jun 3;352(6290):1232–6.

170. Boucher D, Monteleone M, Coll RC, Chen KW, Ross CM, Teo JL, et al. Caspase-1 self-cleavage is an intrinsic mechanism to terminate inflammasome activity. Journal of Experimental Medicine. 2018 Mar 5 ;215(3):827–40.

171. Broz P, von Moltke J, Jones JW, Vance RE, Monack DM. Differential requirement for Caspase-1 autoproteolysis in pathogen-induced cell death and cytokine processing. Cell Host Microbe. 2010 Dec 16;8(6):471–83.

172. Aksentijevich I, Putnam CD, Remmers EF, Mueller JL, Le J, Kolodner RD, et al. The Clinical Continuum of Cryopyrinopathies: Novel CIAS1 Mutations in North American Patients and a New Cryopyrin Model. Arthritis Rheum. 2007 Apr;56(4):1273.

173. Tweedell RE, Malireddi RKS, Kanneganti TD. A comprehensive guide to studying inflammasome activation and cell death. Nat Protoc. 2020 Oct 7;15(10):3284–333.

174. Muñoz-Planillo R, Kuffa P, Martínez-Colón G, Smith BL, Rajendiran TM, Núñez G. K+ Efflux Is the Common Trigger of NLRP3 Inflammasome Activation by Bacterial Toxins and Particulate Matter. Immunity. 2013 Jun;38(6):1142–53.

175. Perregaux D, Gabels CA. Interleukin-1 beta maturation and release in response to ATP and nigericin. Evidence that potassium depletion mediated by these agents is a necessary and common feature of their activity. Journal of Biological Chemistry. 1994;269(21):15195–203.

176. Chen J, Chen ZJ. PtdIns4P on dispersed trans-Golgi network mediates NLRP3 inflammasome activation. Nature. 2018 Dec 28;564(7734):71–6.

177. Juliana C, Fernandes-Alnemri T, Kang S, Farias A, Qin F, Alnemri ES. Non-transcriptional Priming and Deubiquitination Regulate NLRP3 Inflammasome Activation. J Biol Chem. 2012 Oct 19;287(43):36617–22.

178. Fernandes-Alnemri T, Kang S, Anderson C, Sagara J, Fitzgerald KA, Alnemri ES. Cutting Edge: TLR Signaling Licenses IRAK1 for Rapid Activation of the NLRP3 Inflammasome. J. Immunol. 2013 Oct 15 ;191(8):3995–9. for

179. Lin KMKM, Hu W, Troutman TDTD, Jennings M, Brewer T, Li X, et al. IRAK-1 bypasses priming and directly links TLRs to rapid NLRP3 inflammasome activation. Proc Natl. Acad Sci. 2014 Jan 14 ;111(2):775–80.

180. Ntt AS, Cortana M. Priming is Despensable for Nlrp3 inflammasome activation in human monocytes. bioRxiv. 2016;(C):67–70.

181. Schmacke NA, O'Duill F, Gaidt MM, Szymanska I, Kamper JM, Schmid-Burgk JL, et al. IKKβ primes inflammasome formation by recruiting NLRP3 to the trans-Golgi network. Immunity. 2022 Dec;55(12):2271-2284.e7.

182. Py BF, Kim MS, Vakifahmetoglu-Norberg H, Yuan J. Deubiquitination of NLRP3 by BRCC3 Critically Regulates Inflammasome Activity. Mol Cell. 2013 Jan;49(2):331–8.

183. Song N, Liu ZS, Xue W, Bai ZF, Wang QY, Dai J, et al. NLRP3 Phosphorylation Is an Essential Priming Event for Inflammasome Activation. Mol Cell. 2017 Oct 5;68(1):185-197.e6.

184. Hu Y, Jiang Y, Li S, Ma X, Chen M, Yang R, et al. The Gasdermin D N-terminal fragment acts as a negative feedback system to inhibit inflammasome-mediated activation of Caspase-1/11. Proc Natl Acad Sci. 2022 Nov 8;119(45):1–12.

185. Stehlik C, Krajewska M, Welsh K, Krajewski S, Godzik A, Reed JC. The PAAD/PYRIN-only protein POP1/ASC2 is a modulator of ASC-mediated nuclear-factor-kappa B and pro-caspase-1 regulation. Biochemical Journal. 2003 Jul 7;373(Pt 1):101.

186. Bedoya F, Sandler LL, Harton JA. Pyrin-Only Protein 2 Modulates NF-κB and Disrupts ASC:CLR Interactions. J. Immunol. 2007 Mar 15;178(6):3837–45.

187. Khare S, Ratsimandresey RA, de Almeida L, Cuda CM, Rellick SL, Misharin A v., et al. The PYRIN domain–only protein POP3 inhibits ALR inflammasomes and regulates responses to infection with DNA viruses. Nat Immunol. 2014 Apr 16;15(4):343–53.

188. Jandinski JJ. Osteoclast activating factor is now interleukin-1 beta: historical perspective and biological implications. Journal of Oral Pathology & Medicine. 1988;17(4):145–52.

189. Dewhirst FE, Stashenko PP, Mole JE, Tsurumachi T. Purification and partial sequence of human osteoclast-activating factor: identity with interleukin 1 beta. J Immunol. 1985 Oct;135(4):2562–8.

190. Cao Z, Xiong J, Takeuchi M, Kurama T, Goeddel D v. TRAF6 is a signal transducer for interleukin-1. Nature. 1996 Oct;383(6599):443–6.

191. Koryllou A, Mejbri M, Theodoropoulou K, Hofer M, Carlomagno R. Chronic Nonbacterial Osteomyelitis in Children. Children. 2021 Jun 25;8(7):551.

192. Bonar SL, Brydges SD, Mueller JL, McGeough MD, Pena C, Chen D, et al. Constitutively Activated NLRP3 Inflammasome Causes Inflammation and Abnormal Skeletal Development in Mice. Ryffel B, editor. PLoS One. 2012 Apr 27;7(4):e35979.

193. Gurung P, Burton A, Kanneganti TD. NLRP3 inflammasome plays a redundant role with caspase 8 to promote IL-1β–mediated osteomyelitis. Proc Natl Acad Sci. 2016 Apr 19;113(16):4452–7.

194. Zhu X, Zhang K, Lu K, Shi T, Shen S, Chen X, et al. Inhibition of pyroptosis attenuates *Staphylococcus aureus*-induced bone injury in traumatic osteomyelitis. Ann Transl Med. 2019;7(8).

195. Sun K, Wang C, Xiao J, Brodt MD, Yuan L, Yang T, et al. Fracture healing is delayed in the absence of gasdermin-interleukin-1 signaling. Elife. 2022 Mar 4;11.

196. Li M, Yang D, Yan H, Tang Z, Jiang D, Zhang J, et al. Gasdermin D maintains bone mass by rewiring the endo-lysosomal pathway of osteoclastic bone resorption. Dev Cell. 2022 Oct 24;57(20):2365-2380.e8.

197. Alippe Y, Wang C, Ricci B, Xiao J, Qu C, Zou W, et al. Bone matrix components activate the NLRP3 inflammasome and promote osteoclast differentiation. Sci Rep. 2017 Dec 26;7(1):6630.

198. Bhakdi S, Muhly M, Korom S, Hugo F. Release of interleukin-1 beta associated with potent cytocidal action of staphylococcal alpha-toxin on human monocytes. Infect Immun. 1989 Nov;57(11):3512–9.

199. Aldrich AL, Heim CE, Shi W, Fallet RW, Duan B, Kielian T. TLR2 and caspase-1 signaling are critical for bacterial containment but not clearance during craniotomy-associated biofilm infection. J Neuroinflammation. 2020 Dec 1;17(1):114.

200. Hanamsagar R, Aldrich A, Kielian T. Critical role for the AIM2 inflammasome during acute CNS bacterial infection. J Neurochem. 2014 May;129(4):704–11.

201. Dhanoa A, Singh VA, Mansor A, Yusof MY, Lim KT, Thong KL. Acute haematogenous community-acquired methicillin-resistant *Staphylococcus aureus* osteomyelitis in an adult: Case report and review of literature. BMC Infect Dis. 2012;12.

202. Sims NA, Vrahnas C. Regulation of cortical and trabecular bone mass by communication between osteoblasts, osteocytes and osteoclasts. Arch Biochem Biophys. 2014 Nov;561:22–8.

203. Kim BJ, Koh JM. Coupling factors involved in preserving bone balance. Cellular and Molecular Life Sciences. 2019 Apr 4;76(7):1243–53.

204. Gravallese EM, Harada Y, Wang JT, Gorn AH, Thornhill TS, Goldring SR. Identification of cell types responsible for bone resorption in rheumatoid arthritis and juvenile rheumatoid arthritis. Am J Pathol. 1998;152(4):943.

205. Chen Z, Su L, Xu Q, Katz J, Michalek SM, Fan M, et al. IL-1R/TLR2 through MyD88 Divergently Modulates Osteoclastogenesis through Regulation of Nuclear Factor of Activated T Cells c1 (NFATc1) and B Lymphocyte-induced Maturation Protein-1 (Blimp1). J Biol Chem. 2015 Dec;290(50):30163–74.

206. Lam J, Takeshita S, Barker JE, Kanagawa O, Ross FP, Teitelbaum SL. TNF-α induces osteoclastogenesis by direct stimulation of macrophages exposed to permissive levels of RANK ligand. J Clin Invest. 2000 Dec 15;106(12):1481–8.

207. Evans KE, Fox SW. Interleukin-10 inhibits osteoclastogenesis by reducing NFATc1 expression and preventing its translocation to the nucleus. BMC Cell Biol. 2007 Dec 19;8(1):4.

208. Josse J, Velard F, Gangloff SC. *Staphylococcus aureus* vs. Osteoblast: Relationship and Consequences in Osteomyelitis. Front Cell Infect Microbiol. 2015 Nov 26;5:(85).

209. Kassem A, Lindholm C, Lerner UH. Toll-Like Receptor 2 Stimulation of Osteoblasts Mediates *Staphylococcus aureus* Induced Bone Resorption and Osteoclastogenesis through Enhanced RANKL. Tang CH, editor. PLoS One. 2016 Jun 16;11(6):e0156708.

210. Mohamed W, Domann E, Chakraborty T, Mannala G, Lips KS, Heiss C, et al. TLR9 mediates *S. aureus* killing inside osteoblasts via induction of oxidative stress. BMC Microbiol. 2016 Dec 3;16(1):230.

211. Oliveira-Nascimento L, Massari P, Wetzler LM. The Role of TLR2 in Infection and Immunity. Front Immunol. 2012 Apr 18;3(APR):79.

212. Martínez-Colón GJ, Warheit-Niemi H, Gurczynski SJ, Taylor QM, Wilke CA, Podsiad AB, et al. Influenza-induced immune suppression to methicillin-resistant *Staphylococcus aureus* is mediated by TLR9. Langlois R, editor. PLoS Pathog. 2019 Jan 25;15(1):e1007560.

213. van der Meer AJ, Achouiti A, van der Ende A, Soussan AA, Florquin S, de Vos A, et al. Toll-Like Receptor 9 Enhances Bacterial Clearance and Limits Lung Consolidation in Murine Pneumonia Caused by Methicillin-Resistant *Staphylococcus aureus*. Molecular Medicine. 2016 Jan 24;22(1):292–9.

214. Boles BR, Thoendel M, Roth AJ, Horswill AR. Identification of genes involved in polysaccharide-independent *Staphylococcus aureus* biofilm formation. PLoS One. 2010 Apr 14;5(4):e10146.

215. Ford CA, Hurford IM, Fulbright LE, Curry JM, Peek CT, Spoonmore TJ, et al. Loss of Vhl alters trabecular bone loss during *S. aureus* osteomyelitis in a cell-specific manner. Front Cell Infect Microbiol. 2022 Sep 20;12:985467.

216. Fey PD, Endres JL, Yajjala VK, Yajjala K, Widhelm TJ, Boissy RJ, et al. A Genetic Resource for Rapid and Comprehensive Phenotype. mBio. 2013;4(1):e00537-12.

217. Schindelin J, Arganda-Carreras I, Frise E, Kaynig V, Longair M, Pietzsch T, et al. Fiji: an open-source platform for biological-image analysis. Nat Methods. 2012 Jul 28;9(7):676–82.

218. Schmittgen TD, Livak KJ. Analyzing real-time PCR data by the comparative CT method. Nat Protoc. 2008;3(6):1101–8.

219. An D, Kim K, Lu W. Defective Entry into Mitosis 1 (Dim1) Negatively Regulates Osteoclastogenesis by Inhibiting the Expression of Nuclear Factor of Activated T-cells, Cytoplasmic, Calcineurin-dependent 1 (NFATc1). J Biol Chem. 2014 Aug 29;289(35):24366–73.

220. Zhang J, Valverde P, Zhu X, Murray D, Wu Y, Yu L, et al. Exercise-induced irisin in bone and systemic irisin administration reveal new regulatory mechanisms of bone metabolism. Bone Res. 2017;5.

221. Spandidos A, Wang X, Wang H, Seed B. PrimerBank: a resource of human and mouse PCR primer pairs for gene expression detection and quantification. Nucleic Acids Res. 2010 Jan;38(suppl_1):D792–9.

222. Spandidos A, Wang X, Wang H, Dragnev S, Thurber T, Seed B. A comprehensive collection of experimentally validated primers for Polymerase Chain Reaction quantitation of murine transcript abundance. BMC Genomics. 2008 Dec 24;9(1):1–17.

223. Luo J, Yang Z, Ma Y, Yue Z, Lin H, Qu G, et al. LGR4 is a receptor for RANKL and negatively regulates osteoclast differentiation and bone resorption. Nat Med. 2016 May 1;22(5):539–46. /

224. Cui W, Cuartas E, Ke J, Zhang Q, Einarsson HB, Sedgwick JD, et al. CD200 and its receptor, CD200R, modulate bone mass via the differentiation of osteoclasts. Proc Natl Acad Sci. 2007 Sep 4;104(36):14436.

225. Wilde AD, Snyder DJ, Putnam NE, Valentino MD, Hammer ND, Lonergan ZR, et al. Bacterial Hypoxic Responses Revealed as Critical Determinants of the Host-Pathogen Outcome by TnSeq Analysis of *Staphylococcus aureus* Invasive Infection. Otto M, editor. PLoS Pathog. 2015 Dec 18 ;11(12):e1005341.

226. Bouxsein ML, Boyd SK, Christiansen BA, Guldberg RE, Jepsen KJ, Müller R. Guidelines for assessment of bone microstructure in rodents using micro–computed tomography. J Bone Miner Res. 2010 Jul 1 ;25(7):1468–86.

227. Cappellen D, Luong-Nguyen NH, Bongiovanni S, Grenet O, Wanke C, Šuša M. Transcriptional Program of Mouse Osteoclast Differentiation Governed by the Macrophage Colony-stimulating Factor and the Ligand for the Receptor Activator of NFκB. J Biol Chem. 2002 Jun 14;277(24):21971–82.

228. Toor SM, Wani S, Albagha OME. Comprehensive Transcriptomic Profiling of Murine Osteoclast Differentiation Reveals Novel Differentially Expressed Genes and LncRNAs. Front Genet. 2021 Nov 15;12:2225.

229. Hoffman WL, Ruggles AO, Tabarya D. Chicken anti-protein A prevents *Staphylococcus aureus* protein A from binding to human and rabbit IgG in immunoassays and eliminates most false positive results. J Immunol Methods. 1996 Oct;198(1):67–77.

230. Dempster DW, Compston JE, Drezner MK, Glorieux FH, Kanis JA, Malluche H, et al. Standardized nomenclature, symbols, and units for bone histomorphometry: A 2012 update of the report of the ASBMR Histomorphometry Nomenclature Committee. J Bone Miner Res. 2013 Jan;28(1):2–17.

231. Erben RG, Glösmann M. Histomorphometry in Rodents. In 2012. p. 279–303.

232. Mohammad M, Hu Z, Ali A, Kopparapu PK, Na M, Jarneborn A, et al. The role of *Staphylococcus aureus* lipoproteins in hematogenous septic arthritis. Sci Rep. 2020 Dec 13;10(1):7936.

233. Gillaspy AF, Hickmon SG, Skinner RA, Thomas JR, Nelson CL, Smeltzer MS. Role of the accessory gene regulator (agr) in pathogenesis of staphylococcal osteomyelitis. Infect Immun. 1995 Sep;63(9):3373–80.

234. Mohammad M, Nguyen MT, Engdahl C, Na M, Jarneborn A, Hu Z, et al. The YIN and YANG of lipoproteins in developing and preventing infectious arthritis by *Staphylococcus aureus*. Kielian T, editor. PLoS Pathog. 2019 Jun 21;15(6):e1007877.

235. Morita M, Iwasaki R, Sato Y, Kobayashi T, Watanabe R, Oike T, et al. Elevation of pro-inflammatory cytokine levels following anti-resorptive drug treatment is required for osteonecrosis development in infectious osteomyelitis. Sci Rep. 2017 Jun 7;7(1):46322.

236. Martino MM, Maruyama K, Kuhn GA, Satoh T, Takeuchi O, Müller R, et al. Inhibition of IL-1R1/MyD88 signaling promotes mesenchymal stem cell-driven tissue regeneration. Nat Commun. 2016 Apr 22;7(1):11051.

237. Zhang P, Liu J, Xu Q, Harber G, Feng X, Michalek SM, et al. TLR2-dependent Modulation of Osteoclastogenesis by *Porphyromonas gingivalis* through Differential Induction of NFATc1 and NF-κB. J Biol Chem. 2011 Jul;286(27):24159–69.

238. Grevers LC, de Vries TJ, Vogl T, Abdollahi-Roodsaz S, Sloetjes AW, Leenen PJMM, et al. S100A8 enhances osteoclastic bone resorption in vitro through activation of Toll-like receptor 4: Implications for bone destruction in murine antigen-induced arthritis. Arthritis Rheum. 2011 May;63(5):1365–75.

239. Yang J, Ryu YH, Yun CH, Han SH. Impaired osteoclastogenesis by staphylococcal lipoteichoic acid through Toll-like receptor 2 with partial involvement of MyD88. J Leukoc Biol. 2009 Oct;86(4):823–31.

240. Liu YHH, Huang D, Li ZJJ, Li XHH, Wang X, Yang HPP, et al. Toll-like receptor-4-dependence of the lipopolysaccharide-mediated inhibition of osteoblast differentiation. Genetics and Molecular Research 2016;15(2):1–11.

241. Alonso-Pérez A, Franco-Trepat E, Guillán-Fresco M, Jorge-Mora A, López V, Pino J, et al. Role of toll-like receptor 4 on osteoblast metabolism and function. Front Physiol. 2018;9:1–12.

242. Bandow K, Maeda A, Kakimoto K, Kusuyama J, Shamoto M, Ohnishi T, et al. Molecular mechanisms of the inhibitory effect of lipopolysaccharide (LPS) on osteoblast differentiation. Biochem Biophys Res Commun. 2010 Nov;402(4):755–61.

243. Agostini L, Martinon F, Burns K, McDermott MF, Hawkins PN, Tschopp J. NALP3 Forms an IL-1β-Processing Inflammasome with Increased Activity in Muckle-Wells Autoinflammatory Disorder. Immunity. 2004 Mar;20(3):319–25.

244. Park-Min KH, Lim E, Lee MJ, Park SH, Giannopoulou E, Yarilina A, et al. Inhibition of osteoclastogenesis and inflammatory bone resorption by targeting BET proteins and epigenetic regulation. Nat Commun. 2014 Dec 13;5(1):5418.

245. Xiao Y, Palomero J, Grabowska J, Wang L, de Rink I, van Helvert L, et al. Macrophages and osteoclasts stem from a bipotent progenitor downstream of a macrophage/osteoclast/dendritic cell progenitor. Blood Adv. 2017 Oct 24;1(23):1993–2006.

246. Kovarova M, Hesker PR, Jania L, Nguyen M, Snouwaert JN, Xiang Z, et al. NLRP1 dependent pyroptosis leads to acute lung injury and morbidity in mice. J Immunol. 2012 Aug 8;189(4):2006.

247. Kuida K, Lippke JA, Ku G, Harding MW, Livingston DJ, Su MSS, et al. Altered Cytokine Export and Apoptosis in Mice Deficient in Interleukin-1β Converting Enzyme. Science. 1995 ;267(5206):2000–3.

248. Ikeda K, Takeshita S. The role of osteoclast differentiation and function in skeletal homeostasis. J Biochem. 2016 Jan;159(1):1–8.

249. Bouxsein ML, Boyd SK, Christiansen BA, Guldberg RE, Jepsen KJ, Müller R. Guidelines for assessment of bone microstructure in rodents using micro-computed tomography. J Bone Miner Res. 2010 Jun 7;25(7):1468–86.

250. Park JH, Lee NK, Lee SY. Current Understanding of RANK Signaling in Osteoclast Differentiation and Maturation. Mol Cells. 2017;40(10):706–13.

251. Teitelbaum SL. The osteoclast and its unique cytoskeleton. Ann N Y Acad Sci. 2011;1240(1):14–7.

252. Krauss JL, Roper PM, Ballard A, Shih C cheng C, Fitzpatrick JAJJ, Cassat JE, et al. *Staphylococcus aureus* Infects Osteoclasts and Replicates Intracellularly. Whiteley M, editor. mBio. 2019 Oct 15 ;10(5):1–15.

253. Raynaud-Messina B, Verollet C, Maridonneau-Parini I. The osteoclast, a target cell for microorganisms Vol. 127, Bone. 2019. p. 315–23

254. Dou C, Zhen G, Dan Y, Wan M, Limjunyawong N, Cao X. Sialylation of TLR2 initiates osteoclast fusion. Bone Res. 2022 Mar 2;10(1):24.

255. Charles JF, Hsu LY, Niemi EC, Weiss A, Aliprantis AO, Nakamura MC. Inflammatory arthritis increases mouse osteoclast precursors with myeloid suppressor function. J Clin Invest. 2012 Dec 3;122(12):4592–605.

256. Prates TP, Taira TM, Holanda MC, Bignardi LA, Salvador SL, Zamboni DS, et al. NOD2 contributes to *Porphyromonas gingivalis*-induced bone resorption. J Dent Res. 2014 Nov;93(11):1155–62.

257. Ke K, Sul OJ, Chung SW, Suh JH, Choi HS. Lack of NOD2 attenuates ovariectomy-induced bone loss via inhibition of osteoclasts. Journal of Endocrinology. 2017 Nov;235(2):85–96.

258. Joung J, Konermann S, Gootenberg JS, Abudayyeh OO, Platt RJ, Brigham MD, et al. Genome-scale CRISPR-Cas9 knockout and transcriptional activation screening. Nat Protoc. 2017;12(4):828–63.

259. Cheng Y, Liu H, Li J, Ma Y, Song C, Wang Y, et al. Evaluation of culture conditions for osteoclastogenesis in RAW264.7 cells. Sirigiri DNR, editor. PLoS One. 2022 Nov 17;17(11):e0277871.

260. Schneider-Poetsch T, Ju J, Eyler DE, Dang Y, Bhat S, Merrick WC, et al. Inhibition of eukaryotic translation elongation by cycloheximide and lactimidomycin. Nat Chem Biol. 2010 Mar 31;6(3):209–17.

261. Orning P, Weng D, Starheim K, Ratner D, Best Z, Lee B, et al. Pathogen blockade of TAK1 triggers caspase-8–dependent cleavage of gasdermin D and cell death. Science. 2018 Nov 30;362(6418):1064–9.

262. Gram AM, Booty LM, Bryant CE. Chopping GSDMD: caspase-8 has joined the team of pyroptosis-mediating caspases. EMBO J. 2019 May 15;38(10):2–4.

263. Wang H, Sun L, Su L, Rizo J, Liu L, Wang LF, et al. Mixed Lineage Kinase Domain-like Protein MLKL Causes Necrotic Membrane Disruption upon Phosphorylation by RIP3. Mol Cell. 2014 Apr;54(1):133–46.

264. Akara-amornthum P, Lomphithak T, Choksi S, Tohtong R, Jitkaew S. Key necroptotic proteins are required for Smac mimetic-mediated sensitization of cholangiocarcinoma cells to TNF-α and chemotherapeutic gemcitabine-induced necroptosis. Lebedeva I v., editor. PLoS One. 2020 Jan 8;15(1):e0227454.